UNIVERSITA' DEGLI STUDI DI NAPOLI
"FEDERICO II"
Doctorate School in *Earth, Environmental and Resources Sciences*

Ph.D. Thesis, XXIX Cycle

Analysis of rock masses belonging to the Apennine-Maghrebide Orogen by means of in situ and remote methodologies applied to rockfall risk assessment

Advisor:
Prof. Domenico Calcaterra

Ph.D. candidate:
Simone Mineo

Co-Advisors
Prof.ssa Giovanna Pappalardo
Prof. Sebastiano Perriello Zampelli

Coordinator of Doctorate School
Prof. Maurizio Fedi

- Academic Year 2016/2017-

Contents

List of Figures

List of Tables

List of acronyms

2D: Two-Dimensions.

3D: Three-Dimensions.

AVI: Aree Vulnerate Italiane (Italian Vulnerable Areas).

CA: Cliff Area.

CNR: Consiglio Nazionale delle Ricerche (National Research Council).

CPO: Calabria Peloritani Orogen.

CR: Coefficient of Restitution.

CRI: Cooling Rate Index.

Dol: Dolostone outcrop.

DTM: Digital Terrain Model.

DZ: Deposit Zone.

ETA: Event Tree Analysis.

FS: Factor of Safety.

IRT: InfraRed Thermography.

JCS: Joint Compressive Strength.

JRC: Joint Roughness Coefficient.

Jv: Volumetric Joint Count.

ISRM: International Society for Rock Mechanics.

LiDAR: Light Detection And Ranging.

Lim: Limestone outcrop.

LTU: Longi Taormina Unit.

LW: Lower segment of SP-10 at MRA.

Med: Medolo outcrops.

MRA: Main Road Area.

n.a.: not available.

PAI: Piano Assetto Idrogeologico (Hydrogeological Attitude Plan).

PGA: Peak Ground Acceleration.

PF: Probability of Failure.

Por: Porphyroid outcrops.

RHRS: Rockfall Hazard Rating System.

RMR: Rock Mass Rating.

RQD: Rock Quality Designation.

SP: Strada Provinciale (Provincial Road).

SZ: Source Zone.

TZ: Transition Zone.

UCS: Uniaxial Compressive Strength.

UNESCO: United Nations Educational, Scientific and Cultural Organization.

UP: Upper segment of SP-10 at MRA.

USGS: United States Geological Survey.

WP/WLI: Working Party on World Landslide Inventory.

ABSTRACT

The rockfall attitude of rock slopes threatening a strategic spot of eastern Sicily has been studied herein with the aims of testing an innovative methodology for the remote survey of fractured rock outcrops and of assessing the rockfall risk along an important transportation corridor through a quantitative probabilistic approach.

The study area, often involved in rockfall events, which cause serious damage to private and public infrastructures, is one of the most relevant places of Sicily due to the great tourism rate recorded every year between the resorts of Taormina and Castelmola, which are also considered an outstanding example of cultural heritage.

The innovative procedure of rock mass survey through InfraRed Thermography is tested and proposed herein for the study of the fracturing condition of intensely jointed rock masses, to find out what kind of information can be assessed in this field of rock mechanics. Although this technique is widely used in several scientific fields, its direct application for such purposes is still pioneering. In this thesis, thermal imaging campaigns, carried out under different climatic conditions, are described, and interesting considerations are proposed with reference to a Cooling Rate Index, estimated to study how rock masses, conditioned by their fracture nets, behave during the heat transfer towards the external environment. Such an index was related to the degree of fracturing of the rock masses to find a relationship linking thermal data to one of the main quantitative fracturing indexes. Results return interesting matches between some geostructural features and thermal outputs, demonstrating the reliability of the application of such methodology to bare rock masses. Moreover, new experimental considerations are proposed, laying the

foundations for future studies aimed to further validate the InfraRed Thermography as an effective remote survey technique.

Risk assessment was carried out through the quantitative approach of the Event Tree Analysis, which was properly customized to take into account the peculiarity of the area and of the road path. Rock mass surveys, trajectory simulations and probabilistic models were taken into account with the aim of calculating the probability related to possible scenarios in case of rockfalls.

Achieved outcomes demonstrate that such procedure is a reliable tool, which can be taken as reference to calibrate further risk models in comparable contexts of the world, where rockfall threaten communication routes. This would represent a helpful instrument to the scientific community and to local authorities dealing with one of the most troublesome natural phenomena affecting the public safety.

INTRODUCTION

In populated mountainous areas, rockfalls are considered one of the major natural threat to the life and represent a relevant risk for people, structures and infrastructures. In particular, rockfall risk is the expression of the likelihood and impact of an uncertain, sudden and extreme landslide event which, if occurring, may cause a certain kind of damage to one or more elements (modified after Ball and Watt, 2001; UNESCO, 2010).

In a period characterized by an increasing interest of local authorities and media on natural risks, the International Scientific Community dealing with rockfalls is more and more focused on developing new technologies for the stability modeling of rock masses, looking for innovative approaches for the survey and processing of field data, with the aim of assessing the associated risk in qualitative or quantitative ways (e.g. Budetta, 2004; Saroglou et al., 2012; Schober et al., 2012; Frattini et al., 2013; Mineo et al., 2015a; Roberds, 2015; Pappalardo et al., 2016a; Budetta et al., 2016).

It is known that forecasting the exact progression of a rockfall in space and time is not a simple practice, due to the unpredictable attitude of such events (Guzzetti and Reichenbach, 2010). Therefore, it is self-evident how important a comprehensive study of the rock slopes threatening specific areas is, starting from the in-situ survey to remote sensing approaches and numerical elaborations.

In this perspective, the research presented herein represents a contribution to this scientific activity, proposing a study on the rockfall attitude of a strategic spot of eastern Sicily, close to the city of Taormina, where the complex geological history has led to a great predisposition of rock slopes to landslide. The main purpose of this research is the analysis of the slopes threatening such relevant tourist area, already affected by numerous rockfalls in the latest decades, aimed at assessing the related risk along an important

communication route. The study presented herein has been carried out following different steps, experiencing also innovative technological approaches for the remote survey of rock masses, to study the rockfall problem under both qualitative and quantitative points of view. The synergy of different approaches commented herein allowed achieving numerous data on geology, geomechanics, thermal attitude, kinematics and stability of surveyed rock slopes, which were used to design a quantitative model for risk assessment, properly customized for the study area.

In particular, the innovative approach experienced in this study is the application of InfraRed Thermography (IRT) for the study of the degree of fracturing of rock masses. This is a pioneering methodology, exploiting the thermal radiation to study the cooling behavior of rock masses and then relating such attitude to their fracturing condition (Teza et al., 2012; Martino and Mazzanti 2014). This is a new aspect of geomechanics, since IRT had never been employed for similar purposes before. In this study, the cooling attitude of rock masses is expressed by a new index (the Cooling Rate Index), which was conceived with the aim of finding a numerical reference for the remote evaluation of the rock fracturing.

Thermal surveys were sided by in-situ rock mass surveys and rockfall trajectory simulations were carried out by using bi-dimensional and three-dimensional codes and results were applied to a quantitative risk assessment method, focused on probabilistic calculations according to Event Trees properly designed.

The approach used herein can be taken as reference to calibrate further risk models in several peculiar parts of the world, where rockfall threaten communication routes. This would represent a great instrument to the scientific community and to local authorities dealing with one of the most problematic natural phenomena affecting the public safety.

CHAPTER 1

AIMS AND METHODOLOGY

1.1. State of the art on the scientific topic

Dealing with rockfalls means dealing with natural phenomena acknowledged among the most serious natural hazards, due to their high degree of unpredictability and rapid evolution. Every year international chronicles report on victims or on missed injuries after a rockfall event, highlighting how such type of phenomena is widespread all over the world. In the latest years, public awareness on this topic has grown and rockfall has become one of the most intensely studied geomorphic processes worldwide, especially in mountainous areas (Chau et al., 2003; Dorren and Seijmonsbergen, 2003; Schneuwly and Stoffel, 2008). In fact, the increasing settlement, along with the growth rates in tourism, have led to a considerable spatial extension of endangered areas, and so to a consequent rising need for safety and protection of the population. To achieve a reliable knowledge of the possible scenarios in case of rockfalls, detailed studies are required to model the stability conditions of the slopes and to attain a reliable hazard assessment. Nevertheless, forecasting the exact evolution of a rockfall in space and time is a very tough task, due to the numerous factors controlling such events (Guzzetti and Reichenbach, 2010). Therefore, the International Scientific Community keeps looking for different methodological approaches to deal with such a problematic issue (e.g. Yin et al., 2011; Schober et al., 2012; Frattini et al., 2012; Sarro et al., 2014; Mateos et al., 2015; Perriello Zampelli et al., 2015).

Several studies were carried out on various aspects of rockfall, such as dynamic behavior (Ritchie, 1963; Erismann, 1986; Azzoni et al., 1995), boulder reaction during ground contact and rockfall trajectory (Bozzolo et al., 1986; Hoek, 1987; Hungr and Evans, 1988; Pfeiffer and Bowen, 1989; Evans and Hungr, 1993; Crosta and Agliardi, 2003; Paronuzzi, 2009), or runout distance of falling rocks

(Kirkby and Statham, 1975; Statham and Francis, 1986; Okura et al., 2000). Some researchers focused also on the possible triggering factors by taking into account freeze-thaw cycles (e.g. Murton et al., 2006; Stock et al., 2013; Gupta and Tandon, 2015; Macciotta et al., 2015; Park and Park, 2016), changes in the rock-moisture degree, increase of mean annual temperature, occurrence of earthquakes (e.g. Gardner, 1983; Harp and Wilson, 1995; Matsuoka and Sakai, 1999; Davies et al., 2001; Marzorati et al., 2002; Sass, 2005; Matsuoka, 2006; Barbano et al., 2014). Furthermore, since the late 1980s, numerical modelling has become a common practice in rock engineering (Guzzetti et al., 2002; Dorren et al., 2006; Stoffel and Perret , 2006), especially when a hazard or risk assessment is pursued. In this perspective, different methods were proposed for rockfall risk mapping, both along linear structures and within exposed areas, in order to identify slopes at high risk of failure and to allow preventive measures to be effectively prioritized (Pierson et al., 1990; Budetta, 2011; Crosta and Agliardi, 2003; Peila and Guardini, 2008; Pantelidis and Kokkalis, 2011; Saroglou et al., 2012; Budetta et al., 2016). Besides their scientific relevance, such studies have an important economic impact, as they imply a subsequent involvement of local authorities for the design and construction of the most suitable mitigation measures.

Nevertheless, regardless of the final purpose, the analysis of these events has to get started from the in-situ geological and geomechanical survey, which is the only practice ensuring a reliable assessment of the main structural and mechanical features of the rock slopes, on which the occurrence of rockfalls depends. To this purpose, several researchers presented integrated analyses of rock slopes, by means of different survey methodologies, to highlight the multidisciplinary aspect of such a complex topic (e.g. Watanabe and Sassa, 1996; Arosio et al., 2009; Mineo et al., 2015b; Pappalardo et al., 2016b). However, a recurring problem to face during the in situ surveys is the

accessibility of the study area. In fact, usually the unstable sectors are located at sectors of a cliff or hard to reach, thus requiring a technological support. This is why part of the Scientific Community is currently experiencing remote sensing techniques able to acquire field data from a remote survey position. This is the case of the employment of airborne and terrestrial geodetic LiDAR-scans (e.g. Gordon et al. 2001; Oppikofer et al. 2009; Gigli and Casagli 2011; Niethammer et al., 2012; Fanti et al., 2013; Michoud et al., 2015), for example. Reliable results are achieved also by the analysis of terrestrial stereoscopic photographs (e.g. Poetsch et al., 2007; Haneberg, 2008; Ferrero et al., 2009; De Vita et al., 2012; Perriello Zampelli, 2015), or by the differential InSAR (Interferometric Synthetic Aperture Radar), which enables detailed displacement analysis in case of a monitoring survey (e.g. Di Martire et al., 2016; Rouyet et al., 2016). Moreover, a recent practice, although still pioneering, exploits the InfraRed thermal radiation to detect peculiar features along a slope (e.g. Wu et al., 2005; Baron et al., 2012; Mineo at al., 2015a; Pappalardo et al., 2016a). This methodology, which is currently providing useful contribution in several field of sciences, is part of the methodological approach carried out in this research, thus it will be presented in detail in the following paragraphs.

All the innovative techniques above mentioned are part of the new frontiers in the remote survey of rock masses, which draw the attention of the International Scientific Community in an attempt to improve the knowledge to achieve higher standards of safety and protection.

1.2. Methodological approach

The different approaches commented herein were planned trying to follow a strict path in order to achieve, step by step, set goals.

Due to the geological peculiarity of the study area, which have led to an intense degree of fracturing of the rock masses, the first activity was a geological survey aimed at mapping the main formations cropping out in this spot and to highlight their relationship, with particular reference to the high number of tectonic contacts between them. This survey was useful to achieve a good knowledge of the area and to select the representative rock masses, which underwent a survey according to ISRM recommendations (2007). The main geostructural and geomechanical parameters were estimated and discontinuities were grouped into systems according to a statistical contouring procedure, analyzing mean and maximum pole concentrations, using the Fisher distribution method (Fisher, 1953).

Based on obtained data, a kinematic analysis has been performed in order to highlight the potential failure mechanisms affecting the slopes. At the same time, a thermal mapping of rock masses was performed during one-day surveys, both in the dry and cold seasons, with the aim of studying their thermal behavior and proving how IRT may be useful in the remote survey of fractured rock slopes. Temperature records were used for the reconstruction of the cooling trend of the rock masses, describing the decrease of the temperature during the survey time. Interesting considerations are proposed with reference to an index, herein named Cooling Rate Index (CRI), estimated to study how rock masses, conditioned by the fracture nets, behave during their cooling. Such behavior was related to the degree of fracturing of rock masses to find a relation linking IRT data to one of the main quantitative fracturing indexes (i.e. Rock Quality Designation according to Deere, 1963).

Once ascertained the poor conditions of rock slopes, the combination of possible rockfall trajectories was modeled and studied through 2D and 3D codes, with the purpose of highlighting the potential targets of such events, along with the spatial evolution of rockfalls (i.e. trajectory simulations, rebound points, end points, kinetic energy). This procedure was calibrated according to back-analyses performed after the occurrence of two important events, which caused alarmism and discomfort to population and tourists. Achieved results were graphically represented on thematic maps, for a better reading of the problem, and were finally taken into account for the quantitative risk assessment along the main element at risk, represented by a transportation corridor connecting the resorts of Taormina and Castelmola. Such risk assessment was carried out through the Event Tree Analysis method, properly customized for the study area. The probability computation, carried out according to similar studies available in literature (e.g. Bunce et al., 1997; Peila and Guardini, 2012; Budetta et al., 2016 and references therein), provided interesting results related to the possible negative outcomes arising from the impact of falling boulders on the road. Achieved numerical data were graphically represented on thematic maps aimed at providing an immediate and intuitive prevention tool, which can be employed for future land-use planning.

CHAPTER 2

LANDSLIDES ALONG ROCK SLOPES

2.1. Rockfalls

Landslides involving rock material are usually referred to as rockfalls. Such kind of movements are among the most rapid land-instability events, defined as one of the most prominent geomorphic processes (e.g., Hales and Roering, 2007; Beylich and Kneisel, 2009) and natural hazards (e.g., Jaedicke et al., 2009; Heckmann et al., 2016), especially in mountainous areas. They generally occur at rock slopes or vertical cliffs through the detachment of one or more boulders, which move down slope by bouncing and flying along ballistic trajectories or by rolling along the slope itself (Varnes, 1978). Such phenomena are relevant from the engineering-geological point of view, because of their frequent occurrence, especially in mountainous areas, and of the complexity of their modeling. In fact, forecasting the exact evolution of a rockfall in space and time is a very tough task, due to the numerous factors controlling such events (Guzzetti and Reichenbach, 2010). Among these, the physical properties of falling boulders, the slope geometry, the elastic properties of the lithologies along the slope and the presence of obstacles along the falling rock trajectory can be mentioned (e.g. Parise, 2002; Schweigl et al., 2003).

The causes of rockfalls are numerous and can be assorted into three main groups (USGS, 2004): geological, morphological and human. Among the geological causes, the degree of jointing of a rock mass and the orientation of the discontinuity systems are the most relevant (Markland, 1979; Hoek and Bray, 1981). In fact, the presence of fractures affects the geomechanical quality of the rock mass, along with its strength and deformability (e.g. Norrish and Wyllie, 1996; Hantz et al., 2003; Jaboyedoff et al., 2004; Budetta, 2011). Furthermore, the fracture network controls the water circulation within a rock mass, which favors weathering processes, concurring to the worsening of the

mechanical properties of the rock (e.g. Crosta and Agliardi, 2003; Dorren and Seijmonsbergen, 2003; Calcaterra and Parise, 2010; Dochez et al., 2014; Mineo et al., 2015b). Even the contrast in competence between different or differently fractured rock types can be regarded as a geological cause of rockfalls, especially in areas affected by heavy rainfall events (Barbano et al., 2014).

Morphological causes include tectonic or volcanic uplift, which usually are accompanied by seismic shakings, or fluvial/wave/glacial erosion of the slope toe. Moreover, there are some processes, taking place within the discontinuities, which can lead to a worsening of their mechanical properties. These are freeze-and-thaw mechanisms in cold climates or the increase of pore pressure after thawing of snow/ice blankets. Similar effects can be produced also either by the erosion of surrounding material during heavy rainstorms, or by root growth, or by leverage action played by roots moving in high winds.

Human causes are all the anthropogenic activities carried out to favor the increasing settlement and to implement the communication routes. Among these, excavation and mining can be regarded as the most common causes, followed by artificial vibrations and water leakage from utilities.

These are only some of the numerous possible causes, which can either predispose a slope to rockfall or trigger the event.

In general, the area where a rockfall occurs can be divided into three zones (Figure **1**): the movement originates at the source zone or detachment zone, located either at the top of the slope or along the slope face, where a hypothetic block is dislodged by one or more triggering causes, initiating a down slope motion under the effect of the gravity. After a phase of free-fall, the block moves bouncing or rolling in the transition zone, interacting with different elements of the slope, where the maximum dynamic activity takes place. Such interaction plays a key role in the evolution of the event, with

respect to the block energy and its trajectory. Finally, the falling rock is progressively slowed down until a complete stop in the deposit zone, where it will lie together with other fallen boulders.

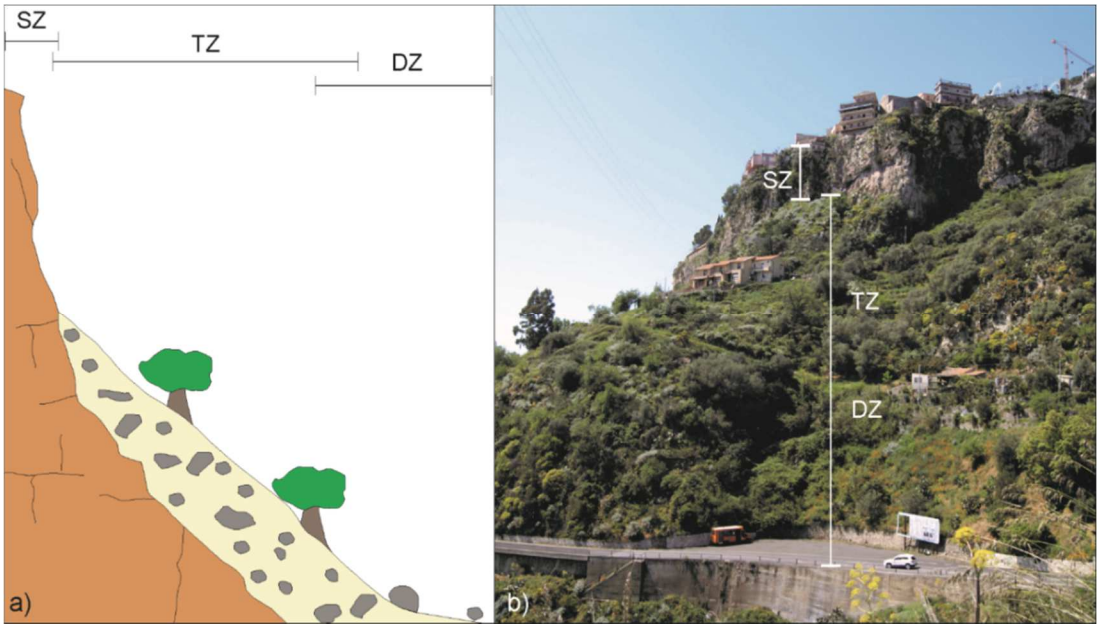

Figure 1: a) sketch of the three typical rockfall activity zones. SZ: source zone; TZ: transition zone; DZ: deposit zone; b) example of a rockfall zonation in the study area: in this case, TZ and DZ overlap because of the steep morphology of the slope and the presence of vegetation.

2.2. Main classification systems for landslides along rock slopes

Although in the common practice the term "rockfall" is generally used to refer to landslides affecting rock materials, there are several classifications, which take into account the kinematics of the failure, to make a distinction between different movements.

In 1978, Varnes proposed a classification of slope movements based on both the type of material involved and the type of movement. This can be considered a complete classification for landslides and it is described herein with particular reference to the movements affecting rock masses.

The landslide nomenclature is composed of two terms: the first one refers to the material type (e.g. "rock" for rock material, "soil" for aggregate of solid particles), while the second term describes the type of movement. In particular, rock is defined as "a hard or firm mass that was intact and in its natural place before the initiation of movement".

There are five kinematically distinct types of movement:

1) Rock-Fall: abrupt movements of masses of geologic materials, such as rocks and boulders, detached from steep slopes or cliffs. Separation can occur along both pre-existing discontinuities, such as joints, fault planes and bedding planes, and along neo-formation surfaces. The falling boulder moves downstream through free-fall, bouncing and rolling until a complete stop at the foot of the slope. Such landslides are strongly influenced by gravity, mechanical weathering, and presence of interstitial water. Moreover, they involve high rate of kinetic energy and are characterized by a high level of unpredictability (APAT, 2006).
2) Rock-Topple: movement driven by the forward rotation of a detached block above a pivotal point, located in the lower part of the detached material, under the actions of gravity and forces exerted by adjacent units or by fluids in cracks.

3) Rock-Slide: sliding movement occurring along a surface of rupture, which can be either circular or planar. The first (rotational slide) is a rare case for rocks, taking place only at weak rock materials such as highly weathered or closely fractured rocks. The second one (translational slide) occurs when the rock volume moves along a roughly planar surface.
4) Rock-Spread: it usually occurs on very gentle slopes or flat terrain. The dominant mode of movement is lateral extension accompanied by shear or tensile fractures. When a coherent material, either bedrock or soil, rests on materials that liquefy, the upper units may undergo fracturing and extension and then it may subside, translate, rotate or disintegrate.
5) Rock-Flow or Deep-Seated Gravitational Creep: it is the imperceptibly slow, steady, downward movement of slope formed by soil or rock. Movement is caused by shear stress sufficient to produce permanent deformation, but too small to produce shear failure.

The combination of two or more of the above types is known as a complex landslide.

This classification system was widely accepted by workers in several countries, although usually with slight modifications (e.g. Hungr and Picarelli, 2014). A velocity scale, later updated by International Geotechnical Society's UNESCO Working Party on World Landslide Inventory (WP/WLI) (1995) and Cruden and Varnes (1996) completes the classification (Table 1) and allows classifying rockfalls as "very rapid" to "extremely rapid" movements.

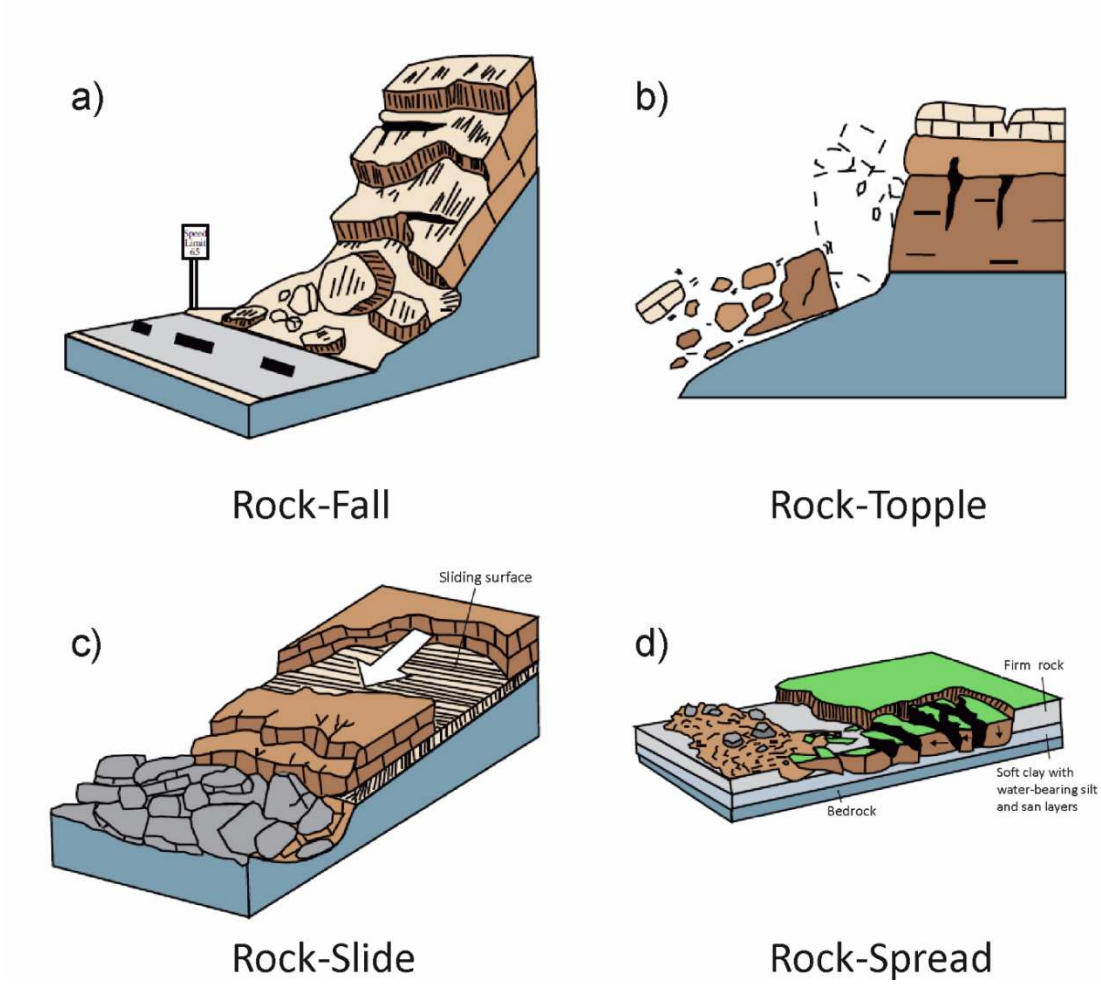

Figure 2: sketch of the main types of landslide movements according to Varnes (1978), modified after USGS (2004).

A further classification deserving a comment is the one proposed by Hungr et al. (2001), who reviewed the classification of flow-type landslides. Among the categories described, the "rock avalanche" movement needs to be a mentioned. It regards fragmented rocks, either dry or saturated, which originate as intact rock mass at the source of the landslide, but disaggregate in the course of failure. It gains an extremely high velocity in a flow-like motion of a large volume of rock material (even greater than 10,000 m^3) originating from a rockfall or a rock slide.

Table 1: Landslide velocity scale (after Cruden and Varnes, 1996).

Velocity class	Description	Velocity (m/s)	Typical velocity
7	Extremely Rapid	5	5 m/s
6	Very Rapid	0.05	3 m/min
5	Rapid	$5x10^{-4}$	1.8 m/hr
4	Moderate	$5x10^{-6}$	13 m/month
3	Slow	$5x10^{-8}$	1.6 m/year
2	Very Slow	$5x10^{-10}$	16 mm/year
1	Extremely Slow		

In addition to the systems above reported, which allow classifying landslide movements with reference to their failure pattern and to the type of involved material, there is a classification system based on the "state of activity" of landslides. There is a wide literature documentation on this issue, firstly proposed by WP/WLI (1995) and Cruden and Varnes (1996). In particular, the Italian Agency for Protection of the Environment and Technical Services (APAT, 2006), who summarizes the guidelines available in the national and international literature (e.g. Amanti et al., 2001), refers to the state of activity as a "fundamental descriptive element useful, at least in the short term, for prediction purposes".

According to this classification, a landslide can be defined as:

i) Active: when the landslide is currently moving. For example, when the erosion at the foot of a cliff triggers the toppling of a rock volume.

ii) Suspended: when the landslide has moved within the last 12 months, but it is currently not active. For example, when the cracking phenomena occur at the source area of the previous rockfall, weakening the rock and predisposing a new rock volume to failure.

iii) Reactivated: when the landslide is active after a period of inactivity. For example, the prone-to-fail rock volume mentioned at point *ii* fails, possibly mobilizing the material lying in the deposit zone.

iv) Inactive: when the landslide has not moved within the last 12 months. In this case the landslide can be defined as:

   a) *dormant* if it could be reactivated by its original causes or other causes;

   b) *abandoned* if it is no longer affected by its original causes;

   c) *stabilized* if it has been protected by its original causes by nature or by artificial remedial measures;

   d) *relict* if it developed under climatic or geomorphological conditions considerably different from those at present.

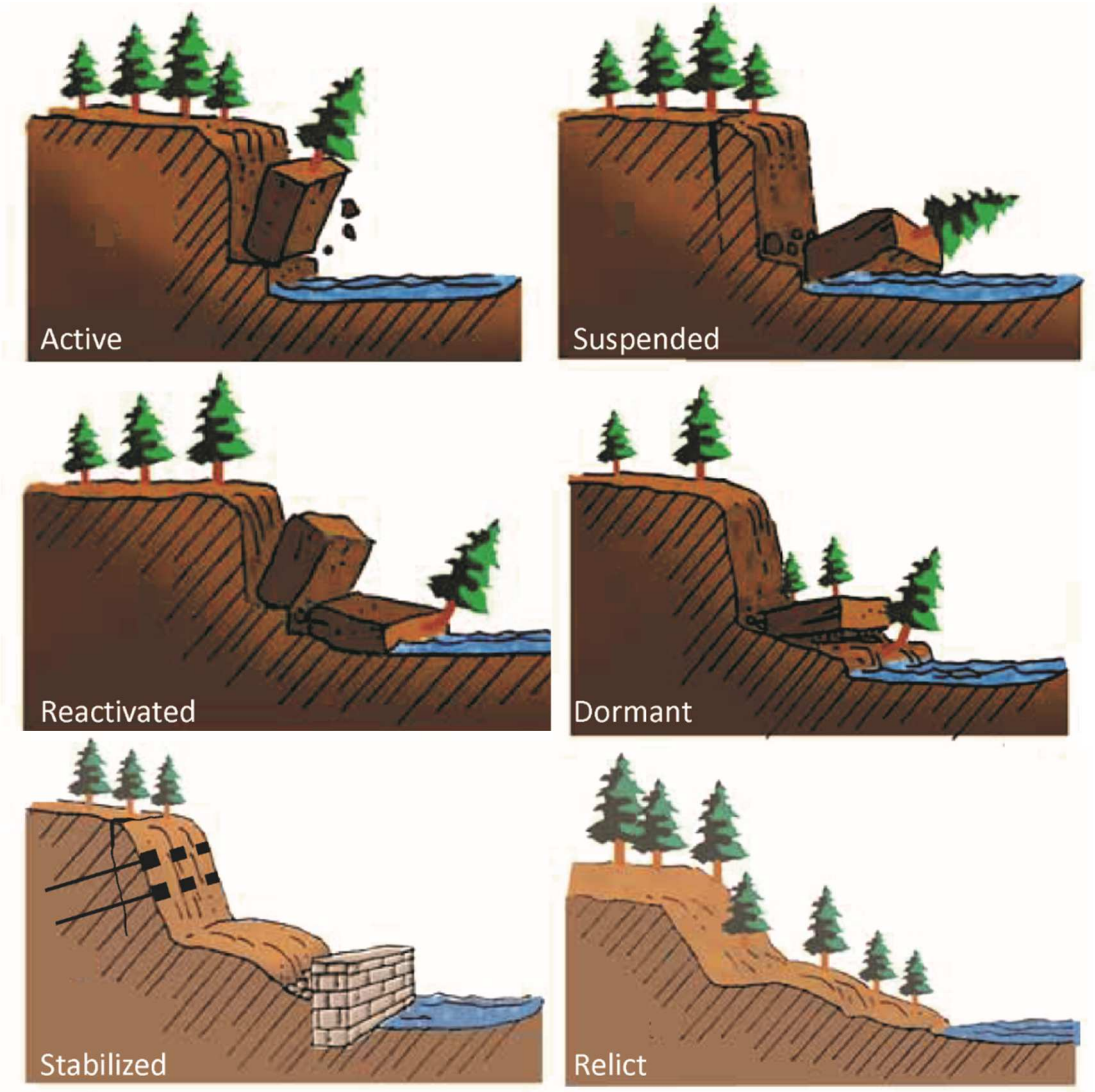

Figure 3: sketch of the main configurations of state of activity of landslide movements, modified after APAT (2006).

CHAPTER 3

THE STUDY AREA

3.1. General background

The study area is located in one of the most-visited tourist spot of southern Italy, along the Ionian coastline of northeastern Sicily (Figure 4a). Here, the charming city of Taormina and its surroundings are popular travel destinations, attracting visitors from all over the world. In the mountainous sector of this area, Castelmola represents one of the most recommended tourist attractions, renowned for its singular landscape enclosing the Etna volcano and the Ionian Sea. This village, which probably used to be the acropolis of Taormina in the Hellenic age, is a 1100-inhabitant village of pre-Hellenic origin, acknowledged among the Most Beautiful Italian Villages (Bacilieri, 2012). It lays on a rock cliff (average elevation 460 m a.s.l.) and it is approachable only through the Provincial Road 10 (Strada Provinciale 10, SP10), which is a two-lane hill road crossing the steep reliefs and deep valleys between Taormina and Castelmola (Figure **4**b).

The geomorphological conditions, along with the geological and tectonic settings of this region, make the steep and heavily fractured slopes highly prone to instability phenomena. In fact, over the last decades, numerous and repeated landslides occurred in this territory, threatening the strategic structures and infrastructures located at two main sub-areas (Figure **4**c): the Cliff Area (CA) and the Main Road Area (MRA). In particular, CA is located at the foot of the 25 m-high carbonate cliff on which Castelmola lies. Here, a group of private houses and a pedestrian tourist track are likely to be regarded as possible elements of concern in case of rockfall. On the other hand, MRA holds the final segment of SP10 (1.7 km of length; between km 6+100 m and km7+800 m), which meanders along the slopes with sharp curves and steep grades. In this area, SP10 can be divided into two parallel segments at a

different altitude: the upstream and downstream segments (Figure **4**c). This is a critical condition because, in case of landslide movements, this road is doubly subject to possible disruptions, which would mean major setbacks not only from a touristic and economic point of view but also for rescue purposes during a potential state of emergency. In fact, SP10 is the only access way to Castelmola and the only escape route in case of evacuation.

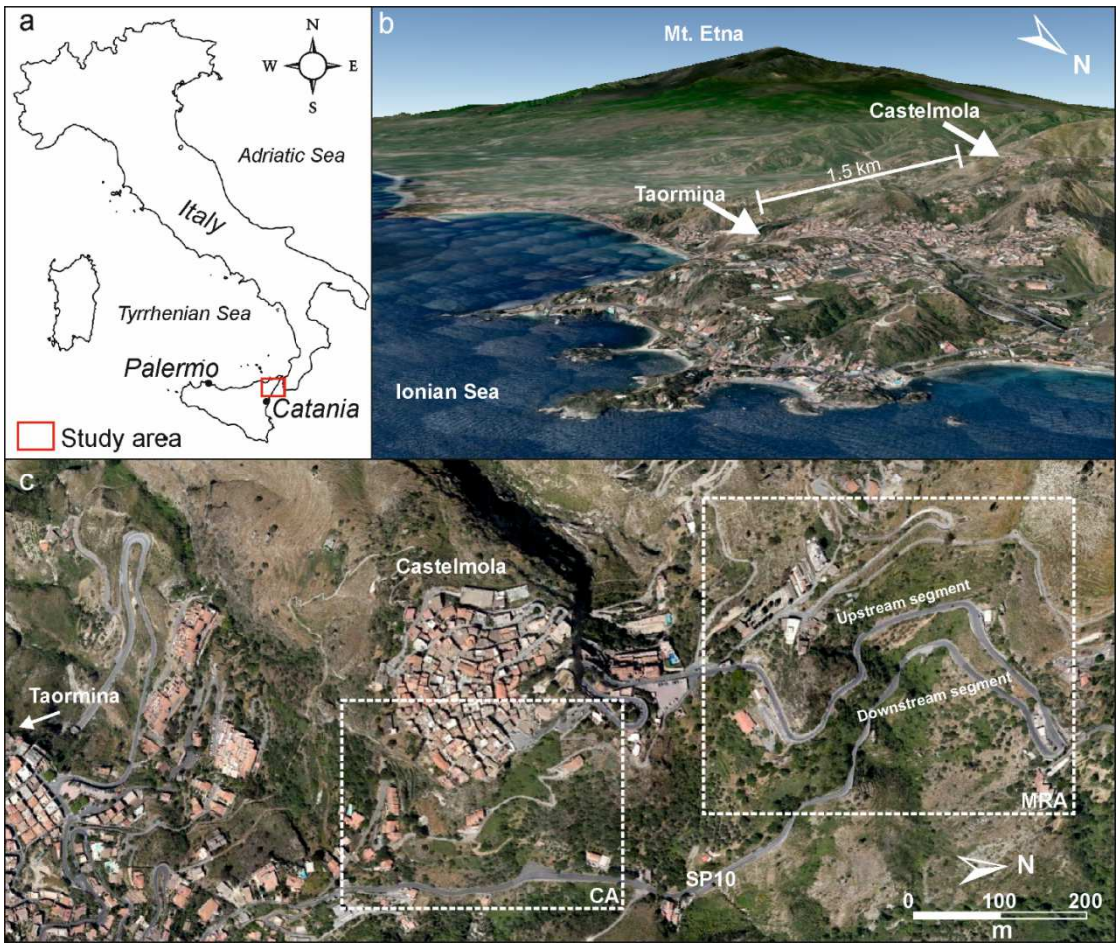

Figure 4: a) geographical location of the study area; b) location of Taormina and Castelmola; c) aerial view of the sub-areas (CA: Cliff Area; MRA: Main Road Area).

3.2. Regional geological and tectonic setting

From a regional geological point of view, the study area lies in the southern sector of the Peloritani Mountains, close to the geological contact with the volcanic products of Mount Etna. In particular, the Peloritani Mountain Belt represents the southernmost portion of the Calabrian-Peloritani Orogen (CPO), a segment of the southern Alpine orogenic belt linking the Apennine chain, to the north, with the E–W-trending Maghrebian belt, to the south (Cirrincione et al., 2012). From the structural point of view, CPO is a nappe-pile edifice composed of distinct tectonic slices of metamorphic basement (remnants of Hercynian and Alpine orogeny) and Mesozoic-Cenozoic sedimentary covers. Its most recent evolution is strictly linked to the coexistence of extensional and compressional phenomena, as a consequence of the Tyrrhenian basin opening. This caused the activation of a regional strike-slip tectonics, mainly oriented NW-SE, known as South Tyrrhenian System (Finetti et al., 1996), active from upper Tortonian and locally still active, especially in the central and eastern portion of CPO.

The orogen segment cropping out in northeastern Sicily (i.e. Peloritani Mountains) shows several S-SE verging tectonic slices characterized by a northward increasing metamorphic grade (Atzori et al., 2003). Cirrincione et al. (1999) subdivide the nappe-pile edifice into Lower and Upper complexes. Starting from the bottom of the nappe pile, the Lower complex is characterized by very low-grade basement rocks belonging to three tectonic units (Longi-Taormina Unit, San Marco d'Alunzio Unit, and Capo S. Andrea Unit). This complex is confined on top by a cataclastic shear zone putting it in contact with phyllites of the Mandanici Unit (Atzori et al. 1984), whereas its southernmost and geometrically lower part marks the present front of the Peloritani Mountains overthrusted onto the Apennine–Maghrebian chain. This is

represented by the Taormina tectonic Line, a transpressive dextral structure, striking NW-SE, aged Miocene (Scandone et al., 1974; Lentini, 2000).

On the other hand, the Upper complex shows low- to high-grade metamorphic lithotypes of the Aspromonte Peloritani and Mandanici tectonic units (e.g. Lentini and Vezzani, 1975; Cirrincione et al., 2012). In both complexes, the crystalline formations are usually overlapped by sedimentary series spanning from Early Lias to Olocene. In particular, they contain basal red conglomerates (Verrucano *facies*, Triassic–Early Jurassic), overlain by evaporite and carbonate rocks (Lias) surmounted by radiolarites (Middle Jurassic–Cretaceous), which are overlain by marls and limestones (Scaglia *facies*, Eocene).

From tectonic point of view, eastern Sicily and southern Calabria are part of the peri-Tyrrhenian orogenic zone of the Central Mediterranean, which developed during the Neogene-Quaternary Africa–Europe collision (Dewey et al., 1989; Boccaletti et al., 1990). In particular, the Sicilian collision zone is characterized by an active WNW–ESE oriented extension process, which has given rise to the roughly N–S oriented Siculo-Calabrian Rift Zone (Monaco and Tortorici, 2000; De Guidi et al., 2003), an active fault belt extending from the Tyrrhenian side of southern Calabria to the Ionian region of eastern Sicily. In particular, the Sicilian sector is characterized by a system of normal faults striking NNW–SSE between the eastern flank of Mt. Etna and the Ionian Sea offshore of the Hyblean Plateau (Monaco et al., 1997).

During the Late Quaternary, tectonic uplifting affected eastern Sicily at regional scale (Dumas et al., 1978; Ghisetti, 1979; Tortorici et al., 2003). This process gave rise to a flight of marine terraces, distributed along the coastal areas of the region. In particular, the Taormina region is part of a 40-km long segment of the Ionian coast of northeastern Sicily, which experienced a strong tectonic uplift. This process affected the footwall of the Taormina Fault, one of the main seismogenic regional sources, and resulted in the development of

eight orders of marine abrasion platforms carved on Mesozoic carbonate rocks in the onshore from Taormina to Messina (Monaco et al., 2002). In this area, an averaged long-term uplift-rate of about 1.0–1.1 mm/year during the last 400

ky was estimated (Catalano et al., 1995; Catalano and Di Stefano, 1997).

The above-mentioned Siculo-Calabrian Rift Zone is the main responsible for the high seismic activity of the Peloritani region, characterized by the recurrence of several destructive historical earthquakes (Postpischl, 1985; Boschi et al., 1995a). Along the southern Calabria branch of the rift zone, major shocks occurred in 1659, 1783 (Jacques et al., 2001; Galli and Bosi, 2002), 1905 (Monaco and Tortorici, 2000) and 1908 (Baratta, 1910; Shick, 1977). The latter, defined as the most destructive earthquake in recorded European history, razed Messina and Reggio Calabria, which are the two main cities on both sides of the Messina Straits, and caused a devastating tsunami (Barbano et al., 2005). On the other hand, slips along the fault segments of eastern Sicily caused the strong earthquakes of 1169, 1542, 1693 (Boschi et al., 1995b; Bianca et al., 1999), and 1865 (Monaco et al., 1997).

3.3. Local geological setting

Castelmola lies on a carbonate cliff in the southernmost sector of the Peloritani Mountains, where several fault segments strongly affect the local geology, leading to numerous stratigraphic repetitions of the Longi Taormina Unit (LTU). It crops out in a NW-SE oriented belt, about 10 km wide, from the Tyrrhenian to the Ionian coasts of Sicily (De Capoa et al., 1997).

The stratigraphic succession is herein described, from the bottom to the top, as the result of a detailed geological survey, which allowed mapping the main formations and their mutual geometrical relationship (**Figure 5**).

The bottom of the unit is represented by a Variscan epimetamorphic basement of sub-greenschist *facies* mainly composed of metapelites and quartz schists with minor metabasites and porphyroids (Atzori et al., 2001). In particular, the metapelites group crops out in the northern sector of Castelmola village and is characterized by a schistose texture (Figure **6**), with abundance of chlorite, sometimes showing relicts of fold hinges. On the other hand, metabasites and porphyroids, representing the oldest eruptive products of the Paleozoic sequence of Peloritani Range (Acquafredda et al., 1991; Trombetta et al., 2004), crop out along the access road to the village and are characterized by a structure from massive to slightly foliated and sometimes are affected by intense degree of fracturing (Figure **7**). They keep some features of the original porphyritic texture, such as phenocrysts of plagioclase, quartz and k-feldspar.

A late Triassic redbeds succession, known as “Verrucano” (Dueè, 1969), lies unconformably on the metamorphic basement. It is exclusively made up of clastic rocks, such as red quartzarenites and minor quartzose conglomerates and red-purple mudrocks. Within LTU the thickness of this level, occurring in lenses, is up to 20 m (Figure **8**). From a depositional point of view, Verrucano conglomerates represent fluvial deposits in a transitional environment with no evidence of stratification. In the study area, it widely crops out along the access

road to the village, where the transition with the overlaying carbonate succession is marked by an evident change in color, while it is hidden by debris and vegetation in the northeastern sector.

Lower Liassic greyish-white limestones and dolostones in carbonate platform *facies* (Lentini et al., 2006) represent the most relevant portion of the sedimentary covers of LTU in the study area, where the maximum thickness crops out. At the bottom of this formation, detrital and oolitic limestones and yellowish marls (from now on referred to as "limestones") are recognizable in 10 to 60 cm thick strata (Figure **9**). This succession is affected by a heteropic transition to a saccaroid dolostone level, clearly identifiable thanks to its coarse and crystalline structure and local pink-yellowish tinges. Dolostone outcrops do not show any bedding surface, unlike limestones, and appear intensely jointed and with calcite veins filling some fractures (Figure **10**). In the upper portion of this formation, sometimes, a few silt-sand levels made of quartz and cut by an erosion surface occur.

The top of the local stratigraphic succession is represented by alternated marly limestones and marls belonging to the "Medolo" Formation (Figure **11**). This shows signs of deformation, i.e. folds with associated convergent cleavage fans with centimetre-spaced microlithons, and a fossiliferous record of deformed Ammonites (Somma et al., 2005).

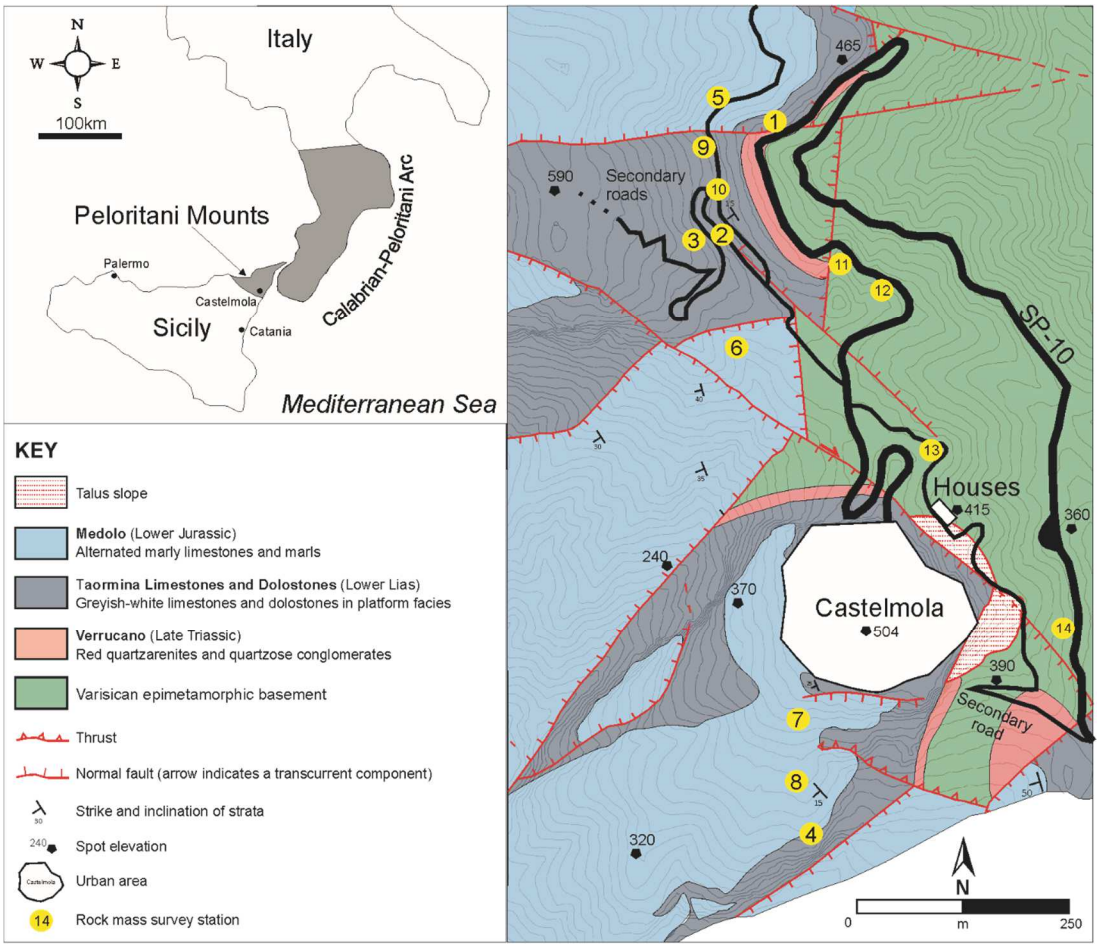

Figure 5: geological map of the Castelmola area, with main urban elements highlighted. Numbers in the yellow circles are for the rock mass survey stations: 1) Dol-1; 2) Dol-2; 3) Dol-3; 4) Dol-4; 5) Med-2; 6) Med-1; 7) Med-4; 8) Med-3; 9) Lim-1; 10) Lim-2; 11) Por-1; 12) Por-2; 13) Por-3; 14) Por-4.

Figure 6: a) semischist outcrop in the northern sector of the study area; b) detail of the evident schistosity of this rock.

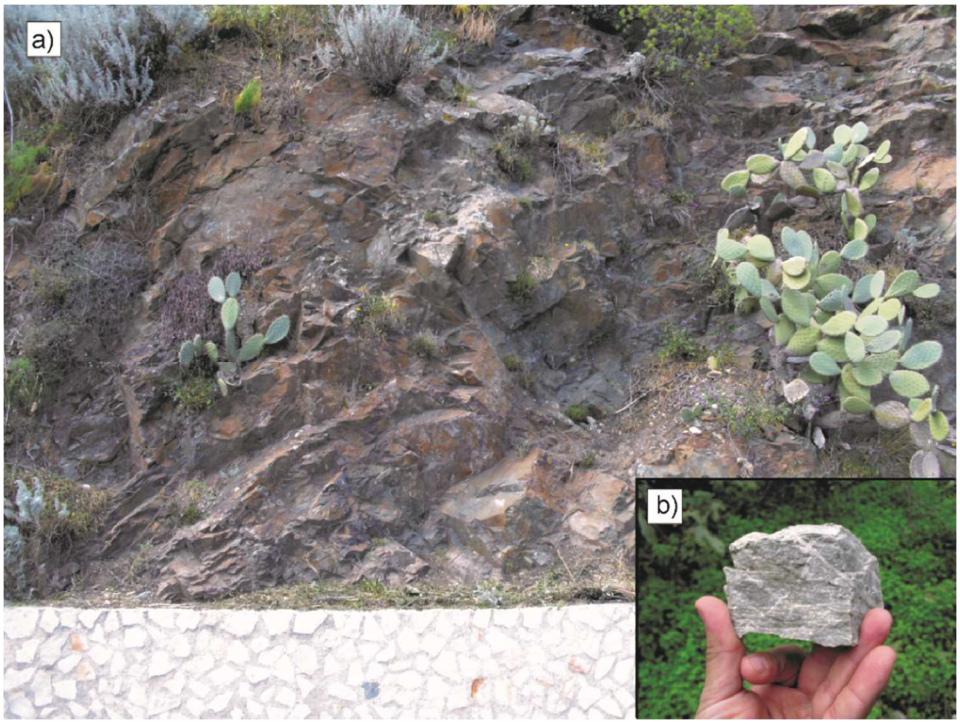

Figure 7: a) porphyroid outcrop along SP10; b) detail of a green-grayish sample.

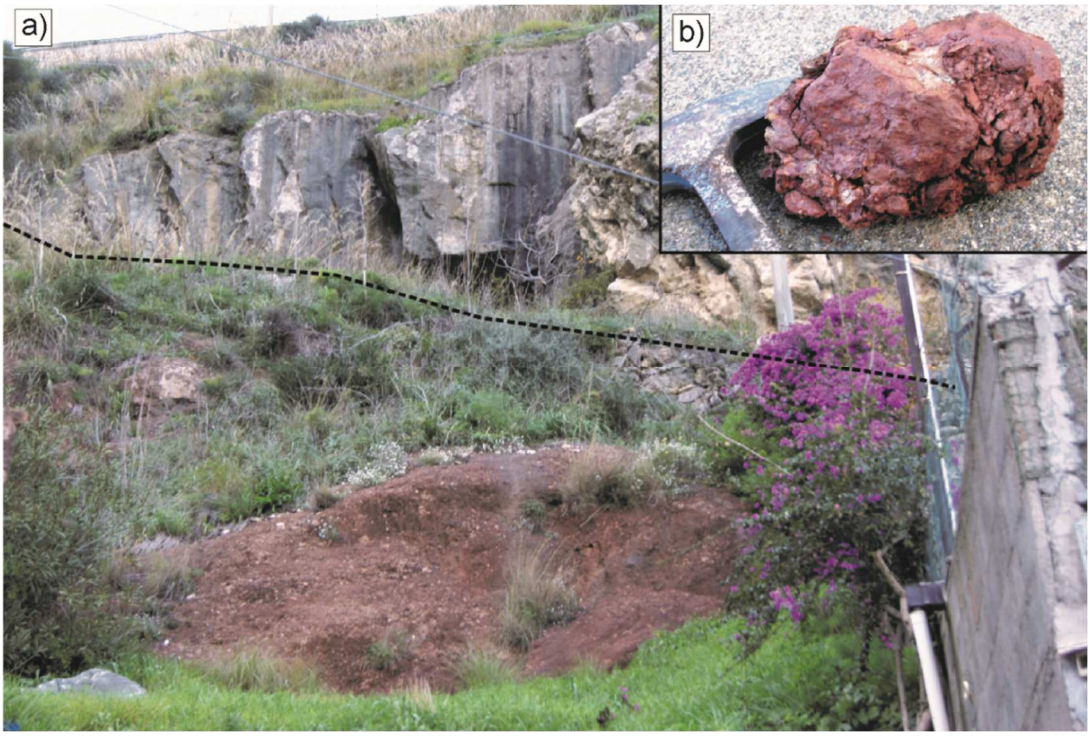

Figure 8: a) red conglomerate in Verrucano *facies* slong SP10. The geological limit with the upper limestone formation is marked by the dashed line; b) detail of a conglomerate sample.

Figure 9: outcrop of limestone with horizontal bedding surfaces.

Figure 10: intensely jointed dolostone rock mass.

Figure 11: marly limestones and marls belonging to the “Medolo” Formation.

3.4. Documented landslides

Several rockfalls have affected the study area over time, causing severe damage to structures and infrastructures along with discomfort to the population. Information on some of these landslides is available in the national databases of AVI (Italian Areas of Vulnerability; AVI Project, 1998) and P.A.I. (Hydro-Geomorphologic Setting Plan, 2006). The latter, whose function is also to identify high hazard and risk areas, classifies the studied site as a high hazard and risk zone. Its documents report 66 instability areas (2.83 km^2), 19 of which (1.85 km^2) are labelled with the highest hazard level.

In 1952, the local daily newspaper La Gazzetta del Sud published an article on landslide movements occurring after heavy rain along the "only way of access to Castelmola". More recently, the main documented events, which interrupted SP10, occurred in 1996, 1997 and 1999, when rockfalls from the northern carbonate cliff, involving significant volumes of rock, occurred (Ferrara and Pappalardo, 2005; Pappalardo et al., 2014). With respect to the 1999 event, the AVI database reports that a falling boulder crashed into a car, fortunately causing no victims. After such episodes, the northern cliff was consolidated by means of deep anchors, concrete retaining structures and drainage gullies at the base of the slope.

In 2006, a boulder of about 6 m^3 fell close to a group of houses in the southeastern sector of the village, in the area herein defined as CA, prompting the municipal administration to perform urgent provisional works in order to install rockfall protection barriers behind the threatened houses (Pappalardo and Mineo, 2015) (Figure **12**a).

In February 2012, two landslides occurred at MRA: the first overcame a retaining wall and invaded SP10 near a narrow curve; the second took place only 100 m away, destroying the wire mesh protecting the cliff (La Sicilia, 2012). During the night between 29 February and 1 March 2012, another

landslide affected SP10 and threatened the water pipeline serving Taormina (available at: http://www.tempostretto.it, 2012).

On 29 August 2014, three blocks detached from the highest portion of the cliff behind the group of houses already threatened in 2006 (Figure **12**b). All the three blocks rebounding and rolling along the slope bypassed the existing rockfall barrier; in particular, one block hit the downstream houses (Figure **12**c), one was slowed down by slope vegetation and one rebounded as far as the SP10, causing a temporary disruption of the road.

On 23 February 2015, two falling blocks at MRA reached the road and stopped at a bend, leading to an emergency meeting of the authorities and to a further disruption of the infrastructure (Figure **12**d-e).

These are only some of the numerous events occurred in the area; in fact, several landslides are not mentioned in the chronicles and most of the information regarding past events have been reported orally by local residents. Nevertheless, although the traces of such mass movements are easily erased by vegetation, several boulders lie on the margin of SP10 and along the slopes (average size 0.5×0.4×0.5 m^3), evidencing how often rockfalls occur in this area constituting a threat to public safety.

Figure 12: a) view of CA; b) group of houses at CA after the 2014 rockfall; c) detail of the block crushed into a house; d) view of MRA after the 2015 rockfall; e) 2015 blocks on the SP10.

CHAPTER 4

ROCK MASS SURVEY

4.1. Theoretical background

Since the rock mass is defined as a complex consisting of the rock matrix and of the discontinuities, it mainly behaves as a discontinuous medium, with the discontinuities controlling its mechanical attitude. It is therefore essential that both the structure of a rock mass and the nature of its discontinuities are carefully described in addition to the lithological description of the rock type. To this purpose, the International Society for Rock Mechanics (ISRM, 2007) provided a collection of recommendations aimed at achieving a degree of uniformity in the description of discontinuity in rock masses, *as an aid to communication between the geologist and the engineer*.

In this paragraph, a description of the field parameters to take into account during a rock mass survey, according to ISRM (2007), is provided.

4.1.1. Quantitative description of discontinuities

There are two basic levels at which a rock mass survey may be carried out, depending upon the amount of detail that is required. The *subjective* (biased) survey is aimed at describing only those discontinuities that are likely to be relevant, while the *objective* (random) survey takes into account all the discontinuities intersecting a fixed line (scanline) or falling within a fixed area (window) of the slope face.

Regardless of the chosen approach, it is clear how the main subjects of a rock mass survey are the discontinuities. ISRM defines as discontinuity "any mechanical discontinuity in a rock mass having zero or low tensile strength". It is the collective term for most types of joints, weak bedding planes, weak schistosity planes, weakness zones and faults.

For each discontinuity selected for the rock mass description, the following parameters must be carefully surveyed in field:

- *Orientation*

  It is the *dip* of the line of the steepest declination measured from horizontal, along with the *dip direction* measured clockwise from the true north. This is one of the main parameters controlling the instability features of a rock mass, and the shape of the individual blocks. It can be measured in field by a compass and a clinometer and the result is expressed by three and two digit numbers, for dip direction and dip respectively, separated by a line (e.g. dip direction/dip: 220/55). The pair of numbers represents the dip vector (**Figure 13**).

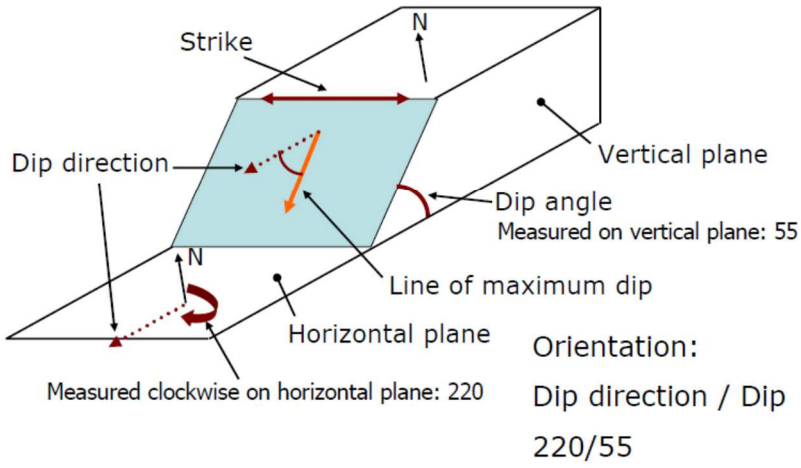

Figure 13: sketch of the orientation of a discontinuity plane

- *Spacing*

  It is a basic measurement of the distance between one discontinuity and another, playing a key role in the size of individual blocks of intact rock and, in some cases, even affecting the mode of failure of a rock mass.

  Discontinuity spacing measurements can be separated into the following three forms (Wines and Lilly, 2002):

  1) *Total spacing:* the distance between two adjacent discontinuities, measured along a line of general, but specified, location and orientation.

2) *Set spacing*: the spacing between two adjacent discontinuities from a particular discontinuity set, measured along a line of general, but specified, location and orientation.

3) *Normal set spacing*: the set spacing measured along a line that is normal to the mean orientation of a particular set.

Based on the spacing values, discontinuities can be classified according to **Table 2**.

Table 2: terminology for the description of discontinuities with respect to their spacing (ISRM, 2007).

Description	Spacing (mm)
Extremely close spacing	<20
Very close spacing	20-60
Close spacing	60-200
Moderate spacing	200-600
Wide spacing	600-2000
Very wide spacing	2000-6000
Extremely wide spacing	>6000

- *Persistence*

  It is the areal extent or penetration length of a discontinuity within the rock mass (**Figure 14**). It represents one of the most important parameters and, at the same time, the most difficult to quantify. It can be assessed by observing the discontinuity trace lengths on the slope face. In fact, often the discontinuities of one particular set will be more continuous than those of the other sets. Therefore, the minor sets will tend to terminate either against the primary features or in the solid rock, for example. It has been demonstrated that discontinuities showing both terminations on the slope face are generally smaller than

discontinuities showing one or no termination (Piteau, 1973). Nevertheless, the estimation of persistence has to be purposely weighted in the direction of conservatism, because it strongly affects the shear strength along the discontinuity (**Table 3**).

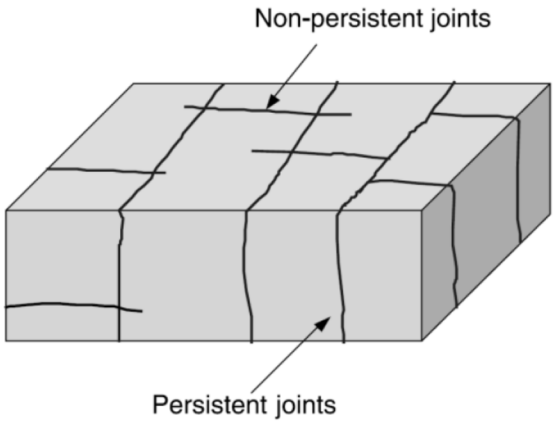

Figure 14: persistent joints versus non-persistent joints (after Kim et al., 2007).

Table 3: terminology for the description of persistence (ISRM, 2007).

Description	Persistence (m)
Very low persistence	<1
Low persistence	1-3
Medium persistence	3-10
High persistence	10-20
Very high persistence	>20

- *Roughness*

It is defined as "the surface roughness and waviness relative to the mean plane of a discontinuity". It is an important component of its shear strength, especially in the case of unfilled joints. The roughness of a discontinuity includes two features: the *waviness*, which is a large scale undulation causing dilation phenomena during shear displacement along interlocked and in-contact discontinuities, and the

unevenness, representing the small scale roughness, which tends to be damaged during shear displacement. In other words, *waviness* affects the initial direction of shear displacement, while *unevenness* affects the shear strength along the plane.

Roughness can be assessed by linear profiles acquired parallel to the dip vector of a discontinuity plane and its description will be limited to descriptive terms, from rough to slickensided (**Figure 15**).

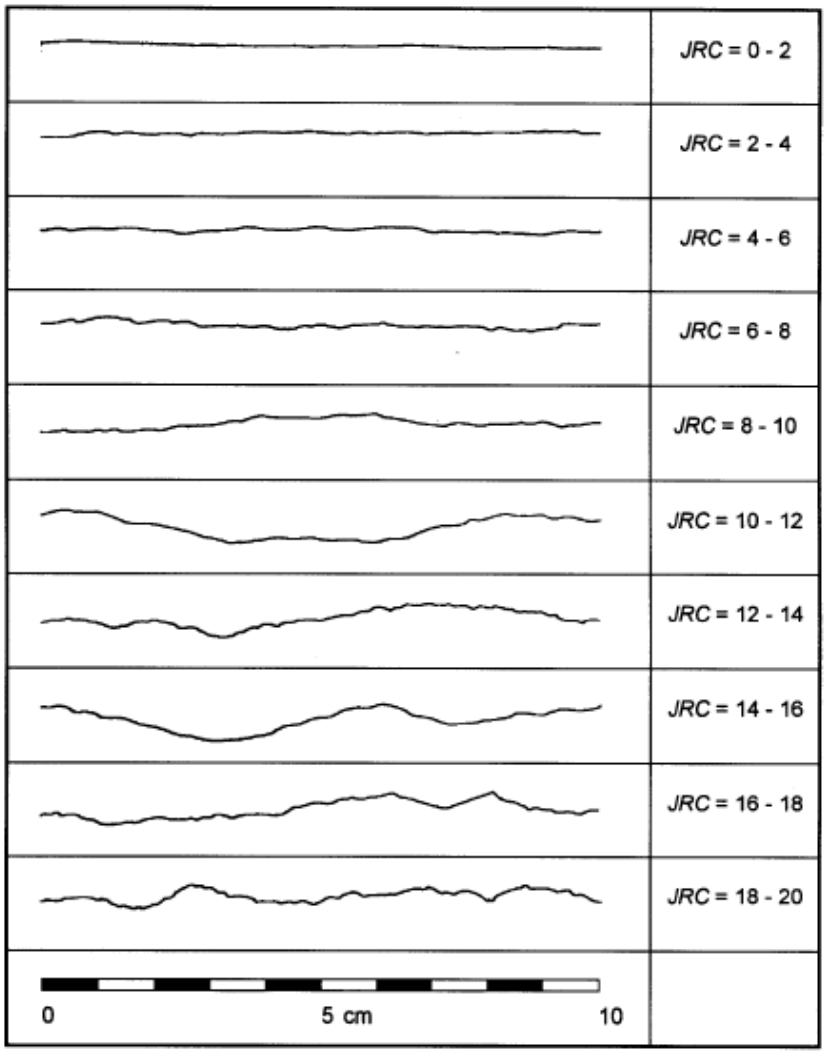

Figure 15: typical roughness profiles and corresponding range of JRC (after Barton and Choubey, 1977).

The main purpose in describing such parameter is to facilitate the estimation of shear strength, with particular reference to unfilled

discontinuities. In fact, shear strength consists of a maximum (peak) or minimum (residual) friction angle plus a contribution (i) due to large-scale waviness, if present. Thus, the shear strength τ (peak or residual) depends on such coefficients, according to the following equation (1) (Patton, 1996):

$$\tau = \sigma'_n \tan(\varphi + i) \qquad \text{(eq.1)}$$

where σ'_n is the effective normal stress.

Roughness profiles can be also used to assess another geomechanical parameter, known as Joint Roughness Coefficient (JRC), by matching the obtained profile to those proposed by Barton and Choubey (1977) (**Figure 15**). This coefficient can be also taken into account for the empirical estimation of the peak friction angle (φ_{peak}) of a discontinuity, through the following equation (2)

$$\varphi_{peak} = JRC\ log_{10}\left(\frac{JCS}{\sigma'_n}\right) + \varphi_r \qquad \text{(eq. 2)}$$

where JCS is the Joint Compressive Strength following described and φ_r is the residual friction angle, which can be estimated by the ratio between the Schmidt hammer rebound (r) obtained on the weathered joint wall and the rebound (R) obtained on the unweathered rock (Barton and Choubey, 1977).

- *Wall Strength*

It is the compressive strength of the rock comprising the walls of a discontinuity and represents a very important component of shear strength and deformability of the rock mass. In fact, rock masses are

frequently weathered along the discontinuity surfaces, thus they can offer a lower wall strength than the unweathered rock. For this reason, a description of the state of weathering, which can range between grade I (fresh rock) and VI (residual soil), is an essential part of the description of the wall strength. One of the main application for the numerical estimation of the wall strength is the Schmidt Hammer Test. It is a speed test, performed by a L-type rebound hammer (Schmidt Hammer), which measures the rebound of a spring-loaded mass impacting against the surface of the rock. Such rebound depends on the hardness of the rock and its numerical value can range from about 10 to 60. The lowest number applies to *weak* rocks (uniaxial compressive strength UCS < 20 MPa), while the highest number applies to *very strong* and *extremely strong* rocks (UCS > 150 MPa). The rebound number is then employed for the empirical estimation of the compressive strength of the rock surface or Joint wall Compressive Strength (JCS), which can be easily carried out by relating the rebound number and the dry density of tested rock, according to Deere and Miller (1966) (**Figure 16**).

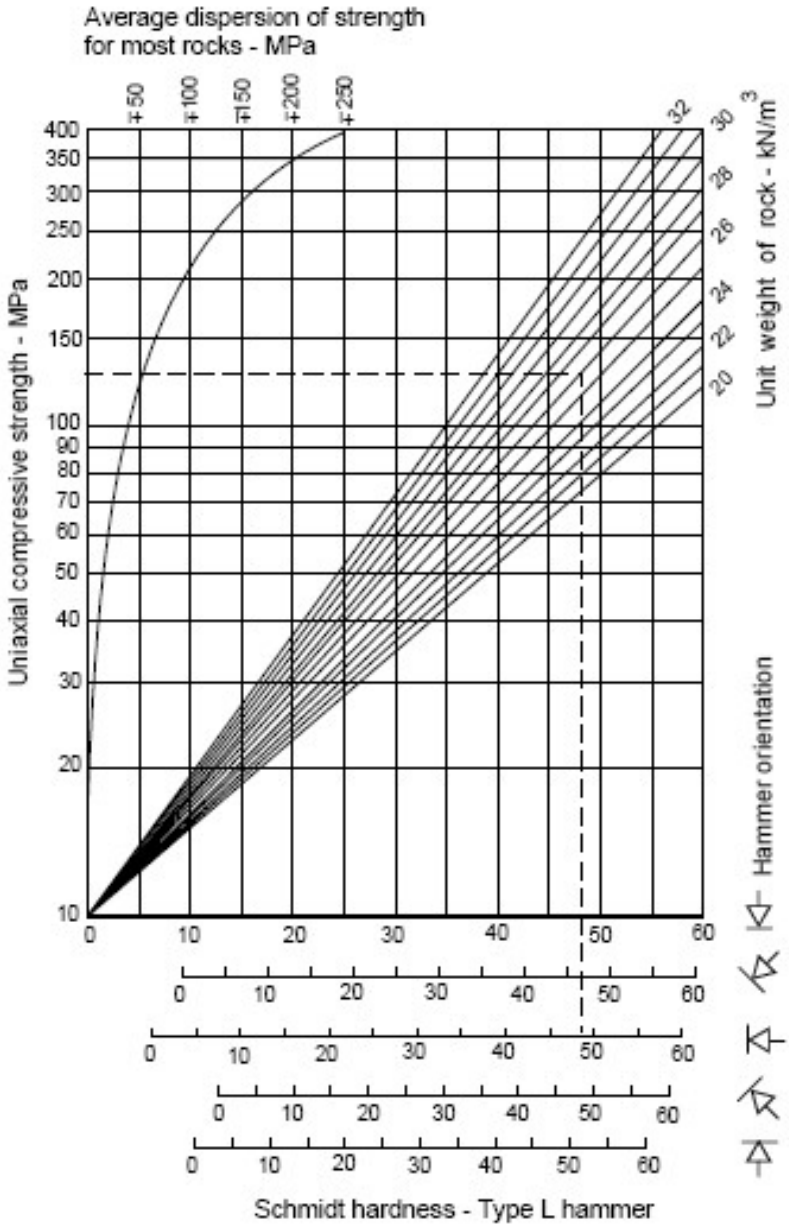

Figure 16: correlation chart for Schmidt (L) hammer, relating rock dry density, compressive strength, rebound number and hammer orientation (after Deere and Miller, 1966).

- *Aperture*

  Aperture is the perpendicular distance separating the adjacent rock walls of an open discontinuity, in which the intervening space is filled with air or water (**Figure 17**). Discontinuities that have been filled also come under this category if filling material has been washed out locally.

It is important to remind that the aperture visible in a rock exposure is a disturbed aperture, due either to localized surface weathering or to the excavation mode. Therefore, measured apertures are likely to be larger than those existing within the rock mass. Based on the measured values, discontinuities can be grouped into *closed*, *gapped* and *open* categories (**Table 4**).

Table 4: terminology for the description of aperture (ISRM, 2007).

Aperture	Description	
<0.1 mm	Very tight	
0.1-0.25 mm	Tight	"Closed" features
0.25-0.5 mm	Partly open	
0.5-2.5 mm	Open	
2.5-10 mm	Moderately wide	"Gapped" features
>10 mm	Wide	
1-10 cm	Very wide	
10-100 cm	Extremely wide	"Open" features
>1 m	Cavernous	

- *Filling*

  It is the material separating the adjacent rock walls of a discontinuity and that is usually weaker than the parent rock. Typical filling materials are sand, silt, clay, breccia, gouge, quartz and calcite veins. The perpendicular distance between the adjacent rock walls is defined as *width* of the filled discontinuity (**Figure 17**). Due to the enormous variety of occurrences, filled discontinuities display a wide range of physical-mechanical behavior, with particular reference to their shear strength, deformability and permeability.

For each filled discontinuity, width, weathering grade, mineralogy, water content and particle size have to be evaluated. The detail of presentation of results depends on the importance of the individual discontinuity (or set) to the project as a whole.

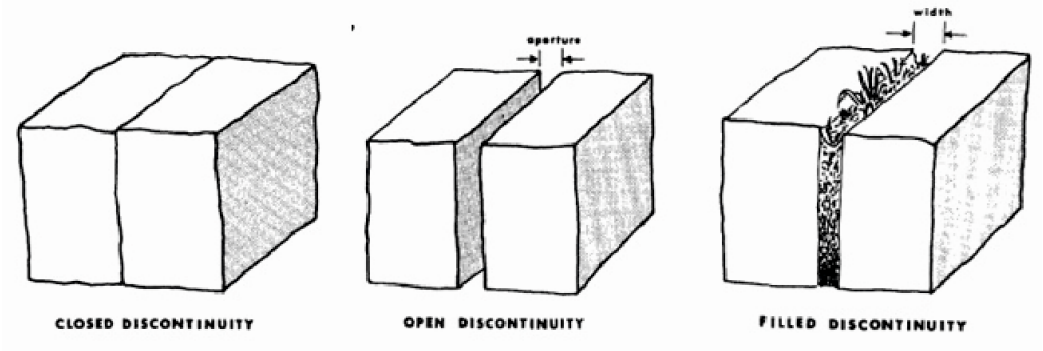

Figure 17: Sketch of discontinuities with different aperture and filling (after ISRM, 2007)

- *Seepage*

  This term indicates water flow and free moisture visible in individual discontinuities or in the rock mass as whole. Water seepage results mainly from flow through water conducting discontinuities and its rate is proportional to the local hydraulic gradient. Based on the seepage rate and on the presence of filling material, discontinuities can be described according to 6 classes (**Table 5**).

Table 5: terminology for the description of seepage (ISRM, 2007).

Seepage rating	Description
I	Very tight and dry discontinuity. No possible water flow.
II	Dry discontinuity with no evidence of water flow.
III	Dry discontinuity with evidence of water flow.
IV	Damp discontinuity, but no free water present.
V	Seepage present, occasional drops of water.
VI	Continuous flow of water.

- *Number of sets*

  This can be considered one of the dominant features of rock slope stability and it is defined by grouping discontinuities with respect to their mean orientation. Such procedure will be discussed in detail in paragraph 4.1.2.

- *Block size*

  Block size is an extremely important indicator of rock mass behavior. It is up to the spacing, the number of sets and the orientation and persistence of discontinuities. Rock masses composed of large blocks tend to be less deformable and more suitable for engineering stabilizing works. On the other hand, a small block size could cause the potential failure mode resembling a soil.

4.1.2. Graphical representation of geostructural data through stereographic projection

Once all the field data are retrieved, the analysis of the orientation and distribution of discontinuities is required, in order to achieve a model of the geostructural setting of the rock mass. This is carried out by representing the three-dimensional orientation data in two dimensions through the stereographic projection. Such procedure allows removing one dimension from consideration, so that lines or points can represent planes, and points can represent lines. Nevertheless, stereographic projections do not allow representing the position or size of the discontinuity, as they take into account only angular relationships between lines and planes.

Such projections consist of a reference sphere showing a horizontal equatorial plane and an orientation fixed towards North. All the geostructural features (planes and lines) with specific plunge and trend are positioned, in an imaginary sense, so that the axis of the feature passes through the center of the reference sphere. The intersection of the feature with the lower half of the reference sphere defines a unique line on the surface of the reference hemisphere. For a plane, such intersection is a circular arc called “great circle” (**Figure 18**a), while for a line it is a point (**Figure 18**b). Otherwise, an alternative way of representing the orientation of a plane is the *pole* to the plane, which is defined as the point on the surface of the reference sphere that is pierced by a radial line in a direction normal to the plane (Wyllie and Mah, 2004). This is a valuable way to represent a plane, because a single point can represent its complete orientation in the space (**Figure 18**c-d).

The two types of stereographic projections are the polar and equatorial schemes. In rock mechanics, only the equatorial net is employed, because the polar projection allows plotting only poles (**Figure 19**).

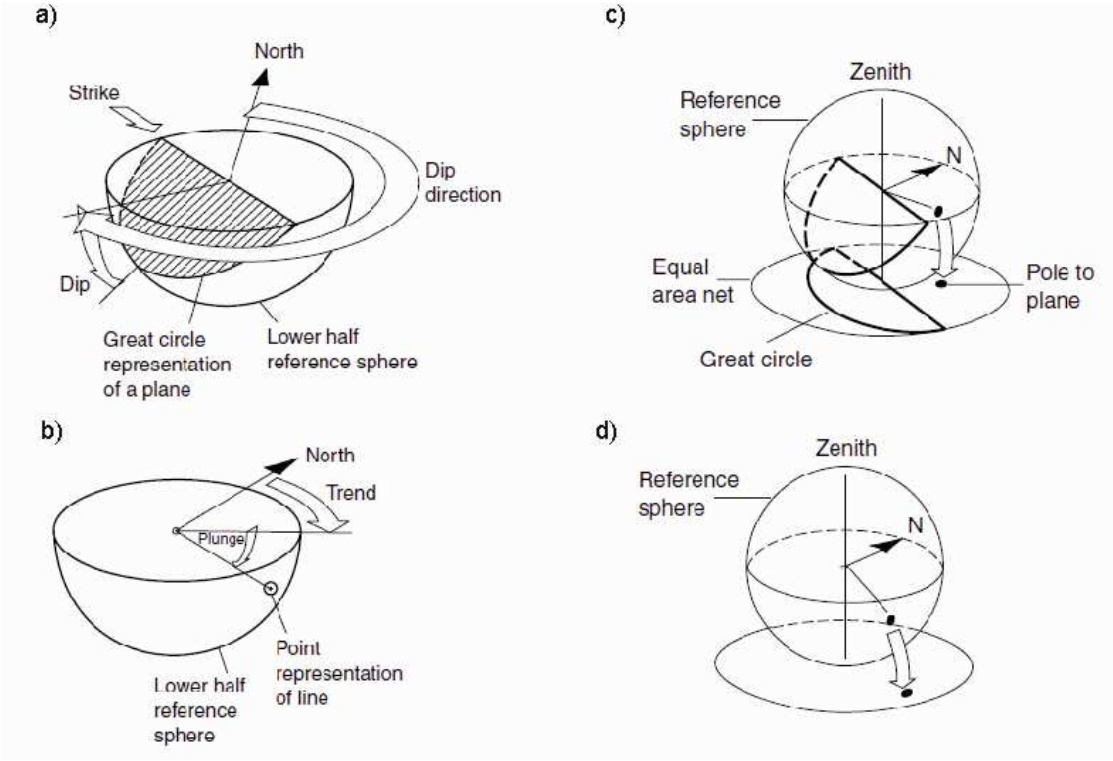

Figure 18: stereographic representation of planes and lines on lower hemisphere of a reference sphere (modified after Wyllie and Mah, 2004): a) plane projected as great circle; b) isometric view of a line (plunge and trend); c) plane projected as a great circle and corresponding pole; D) line projected as a pole.

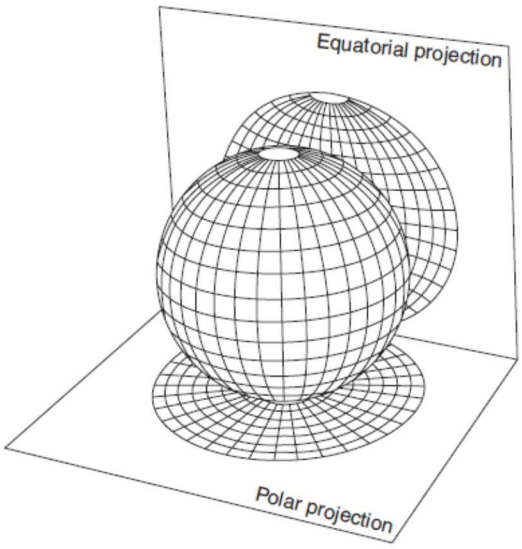

Figure 19: polar and equatorial projection of a sphere.

All natural discontinuities, whose orientation data are plotted on stereograms, are characterized by variable orientations that result in scatter of the pole

plots. Therefore, it can be difficult to distinguish poles belonging to different sets, especially when a certain number of discontinuity systems affect the rock mass. For this reason, the statistical processing of plotted data is a common practice, in order to group all the surveyed discontinuities into sets for the proper analysis. Such statistical procedure is named "contouring" and it is aimed at analyzing mean and maximum pole concentrations, to visualize the clustering of orientation data not immediately evident from the pole plot. The contour can be calculated, for example, by the Fisher distribution method (Fisher, 1953), and represents an interval of probability (in percent) of pole occurrence within a specified angular distance of a given orientation. In this way, the main discontinuity systems are defined and the most representative plane for each set can be plotted for further specific analyses (**Figure 20**).

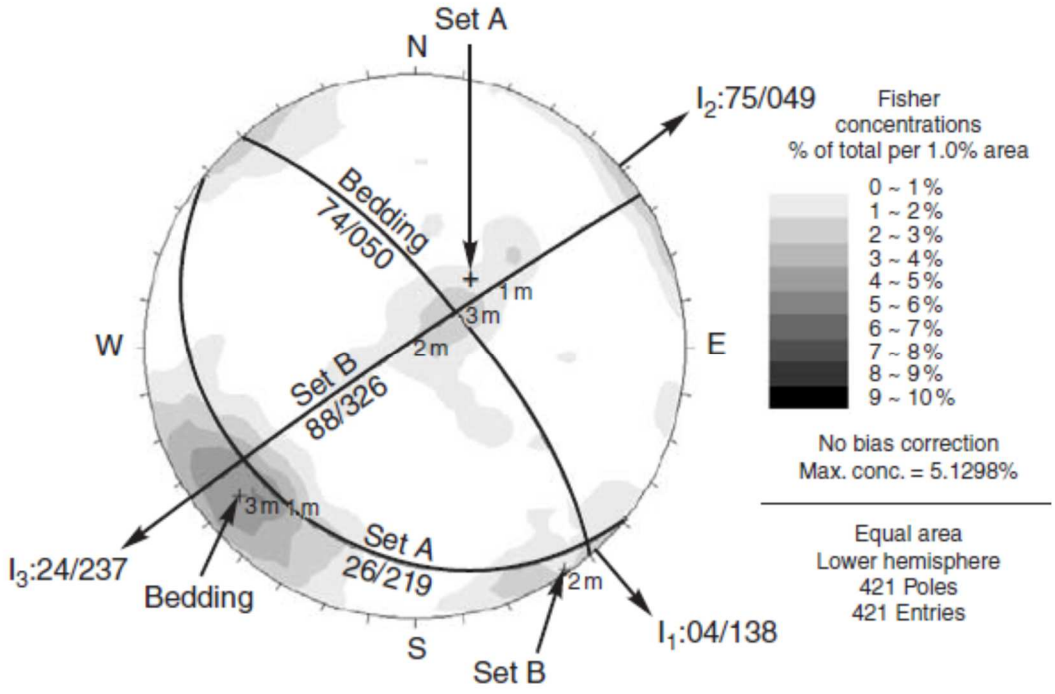

Figure 20: example of a contoured plot of geostructural data with great circles corresponding to mean orientation of bedding and two orthogonal joint sets, and lines of intersection between planes.

4.1.3. Graphical representation of geostructural data through joint rosettes (ISRM, 2007)

Another method of plotting and presenting a large number of orientation measurements in a qualitative manner is by means of joint rosettes. In this case, data are plotted on a simplified compass rose, marked from 0° to 360°, with radial lines generally at 10° intervals. The number of observations are represented along the radial axes, using numbered concentric circles. The resulting strike "petals" have mirror images about the center of the rosette (**Figure 21**).

Such a representation is very useful to evaluate the main direction of discontinuities, which are usually related to regional tectonic systems. On the other hand, the rosette diagrams tend to misrepresent some data. In fact, large concentrations are exaggerated, while small concentration are suppressed, due to the fact that areas in each angle sector vary with the square of the radial coordinate, whereas in a true histogram the areas of each bar or sector should vary with the frequency and not with its square.

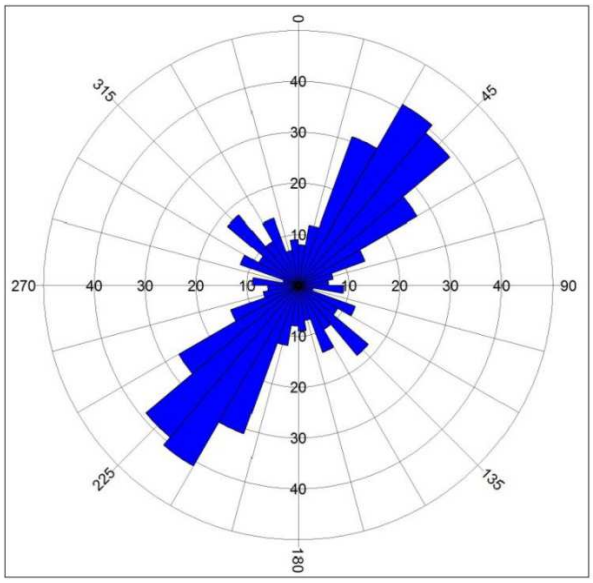

Figure 21: example of a rosette plot, showing a high frequency of NE-SW systems.

4.2. Surveyed rock masses

According to ISRM recommendations (ISRM, 2007), geostructural and geomechanical surveys were carried out at 14 measurement stations (**Figure 5**), with particular reference to the intensely fractured rock masses threatening structures and infrastructures at CA and MRA. In particular, 4 stations were placed at dolostone rock masses (from now on referred to as Dol), 2 at limestone outcrops (Lim), 4 at porphyroid rock masses (Por) and 4 at Medolo outcrops (Med).

Discontinuity systems were distinguished with respect to their orientation, according to the contour method based on the Fisher distribution (Fisher, 1953), and named according to their persistence value using the letter K for persistence up to 10 m and R for persistence >10 m.

4.2.1. Dol-1 Station

The measurement station was placed at a sub-vertical slope in the northern sector of the study area. The slightly weathered rock mass is crossed by 4 discontinuity systems, mainly striking NE-SW and NW-SE according to the regional tectonic setting (**Figure 22**). These are both open (K1 and K2) and closed (K3 and K4), sometimes filled with soft weathered material, and show spacing values ranging between 20 and 600 cm. JRC values are between 4 and 12, while JCS (calculated considering a density of 27 kN/m^3 for dolostones) from 33 to 56 MPa (**Table 6**).

Table 6: main features of discontinuities surveyed at Dol-1 station (slope face 160/87).

Discontinuity system	Spacing (cm)	Persistence (m)	Aperture (mm)	JRC	Filling	Hydraulic condition	JCS (MPa)
K1 (085/79)	200-600	3-10	2.5->5	8-10	Soft	Damp	56
K2 (307/79)	20-60	3-10	2.5->5	8-10	Soft	Damp	53
K3 (219/88)	20-60	3-10	<0.1	10-12	None	Damp	41
K4 (210/49)	20-60	1-3	<0.1	4-6	None	Damp	33

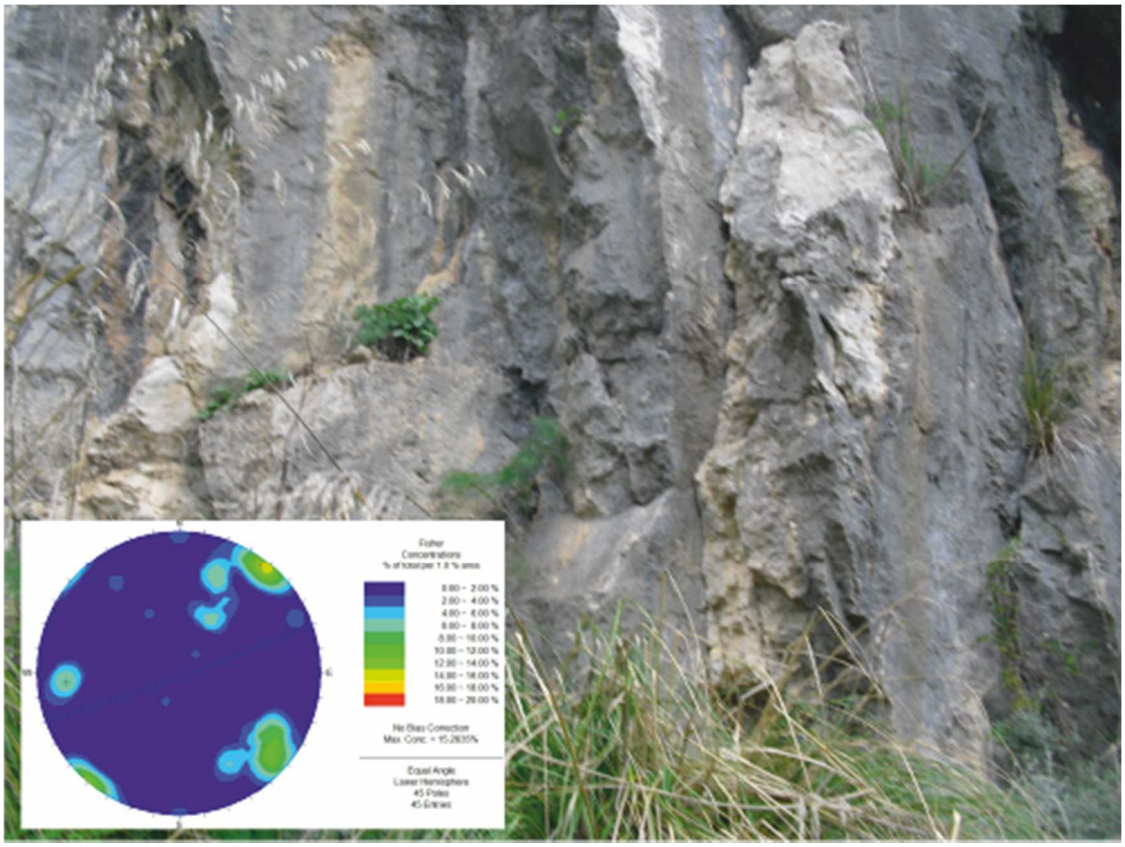

Figure 22: Dol-1 rock mass and contour plot of the surveyed discontinuities.

4.2.2. Dol-2 Station

The rock mass taken into account herein shows a complex setting from the geostructural point of view. In fact, it is fractured by five discontinuity sets with a generally close spacing, which cause a great fragmentation of the rock mass into small blocks with average size of some cubic centimeters. The slope, located in the close proximity of a fault belonging to the South-Tyrrhenian system, was particularly hard to survey because of the great amount of joints and the presence of some crushed portions. Discontinuity surfaces were slightly weathered and sometimes showed striations caused by possible tectonic movements. Although there is a prevalence of systems striking N-S (**Figure 23**), according to the direction of a fault segment surveyed eastward, the average orientation of discontinuities is comparable to those surveyed at Dol-1.

Table 7: main features of discontinuities surveyed at Dol-2 station (slope face 040/87).

Discontinuity system	Spacing (cm)	Persistence (m)	Aperture (mm)	JRC	Filling	Hydraulic condition	JCS (MPa)
K1 (108/59)	2-20	<1-10	1-5	4-6	None	Damp	41
K2 (352/39)	2-20	<1	<0.1	4-6	None	Damp	31
K3 (193/68)	2-20	<1	1-5	4-6	None	Damp	35
K4 (274/61)	2-20	<1	1-5	6-8	None	Damp	33
K5 (039/50)	2-20	<1-10	<0.1	2-4	None	Damp	76

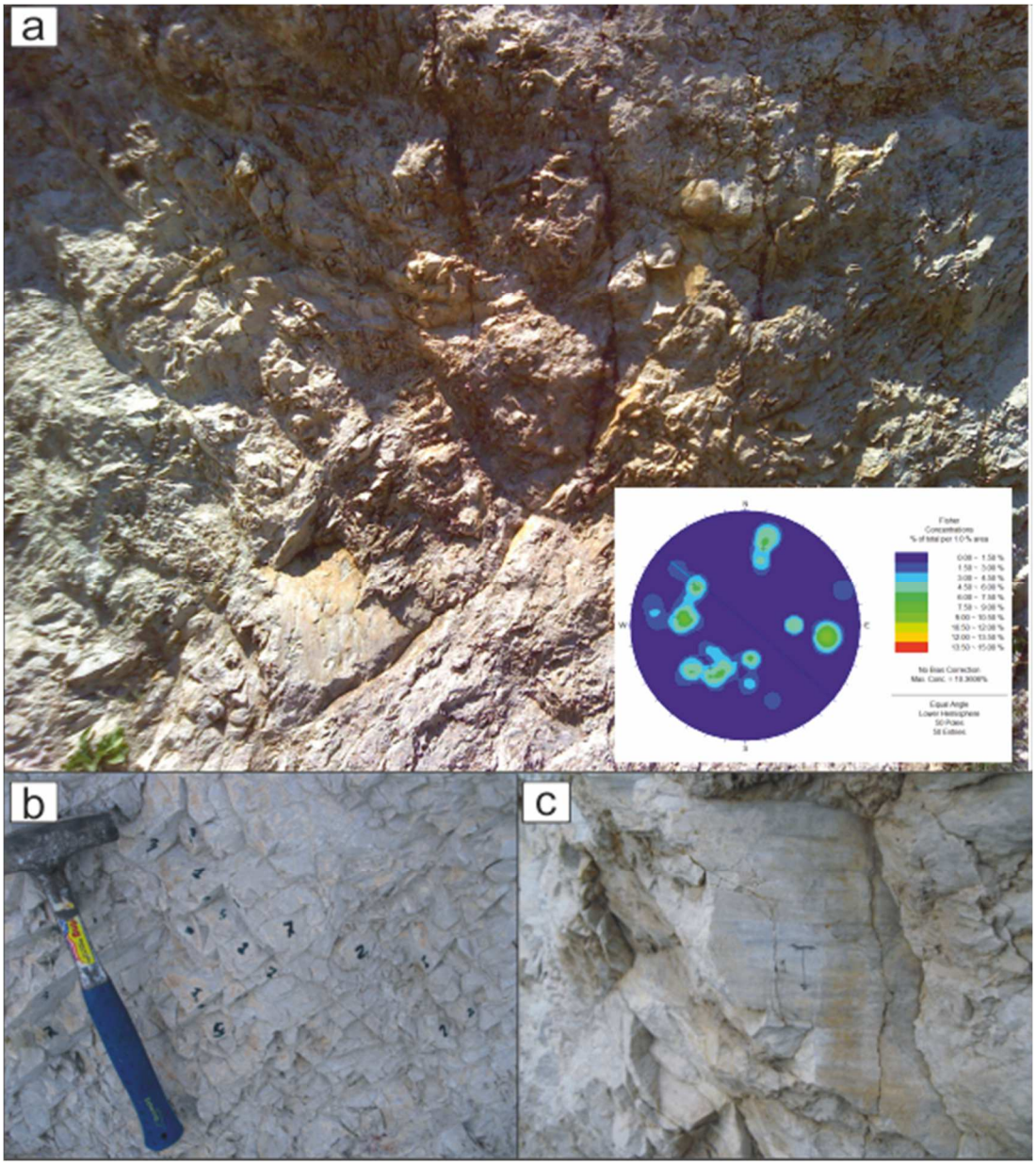

Figure 23: a) Dol-2 rock mass and contour plot of the surveyed discontinuities; b) particular of an intensely fractured sector; c) striations occurring at some planes.

4.2.3. Dol-3 Station

This survey station is placed at a 10 m-high rock slope (dip direction/dip 056/65), which is characterized by an intense degree of fracturing (**Figure 24**a). Five main discontinuity sets cross the rock mass with a generally close spacing, leading to a great fragmentation of the rock (**Figure 24**b). Discontinuities are mostly filled with soft material, even though some fractures belonging to K1

system hold hard material, probably calcite originated by chemical dissolution (**Figure 24**c). Spots of vegetation occur along the slope, index of potential water circulation in the rainy season.

Table 8: main features of discontinuities surveyed at Dol-3 station (slope face 056/65).

Discontinuity system	Spacing (cm)	Persistence (m)	Aperture (mm)	JRC	Filling	Hydraulic condition	JCS (MPa)
K1 (122/57)	2-20	<1	1-5	10-12	Hard	Damp	39
K2 (196/72)	2-20	<1	0.1-1	8-10	None	Damp	33
K3 (282/57)	2-20	<1	1-5	8-10	Soft	Damp	35
K4 (046/50)	2-20	<1-10	1-5	10-12	Soft	Damp	33
K5 (247/46)	2-20	<1	1-5	6-8	Soft	Damp	35

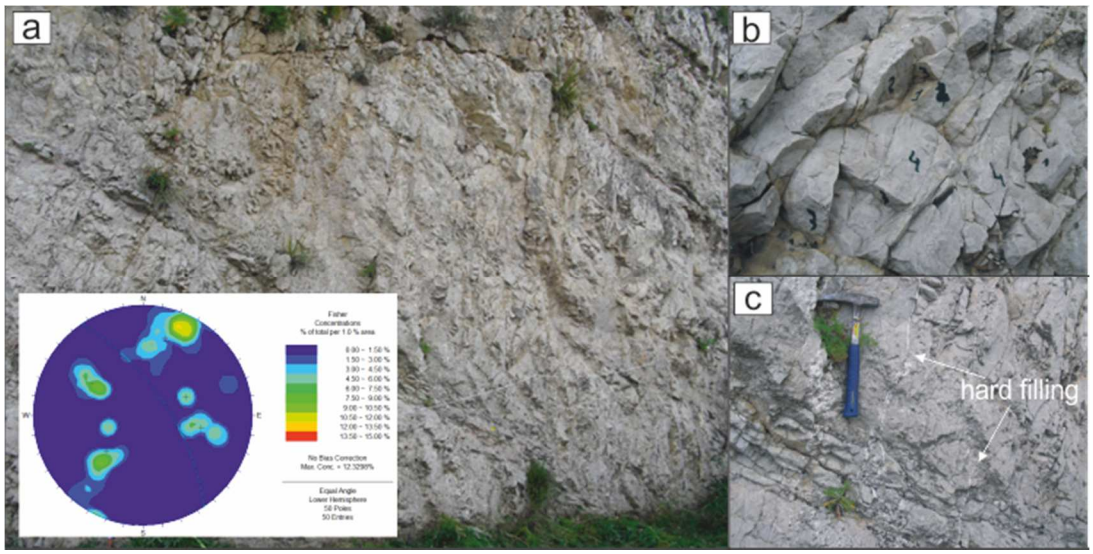

Figure 24: a) Dol-3 rock mass and contour plot of the surveyed discontinuities; b) particular of an intensely fractured sector; hard material filling K1 set.

4.2.4. Dol-4 Station

This survey station is located in the southern sector of the study area, in a tectonically less disturbed spot. In fact, the rock mass considered herein is at the top of the monocline on which Castelmola lies and looks different from the rock masses previously described. Five main discontinuity systems were surveyed, including a bedding set (**Figure 25**). They show, on average, a close spacing and a low persistence, except for the bedding system whose persistence was assumed >20 m (**Table 9**).

There is a prevalence of structures striking NE-SW, which is the direction of a normal fault segment surveyed in the close proximity of the station.

Table 9: main features of discontinuities surveyed at Dol-4 station (slope face 224/67).

Discontinuity system	Spacing (cm)	Persistence (m)	Aperture (mm)	JRC	Filling	Hydraulic condition	JCS (MPa)
K1 (139/79)	6-20	<1	1-5	4-6	Soft	Damp	37
K2 (308/83)	6-20	<1	1-5	8-10	Soft	Damp	24
K3 (348/79)	2-6	<1	1-5	14-16	Soft	Damp	35
K4 (179/85)	6-20	<1	>5	12-14	Soft	Damp	65
R1 (026/16)	20-60	>20	<0.1	12-14	None	Damp	62

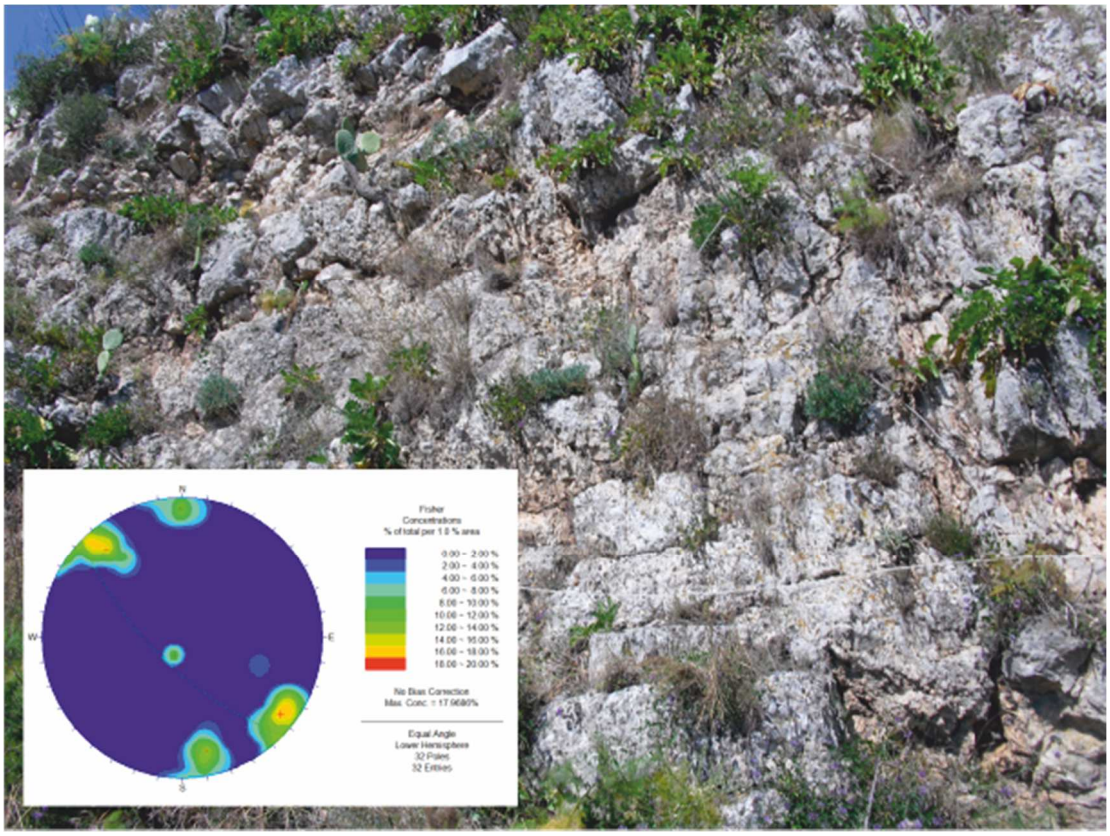

Figure 25: Dol-4 rock mass and contour plot of the surveyed discontinuities.

4.2.5. Lim-1 Station

Surveyed limestones crop out in the northern sector of the study area. Rock masses are heavily fractured and, sometimes, slightly folded (**Figure 26**). In this measurement station discontinuities can be grouped into 7 systems (**Table 10**). Seven sets are characterized by a low persistence and variable spacing, while the remaining three systems, including the bedding family, are more pervasive. The great number of systems surveyed at this rock mass may be due to the influence of a close E-W trending normal fault segment.

Table 10: main features of discontinuities surveyed at Lim-1 station (slope face 070/80).

Discontinuity system	Spacing (cm)	Persistence (m)	Aperture (mm)	JRC	Filling	Hydraulic condition	JCS (MPa)
K1 (323/77)	20-60	<1	1-5	6-8	Hard	Damp	45
K2 (232/50)	20-60	<1	<0.1	8-10	None	Damp	47
K3 (035/54)	6-20	<1	1->5	10-12	Soft	Damp	50
K4 (125/80)	6-20	<1	1-5	8-10	Soft	Damp	52
K5 (103/59)	2-6	<1	<0.1	8-10	None	Damp	43
R1 (300/22)	2-60	>20	>5	8-10	Soft	Damp	48
K6 (140/37)	6-20	1-3	>5	8-10	Hard	Damp	45

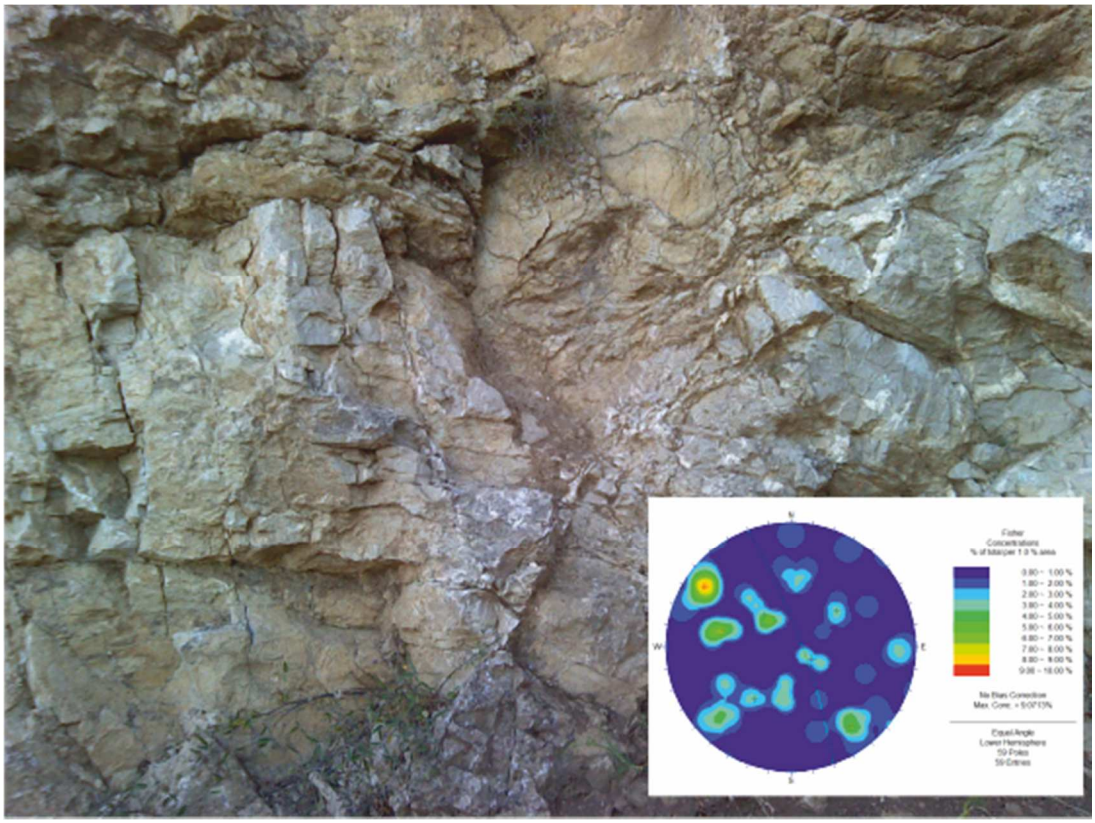

Figure 26: Lim-1 rock mass and contour plot of the surveyed discontinuities.

4.2.6. Lim-2 Station

This station is located along a secondary road, running almost parallel to the upstream segment of MR (**Figure 27**). Although it is only few dozen meters away from Lim-1, a lower number of discontinuity sets was surveyed. In particular, 6 systems, including a bedding set, represent the main geostructural features of this rock mass. Spacing ranges, on average, between 6 and 20 cm and fractures are often open and filled with soft material. Also in this case, discontinuity surfaces are slightly weathered (**Table 11**).

Table 11: main features of discontinuities surveyed at Lim-2 station (slope face 087/72).

Discontinuity system	Spacing (cm)	Persistence (m)	Aperture (mm)	JRC	Filling	Hydraulic condition	JCS (MPa)
K1 (126/53)	6-20	<1	>5	8-10	Soft	Damp	33
K2 (306/80)	6-20	<1	1-5	8-10	Soft	Damp	45
K3 (024/79)	6-20	<1	1-5	6-8	None	Damp	35
K4 (213/72)	6-20	<1	<0.1	10-12	None	Damp	35
K5 (352/84)	6-20	<1	>5	8-10	Soft	Damp	33
R1 (264/19)	6-20	>20	>5	8-10	Soft	Damp	59

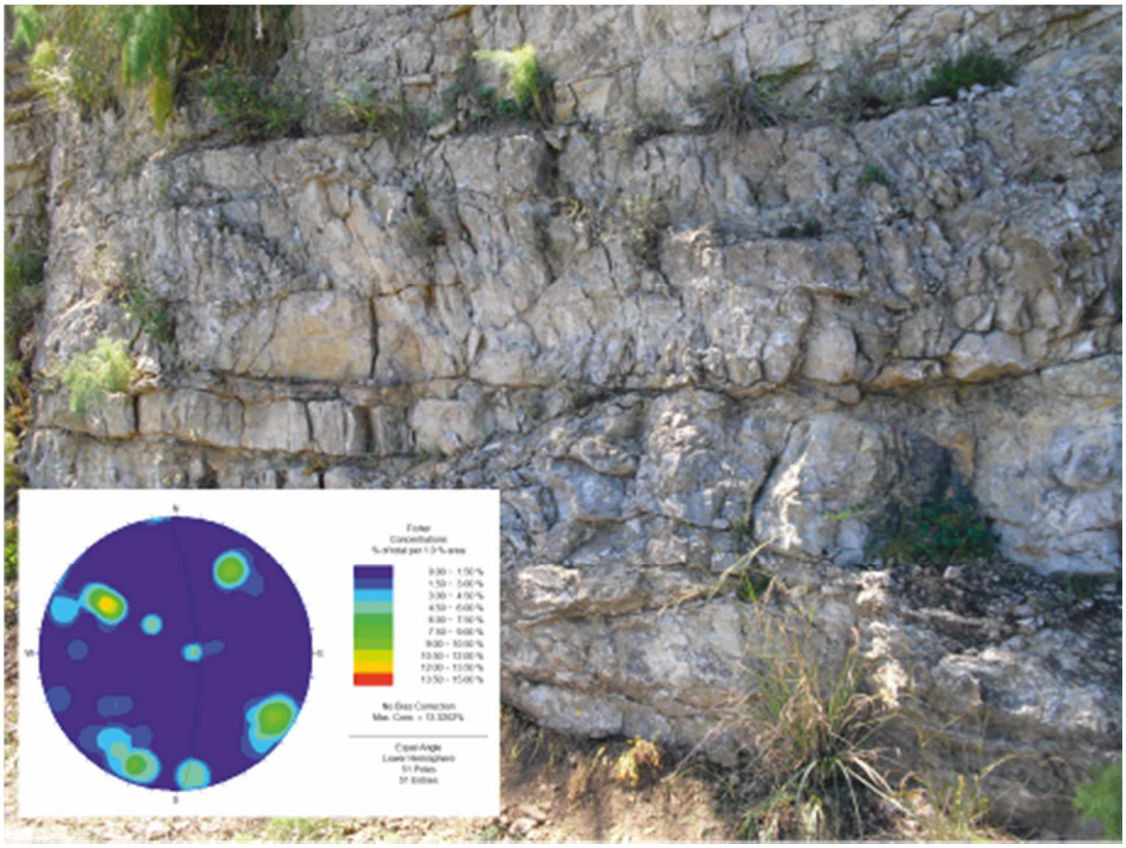

Figure 27: Lim-2 rock mass and contour plot of the surveyed discontinuities.

4.2.7. Por-1 Station

Por-1 rock mass is located along the SP10 road, close to the Castelmola entrance. The rock mass is about 8 m high and shows an intense degree of fracturing and a slight-to-moderate weathering. From the geostructural point of view, 6 discontinuity systems were surveyed with variable spacing and opening. Persistence is generally low, except for a sub-horizontal set (R1), crossing the rock mass with centimetric to metric spacing (**Table 12**). The rosette diagram shows a preferential striking NNW-SSE and N-S, which can be due to a nearby N-S trending normal fault putting in lateral contact the crystalline basement with the sedimentary units (**Figure 28**).

Table 12: main features of discontinuities surveyed at Por-1 station (slope face 340/85).

Discontinuity system	Spacing (cm)	Persistence (m)	Aperture (mm)	JRC	Filling	Hydraulic condition	JCS (MPa)
K1 (253/60)	20-60	<1	>5	4-6	Soft	Damp	69
K2 (180/17)	6-20	<1	1-5	8-10	None	Damp	59
K3 (331/40)	6-20	<1	>5	10-12	None	Damp	69
K4 (056/54)	60-200	<1	1-5	4-6	None	Damp	50
K5 (099/68)	6-20	1-3	>5	4-6	Hard	Damp	39
R1 (282/15)	60-200	>20	>5	0-2	Soft	Damp	50

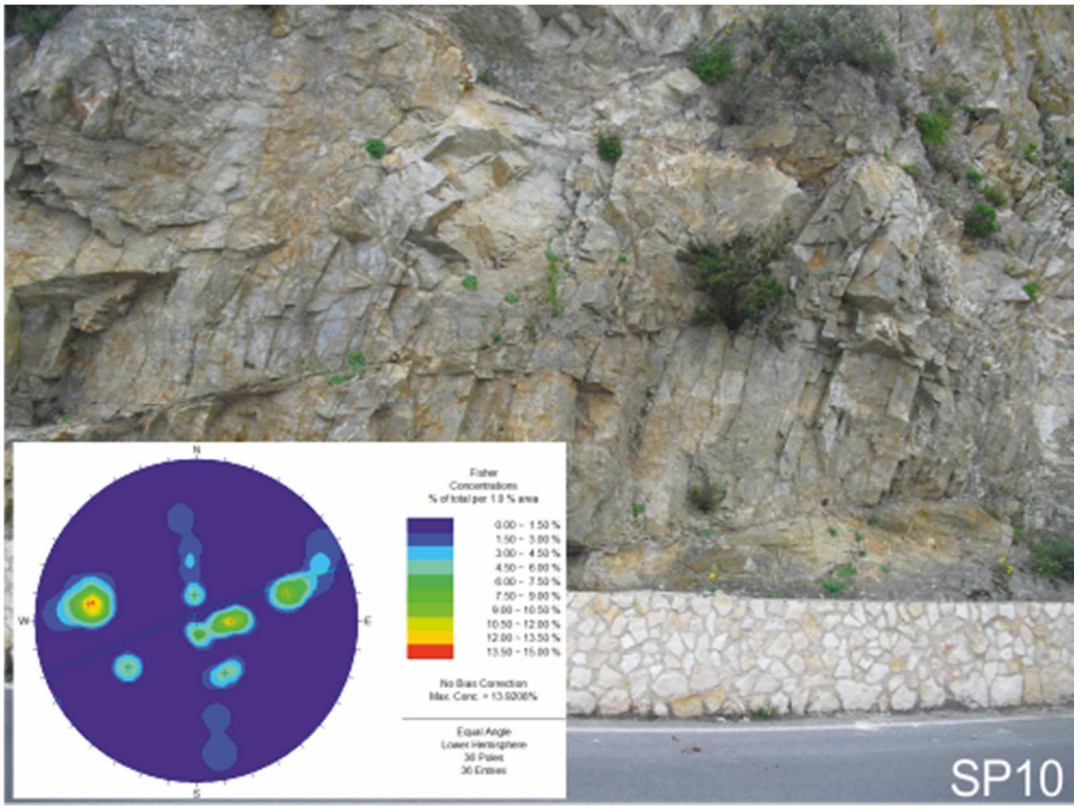

Figure 28: Por-1 rock mass and contour plot of the surveyed discontinuities.

4.2.8. Por-2 Station

This station is placed at the same rock mass previously described, moving towards the village (**Figure 29**). The geostructural setting is very similar to Por-1, with 6 systems characterized by variable spacing and opening (**Table 13**).

Table 13: main features of discontinuities surveyed at Por-2 station (slope face 025/85).

Discontinuity system	Spacing (cm)	Persistence (m)	Aperture (mm)	JRC	Filling	Hydraulic condition	JCS (MPa)
K1 (135/20)	20-60	<1	<0.1	8-10	None	Damp	35
K2 (117/59)	6-20	<1	1-5	4-6	Soft	Damp	48
K3 (173/71)	6-20	3-10	>5	8-10	Soft	Damp	33
K6 (270/40)	6-20	3-10	1-5	8-10	Soft	Damp	35
K4 (070/80)	6-20	1-3	1-5	8-10	Soft	Damp	59
K5 (022/46)	6-20	1-3	<0.1	8-10	None	Damp	43

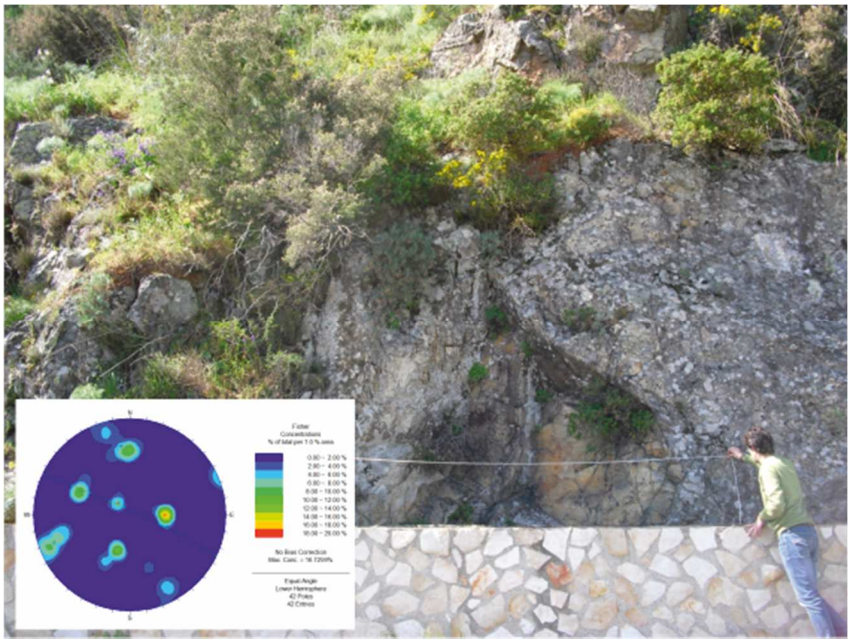

Figure 29: Por-2 rock mass and contour plot of the surveyed discontinuities.

4.2.9. Por-3 Station

Por-3 intensely jointed rock mass is placed along a secondary street linking MR to the pedestrian track at CA. Six fracture systems cross the rock slope(**Figure 30**), which appear intensely jointed and slightly weathered. Fractures are often open and filled with soft material (**Table 14**).

Table 14: main features of discontinuities surveyed at Por-3 station (slope face 022/78).

Discontinuity system	Spacing (cm)	Persistence (m)	Aperture (mm)	JRC	Filling	Hydraulic condition	JCS (MPa)
K1 (081/51)	6-20	<1-3	1-5	6-8	Soft	Damp	56
K2 (327/71)	6-20	<1	1-5	6-8	None	Damp	48
K3 (240/48)	6-20	<1	1-5	10-12	Soft	Damp	33
K4 (359/64)	20-60	<1	<0.1	6-8	None	Damp	45
K5 (158/67)	2-6	<1	1-5	4-6	Soft	Damp	25
K6 (271/76)	2-6	<1	1-5	4-6	Soft	Damp	33

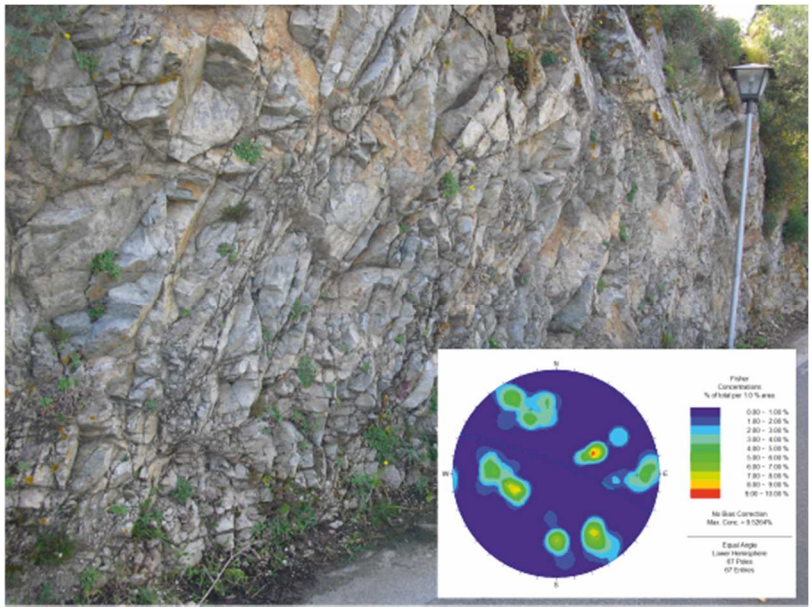

Figure 30: Por-3 rock mass and contour plot of the surveyed discontinuities.

4.2.10. Por-4 Station

This station is located along the SP10 road at CA, close to the end point of several boulders fallen from the cliff. Seven main discontinuity systems, with smooth and slightly weathered surfaces, were surveyed (**Figure 31**). When fractures are open, they hold soft and weathered filling material (**Table 15**).

Table 15: main features of discontinuities surveyed at Por-4 station (slope face 098/62).

Discontinuity system	Spacing (cm)	Persistence (m)	Aperture (mm)	JRC	Filling	Hydraulic condition	JCS (MPa)
K1 (056/68)	2-6	<1	<0.1	4-6	None	Damp	80
K2 (254/63)	6-20	<1	<0.1	10-12	None	Damp	37
K3 (214/50)	6-20	<1	1-5	6-8	Soft	Damp	37
K4 (086/34)	6-20	<1	<0.1	6-8	None	Damp	72
K5 (304/48)	2-6	1-3	<0.1	6-8	None	Damp	41
K6 (336/69)	6-20	1-3	1-5	2-4	Soft	Damp	59
K7 (151/39)	6-20	3-10	1-5	2-4	Soft	Damp	59

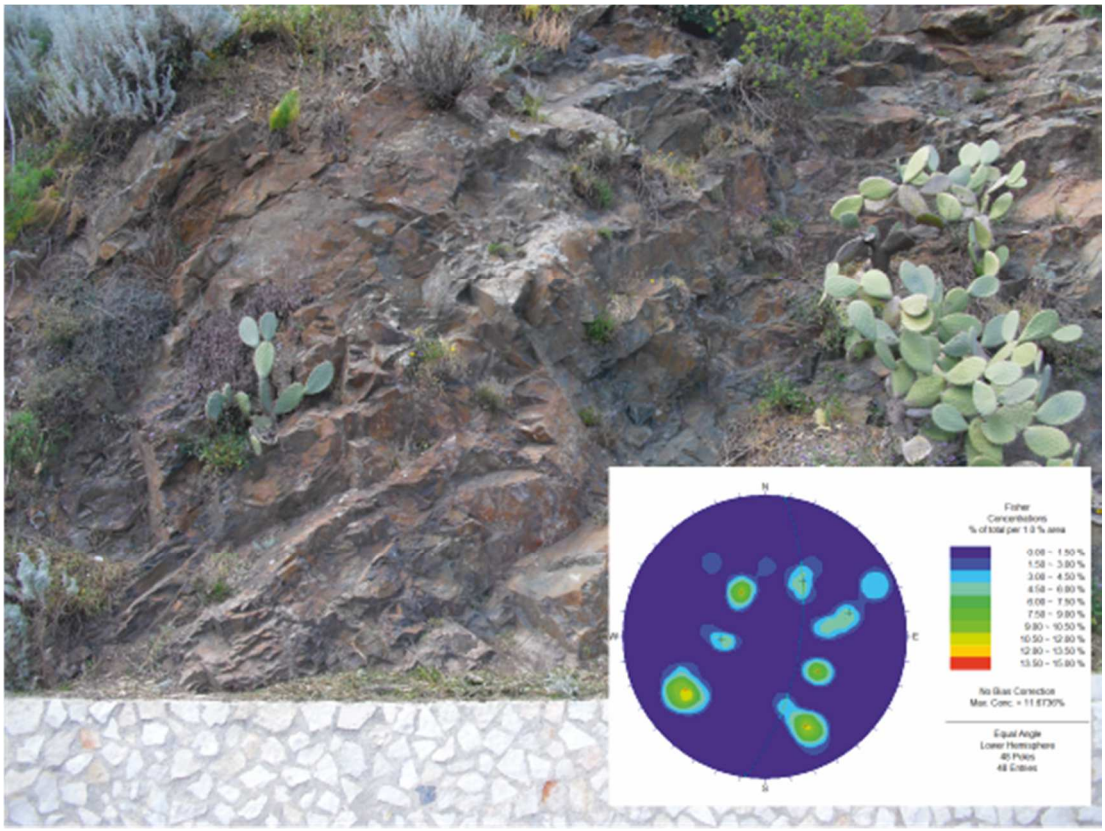

Figure 31: Por-4 rock mass and contour plot of the surveyed discontinuities.

4.2.11. Med-1 Station

The rock mass taken into account herein is located behind the cemetery of Castelmola and it is the most representative outcrop of Medolo formation in this sector (**Figure 32**). Five main systems were surveyed, with spacing ranging between 2 and 60 cm (**Table 16**). In particular, the lowest value is shown by the bedding surface, which is closely spaced and gives the rock mass the aspect of a pile of paper sheets.

Table 16: main features of discontinuities surveyed at Med-1 station (slope face 180/80).

Discontinuity system	Spacing (cm)	Persistence (m)	Aperture (mm)	JRC	Filling	Hydraulic condition	JCS (MPa)
K1 (135/73)	6-20	<1	1-5	6-8	Soft	Damp	23
K3 (214/87)	2-6	<1	<0.1	6-8	None	Damp	25
K4 (083/62)	6-20	<1	1-5	8-10	Soft	Damp	29
K5 (347/85)	20-60	<1	0.1-1	12-14	Hard	Damp	29
R1 (266/25)	2-20	>20	1->5	12-14	Soft	Damp	33

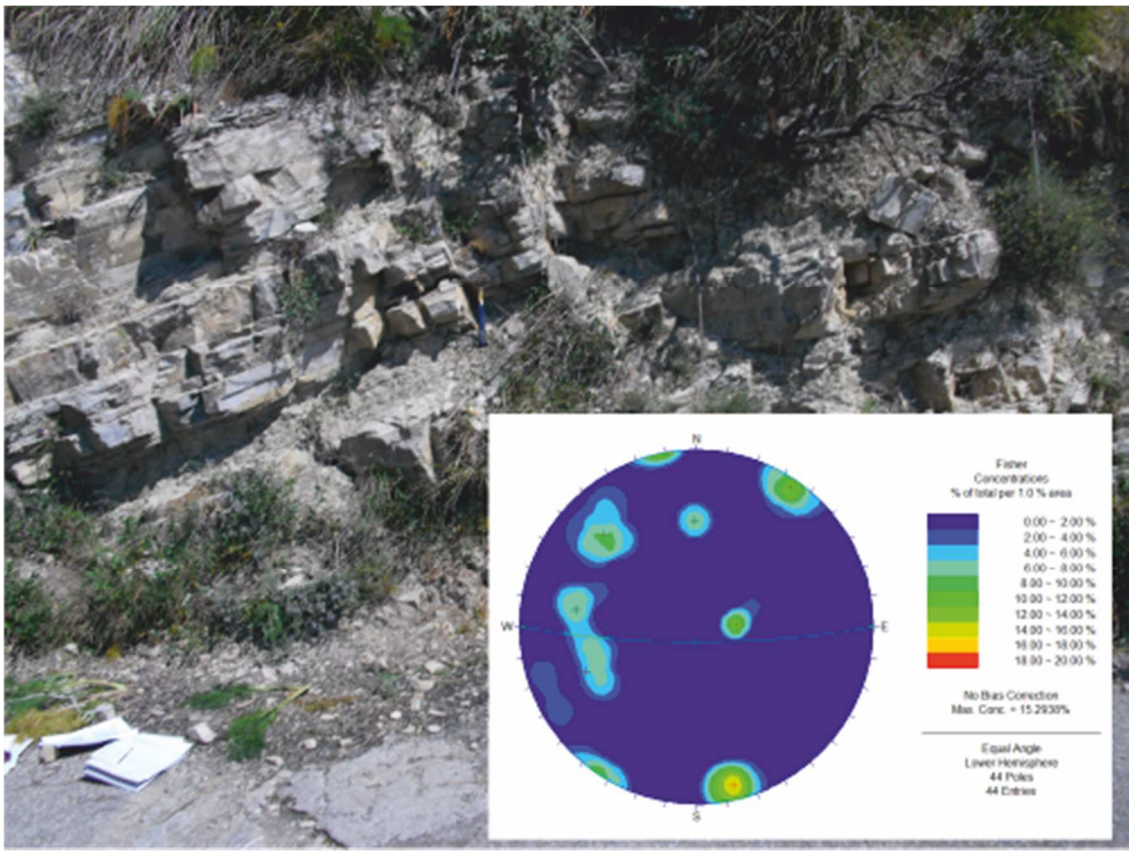

Figure 32: Med-1 rock mass and contour plot of the surveyed discontinuities.

4.2.12. Med-2 Station

This measurement station is the northernmost outcrop surveyed for this study. It is located along the secondary street running parallel to the SP10 road, immediately after the fault segment putting in lateral contact Medolo and Limestones. Five main discontinuity sets were surveyed (**Table 17**). The rock mass looks similar to Med-1, especially due to the presence of a closely spaced bedding system (**Figure 33**). There is a prevalence of E-W trending fractures, according to the direction of the fault segment above mentioned.

Table 17: main features of discontinuities surveyed at Med-2 station (slope face 140/70).

Discontinuity system	Spacing (cm)	Persistence (m)	Aperture (mm)	JRC	Filling	Hydraulic condition	JCS (MPa)
K1 (064/56)	6-20	<1	1-5	8-10	Hard	Damp	41
K2 (167/82)	6-20	<1	0.1-1	8-10	Hard	Damp	29
K3 (001/72)	6-20	<1	0.1-1	8-10	Hard	Damp	21
K4 (130/58)	6-20	<1	<0.1	6-8	None	Damp	28
R1 (261/41)	2-20	>20	>5	6-8	Soft	Damp	25

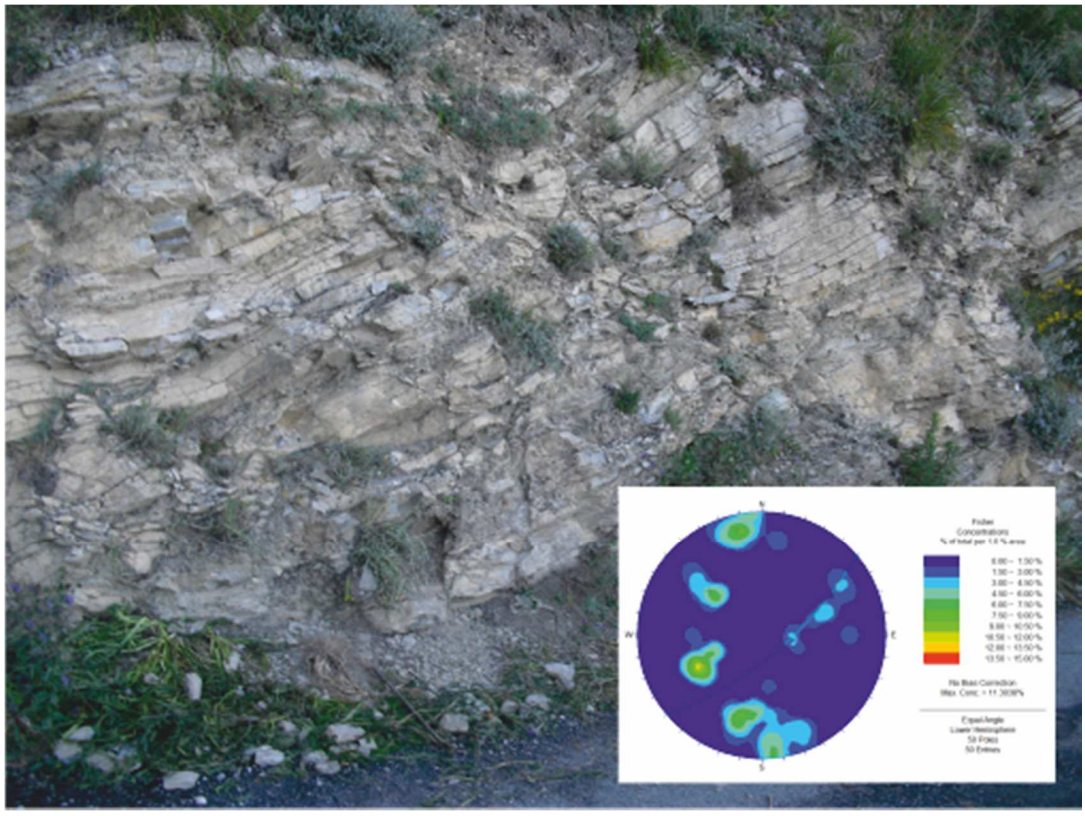

Figure 33: Med-2 rock mass and contour plot of the surveyed discontinuities.

4.2.13. Med-3 Station

As for Dol-4, this rock mass is located in the southern sector of the study area, at the top of the monocline on which Castelmola lies. Surveyed discontinuities can be grouped into five main sets including four joint clusters and a bedding system (**Table 18**). Moreover, the rock mass is crossed by an intraformational fault (herein referred to as R2) showing a ~30-50 cm throw (**Figure 34**). It looks like a compressive structure, probably relatable to the thrust cropping out northwards and putting in tectonic contact limestones on Medolo.

Table 18: main features of discontinuities surveyed at Med-3 station (slope face 133/75).

Discontinuity system	Spacing (cm)	Persistence (m)	Aperture (mm)	JRC	Filling	Hydraulic condition	JCS (MPa)
K1 (072/75)	20-60	<1	>5	14-16	Soft	Damp	28
K2 (190/70)	6-20	<1	1-5	14-16	Soft	Damp	32
K3 (279/80)	20-60	<1	1-5	8-10	Hard	Damp	20
R1 (333/13)	6-20	>20	>5	16-18	Soft	Damp	32
R2 (049/35)	60-200	>20	>5	4-6	Hard	Damp	21

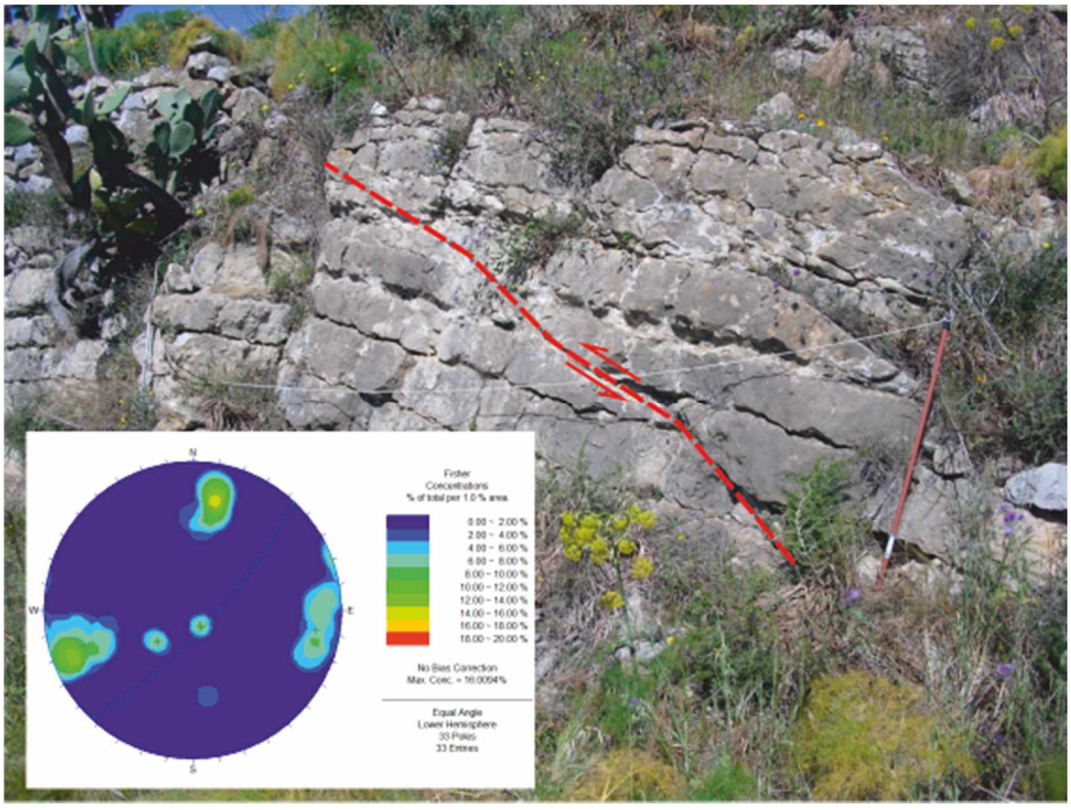

Figure 34: Med-3 rock mass and contour plot of the surveyed discontinuities.

4.2.14. Med-4 Station

This station is placed at a higher elevation with respect to Med-3, between the thrust above mentioned and a E-W trending normal fault. Although the accessibility was not easy and widespread vegetation occurs along the slope, six main systems were surveyed (**Figure 35**). Exposed surfaces are slightly weathered and dry. The less persistent sets show very low apertures and no filling, while the most pervasive discontinuities are often filled with hard material (**Table 19**).

Table 19: main features of discontinuities surveyed at Med-4 station (slope face 245/60).

Discontinuity system	Spacing (cm)	Persistence (m)	Aperture (mm)	JRC	Filling	Hydraulic condition	JCS (MPa)
K1 (175/80)	6-20	<1	<0.1	10-12	None	Damp	36
K2 (018/54)	6-20	<1	<0.1	6-8	None	Damp	26
K3 (236/71)	6-20	<1	<0.1	8-10	None	Damp	32
R1 (301/31)	2-60	>20	1-5	8-10	Soft	Damp	22
K4 (132/82)	6-20	1-3	>5	8-10	Hard	Damp	25
K5 (084/69)	6-20	1-3	1-5	6-8	Hard	Damp	28

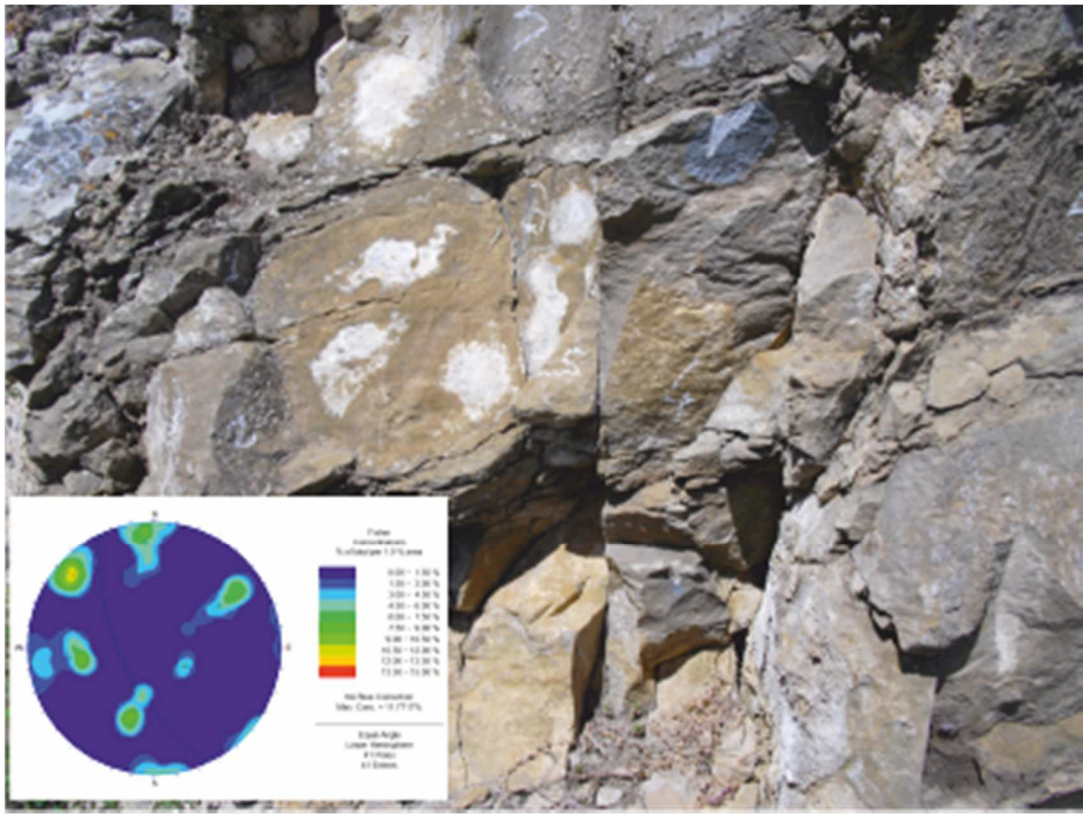

Figure 35: Med-4 rock mass and contour plot of the surveyed discontinuities.

4.3. Statistical presentation of results

After having analyzed field data for each surveyed rock mass, a statistical grouping of the most relevant geomechanical parameters has been performed, in order to highlight differences and similarities between the lithologies taken into account. Data are presented below through doughnut charts, which allow displaying statistics in rings representing data series. Each ring is 100% of the considered parameter and it is divided into labels related to a fixed range of values.

Figure 36 shows that, in general, a very close to close spacing affects most of the surveyed rock masses. In particular, dolostones are characterized by the closest spacing values, probably due to the brittle behavior offered by such rock type (Pappalardo, 2015). At Limestones, Porphyroids and Medolo formation a close-to-moderate spacing prevails. Furthermore, dolostone

outcrops are affected also by 20% of *very wide* spacing, while for the other rock types the percentage is lower, although they show also *very wide* features.

With reference to the persistence parameter, all the lithologies are affected by a prevalence of low persistent discontinuities, because of the high degree of fracturing subdividing the rock masses into small rock volumes. On the other hand, Limestones and Medolo formation have the highest percentage of *very high persistence*, because of the bedding surfaces, widely affecting such rock types.

Most of the discontinuities are open and filled with soft material, which is likely to come from the weathering processes affecting the rocks (**Figure 37**). Only a low percentage of fractures is closed or very tight, regardless of the lithology. Moreover, half of the discontinuities surveyed at dolostone and porphyroid rock masses do not show any filling, while a relevant percentage of fractures in all the sedimentary rock masses is filled with hard material, usually calcite, due to chemical dissolution processes. This is a relevant consideration, because empty fractures are preferential way of drainage for water, which, at the same time, enhances chemical processes of interaction between rock and water itself, thus leading to dissolution and weathering phenomena.

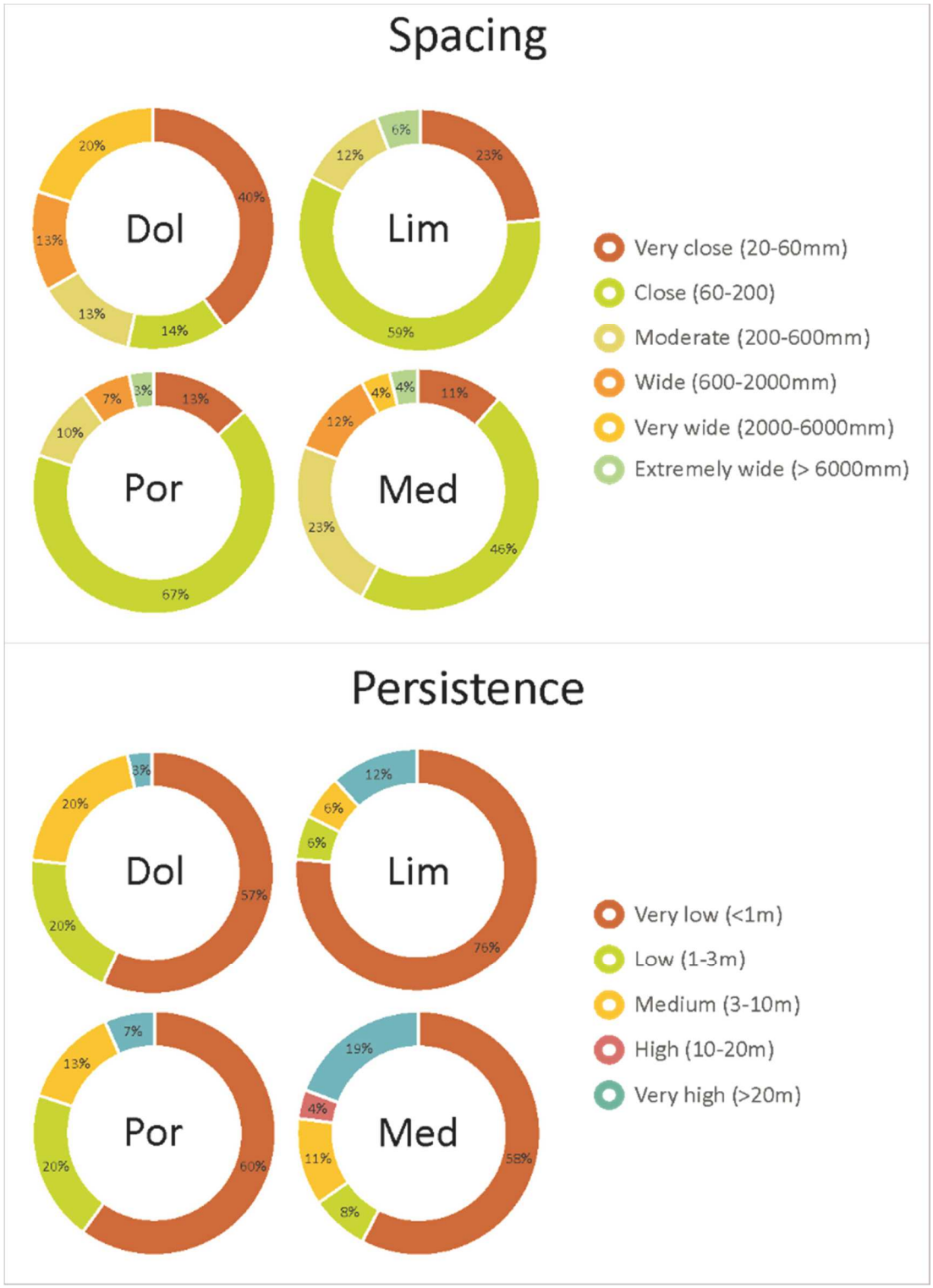

Figure 36: doughnut charts showing the statistical percentages of spacing and persistence values for each surveyed lithology.

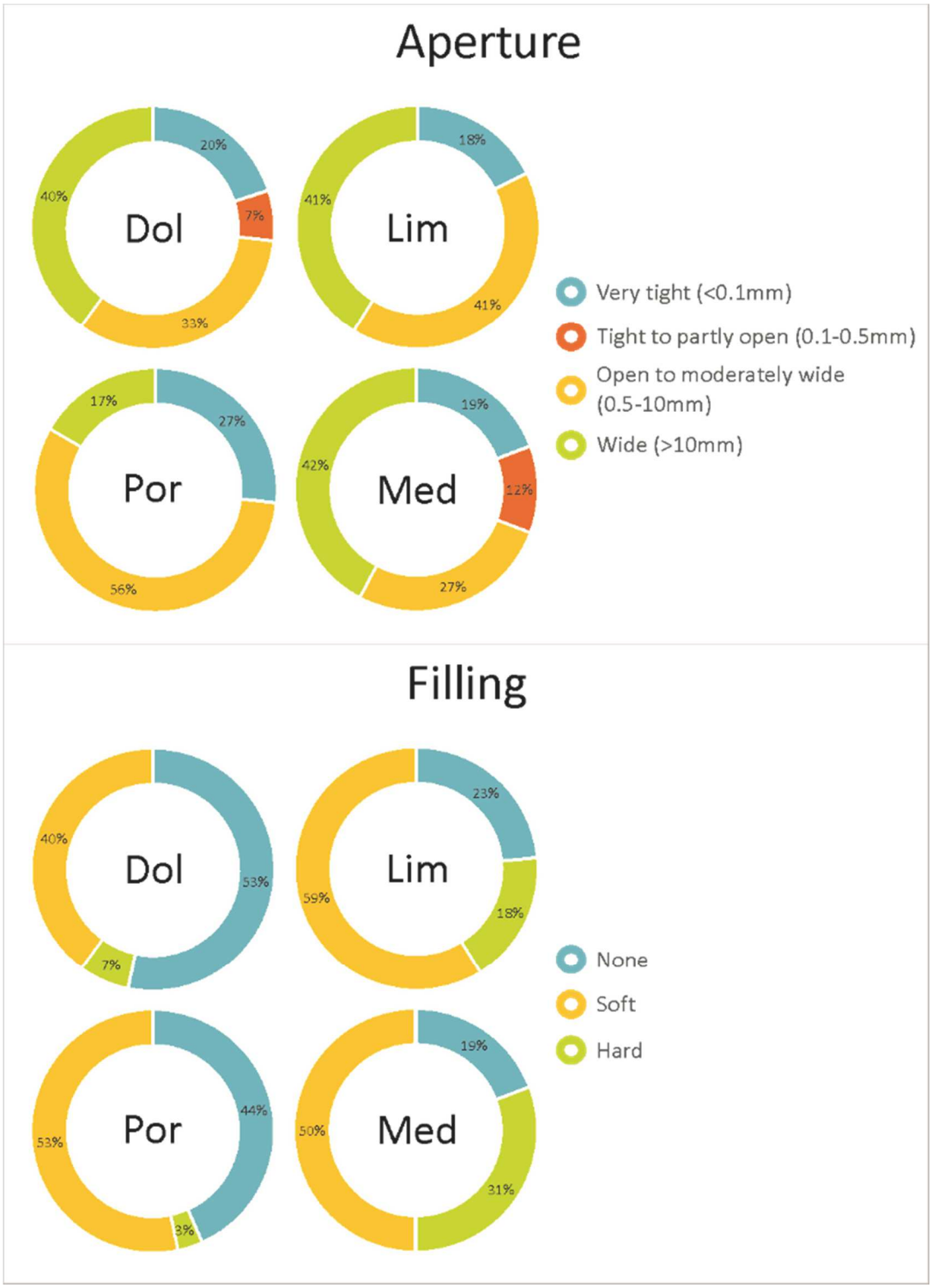

Figure 37: doughnut charts showing the statistical percentages of aperture and filling values for each surveyed lithology.

CHAPTER 5

FAILURE PATTERNS AND KINEMATIC ANALYSIS

5.1. Failure patterns of rock slopes

Hard rock is usually so strong that failure under gravity alone is possible only if discontinuities permit easy movement of discrete blocks (Goodman, 1989). In jointed rock slopes the orientation of discontinuities gives rise to the exhibition of a large variety of failure modes along weakness features. The identification of such patterns is not always an easy practice in the field, especially in complex contests where several types of geological structures may be present. Nevertheless, failure modes can be outlined by examining pole plots after a rock mass survey, based on the orientation of discontinuities and the slope face. There are four basic patterns that can be identified by the stereonet analysis (**Figure 38**), even if in actual jointed rock slopes, a series of combination between such patterns can also take place (Goodman and Bray, 1976):

- Planar failure (**Figure 38**a), occurring at slopes containing persistent joints dipping out of the slope face and, at the same time, striking parallel to the face. In this case, a rock block can rest on an inclined weakness plane that "daylights" into free space. The movement of such block can occur along both the surface of sliding and the lateral margins of the slide as well.
- Wedge failure (**Figure 38**b), affecting a block enclosed between two intersecting discontinuities. Slip can occur without any topographic or structural release feature, if the line of intersection of the two discontinuities "daylights" into free space. A wedge can slide either along the line of intersection of the two discontinuities or along one of the two planes characterized by a more favorable direction for sliding than the line of intersection.

- Toppling failure (**Figure 38**c), occurring at strong rock containing discontinuities dipping steeply into the face, thus giving rise to inclined rock layers. In this case, each layer tends to bend downhill under its own weight. If the toe of the slope is allowed to slide or overturn, flexural cracks will form in the layers above, liberating a large mass of rock.
- Circular failure (**Figure 38**d), affecting very weak or closely fractured rock masses with randomly oriented discontinuities. Such rocks behave as a "pseudocontinuous" matter, because they show so many combination of failure modes that there is always a locus along preexisting cracks corresponding to the most critical failure locus of a continuous material. Slopes in such rocks can be analyzed using soil mechanics approaches (Hoek and Bray, 1977).

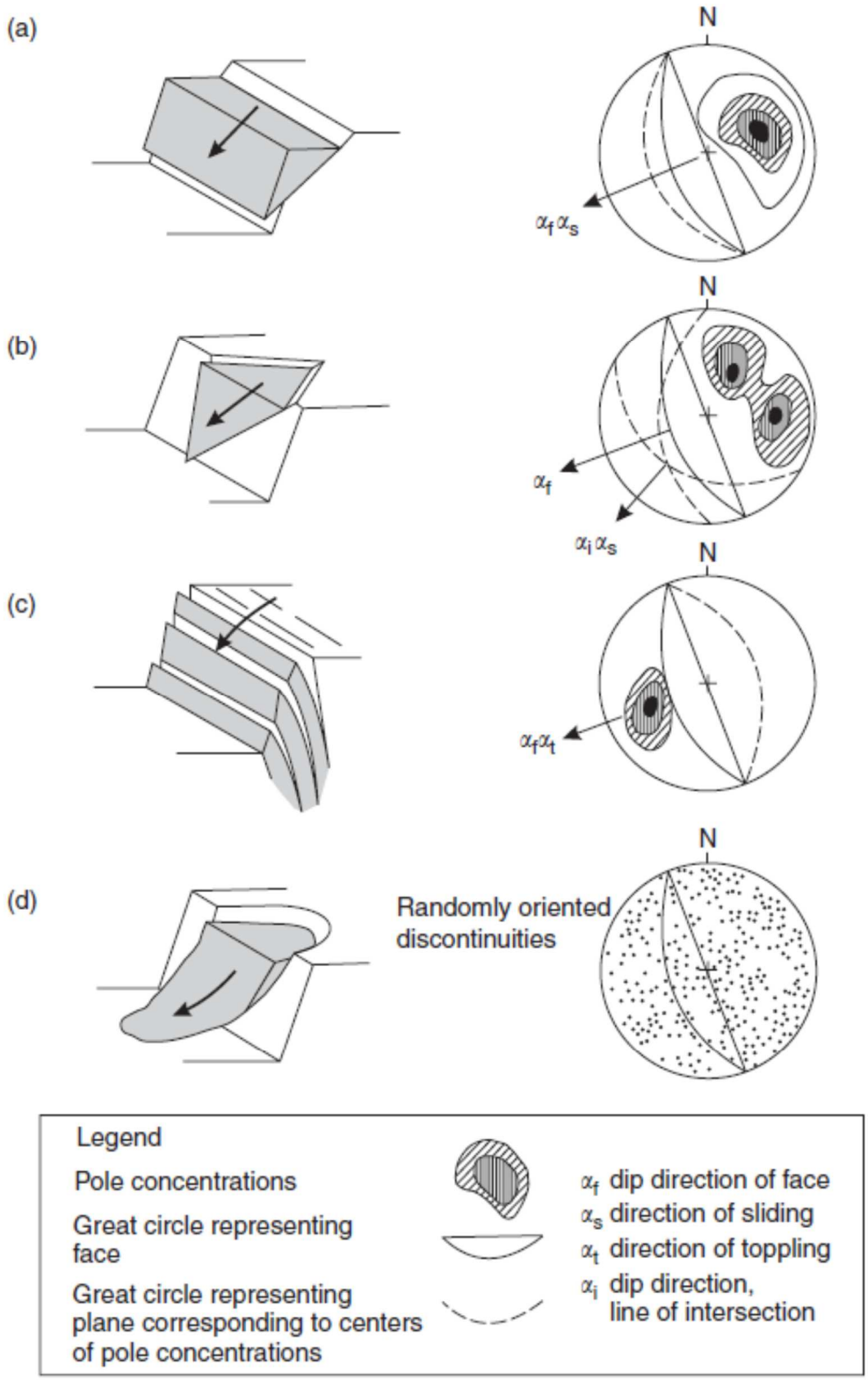

Figure 38: main failure patterns (after Wyllie and Mah, 2004): a) plane failure, b) wedge failure, c) toppling failure, d) circular failure.

5.2. Kinematic analysis

The term "kinematics" refers to the motion of a body with no reference to the forces driving it (Goodman, 1989). In real cases, several rock cuts are stable on steep slopes even though they are affected by steeply inclined planes of weakness with low strength; this happens when there is no freedom for a block to move along the weak surface because other ledges of intact rock are in the way, working as mechanical blockage. Should such blockage be removed by any natural or artificial cause, the slope would fail immediately.

Therefore, to carry out a kinematic analysis it is essential to consider also the shear strength along the sliding surface and it must be assumed that the shear strength comprises only friction and that the cohesion is zero.

For this reason, kinematic analysis is a preliminary procedure aimed at giving an indication of the stability of a rock mass through the analysis of stereonets (e.g. Markland, 1972; Hocking, 1976; Matheson, 1983). Nevertheless, while such analysis provides a good indication of stability conditions, it does not consider external forces such as water pressures or reinforcement features, which can have a significant effect on stability. Therefore, the usual design procedure is to use kinematic analysis to identify potentially unstable mechanisms, followed by detailed stability analysis of peculiar blocks.

5.2.1. Planar failure

This type of failure is possible according to three conditions:

1) the potential failure plane "daylights" on the slope face, i.e. it dips at a flatter angle than the face ($\psi a < \psi f$);
2) the dip direction of the discontinuity does not differ from the dip direction of the face by more than about 20° ($|\alpha a - \alpha f| < 20°$);
3) the angle of the discontinuity plane is greater than the friction angle of the sliding surface ($\psi a > \varphi$).

According to this, it is essential to plot on a stereonet the great circle of the slope face and the poles of the surveyed discontinuities, along with the daylight envelope, lateral limits and friction cone. In particular, the daylight envelope is the area within which all poles of the planes that daylight fall; the lateral limits are fixed to delimit the ±20° margin of difference between the direction of the face and the potentially unstable discontinuities; the friction cone encloses the area within which all poles belonging to planes dipping at angles lower than φ fall (**Figure 39**). All the poles enclosed within these three features are unstable from the kinematics point of view.

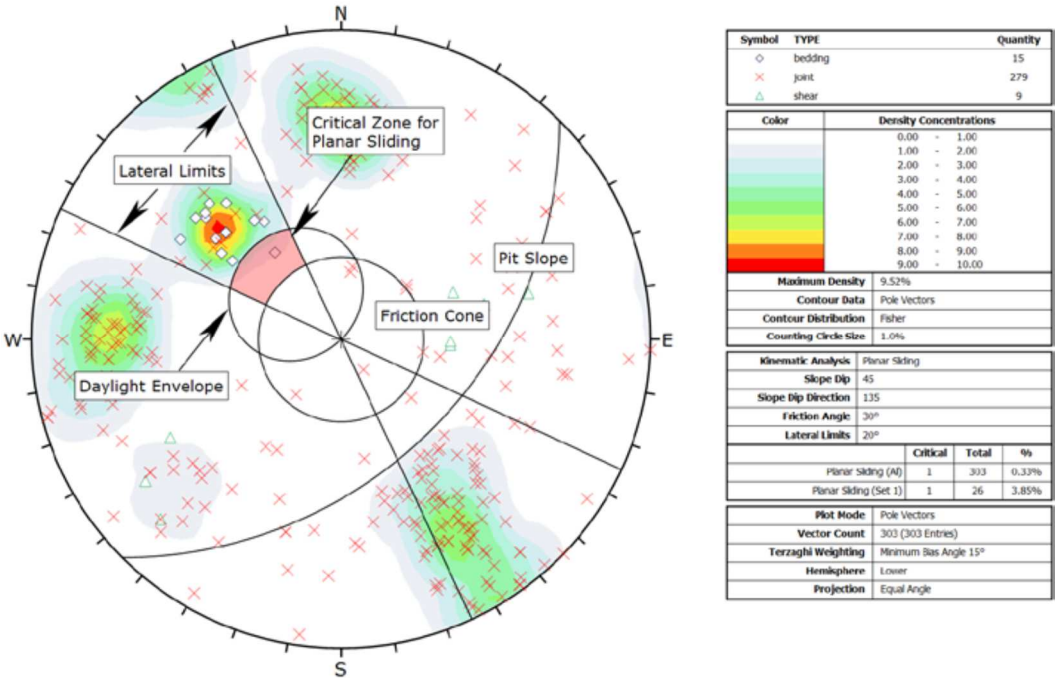

Figure 39: representative stereonet showing the relevant elements for the kinematic analysis of planar failure (Rocscience Dips 6.0 manual).

5.2.2. Toppling failure

For a toppling failure to occur, the conditions are listed as follows:

1) the potentially unstable discontinuity has to show an opposite dip with respect to the slope face;
2) the dip direction of the discontinuity dipping into the face must be within about 30° of the dip direction of the face ($|\alpha a - \alpha f| < 30°$);

3) the direction of the applied compression has to make an angle greater than φ with the normal to the discontinuity.

In this case, the envelope defining the orientation of the potentially unstable planes lies at the opposite side of the stereonet from the sliding envelopes and there will be a further feature to plot called "slip limit", which is a plane defining the critical zone for toppling (**Figure 40**). All poles falling within the critical zone are unstable from the kinematics point of view.

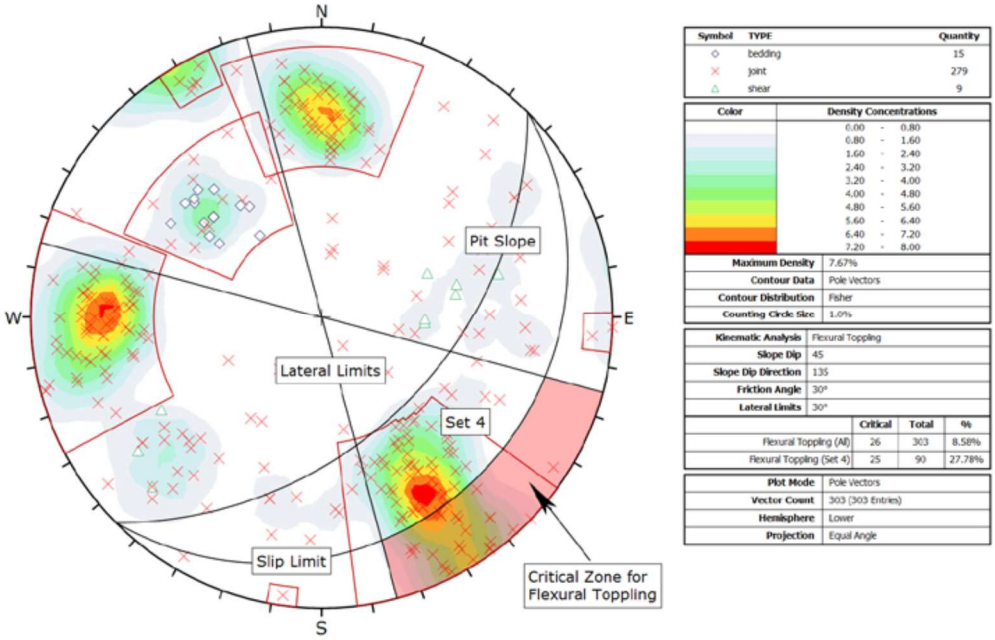

Figure 40: representative stereonet showing the relevant elements for the kinematic analysis of toppling failure (Rocscience Dips 6.0 manual).

5.2.3. Wedge failure

The kinematic analysis for wedge failure can be carried out in a similar manner to that of plane failures. In this case, the pole of the line of intersection of the two discontinuities is plotted on the stereonet and sliding is possible if the pole daylights on the face ($\psi i < \psi f$). The direction of sliding of kinematically permissible wedges is less restrictive if compared to that of planar failures, because there are two planes acting as release surfaces. Therefore, the daylight envelope for the line of intersection is wider than the envelope for

plane failures and encloses all poles representing lines of intersection whose dip directions lie in the plane of the slope face (**Figure 41**).

On the other hand, instead of plotting poles of the lines of intersection, a more expeditious way to carry out a wedge kinematic analysis is to plot the great circles of the intersecting planes along with the friction cone representing the friction angle along planes. In this case, two critical zones are defined: the primary critical zone is the crescent shaped area inside the plane friction cone and outside the slope plane (red area in **Figure 42**). Intersections falling in this zone represent wedges, which satisfy frictional and kinematic conditions for sliding along the intersection line. The secondary critical zone (yellow area in **Figure 42**) is the area between the slope plane and a plane (great circle) inclined at the friction angle. Critical intersections falling in this zone always represent wedges, which slide on one joint plane. In this region, the intersections are actually characterized by a lower angle than the friction angle, but sliding can take place on a single joint plane, which has a dip vector greater than the friction angle itself.

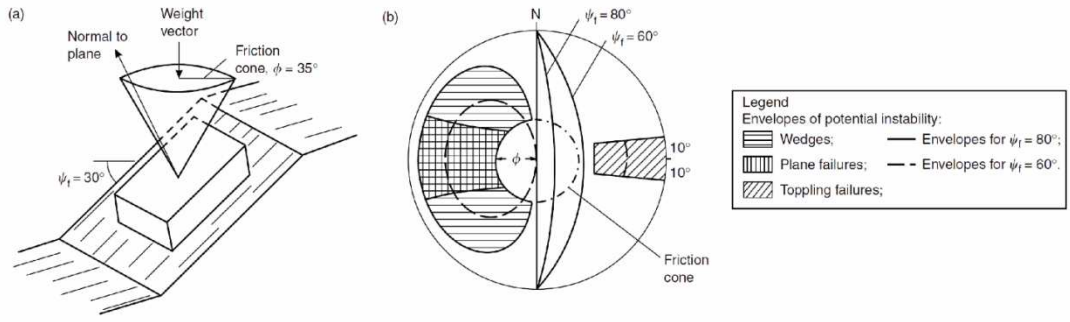

Figure 41: combined kinematics and simple stability analysis using friction cone concept: (a) friction cone in relation to block at rest on an inclined plane (i.e. ϕ > ψf); and (b) stereographic projection of friction cone superimposed on "daylighting" envelopes (modified after Wyllie and Mah, 2001).

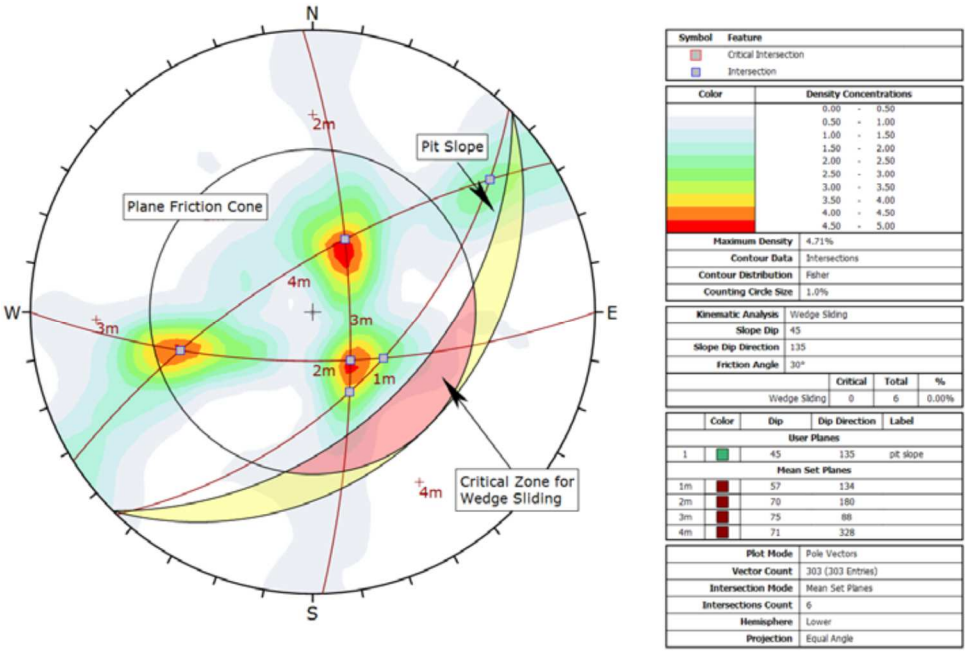

Figure 42: representative stereonet showing the relevant elements for the kinematic analysis of wedge failure (Rocscience Dips 6.0 manual).

5.3. Analysis of surveyed data

The analysis of stereograms was carried out with the aim of achieving a preliminary knowledge on the stability condition of each surveyed rock mass, with particular reference to every discontinuity set. For a simple and neat representation of data, discontinuities have been plotted as poles for the analysis of plane and topple patterns, and as great circles for the kinematic analysis of wedges. Friction angles were assumed according to Barton and Chaubey (1977).

5.3.1. Dolostones

All the surveyed rock masses show a strong predisposition to fail through wedge sliding, followed by planar sliding and rare topples (**Figure 43**). In particular, Dol-1 shows instability conditions for planar failures with respect to a few random discontinuities and some belonging to K3 set. Toppling is likely to involve only some planes of K2 system, while wedge sliding may affect K1, K3 and K4. In this case, wedges are usually formed by the intersection of two discontinuity planes. It has to be underlined that such setting is related to one of the less fractured rock slopes.

On the other hand, Dol-2 station is characterized by critical stability conditions with respect to K2 and K5 sets (planar failure), K3 and K4 (toppling failure). The intense degree of fracturing affecting such slope gives rise to a wide and complex configuration of wedge patterns. In fact, unstable wedges can be formed by the intersection of two or three discontinuity planes. Although such failure patterns will be discussed in detailed in the following sections, it is clear how precarious the stability of this rock mass is.

A similar setting characterizes Dol-3, which is located close to the previous station. Planar sliding would involve K6 and K4 systems, while toppling would slightly affect K2, K3 and K5. Even in this case, the high degree of fracturing leads to the formation of unstable wedges by K1, K4 and K6 sets.

Dol-4, located in a different spot of the study area, seems not to be affected by relevant criticalities from the plane and topple failures points of view, although an isolated pole falls within the instability area for planar sliding. Wedge is the most probable failure pattern, with particular reference to the symmetric intersection between K1 and K2.

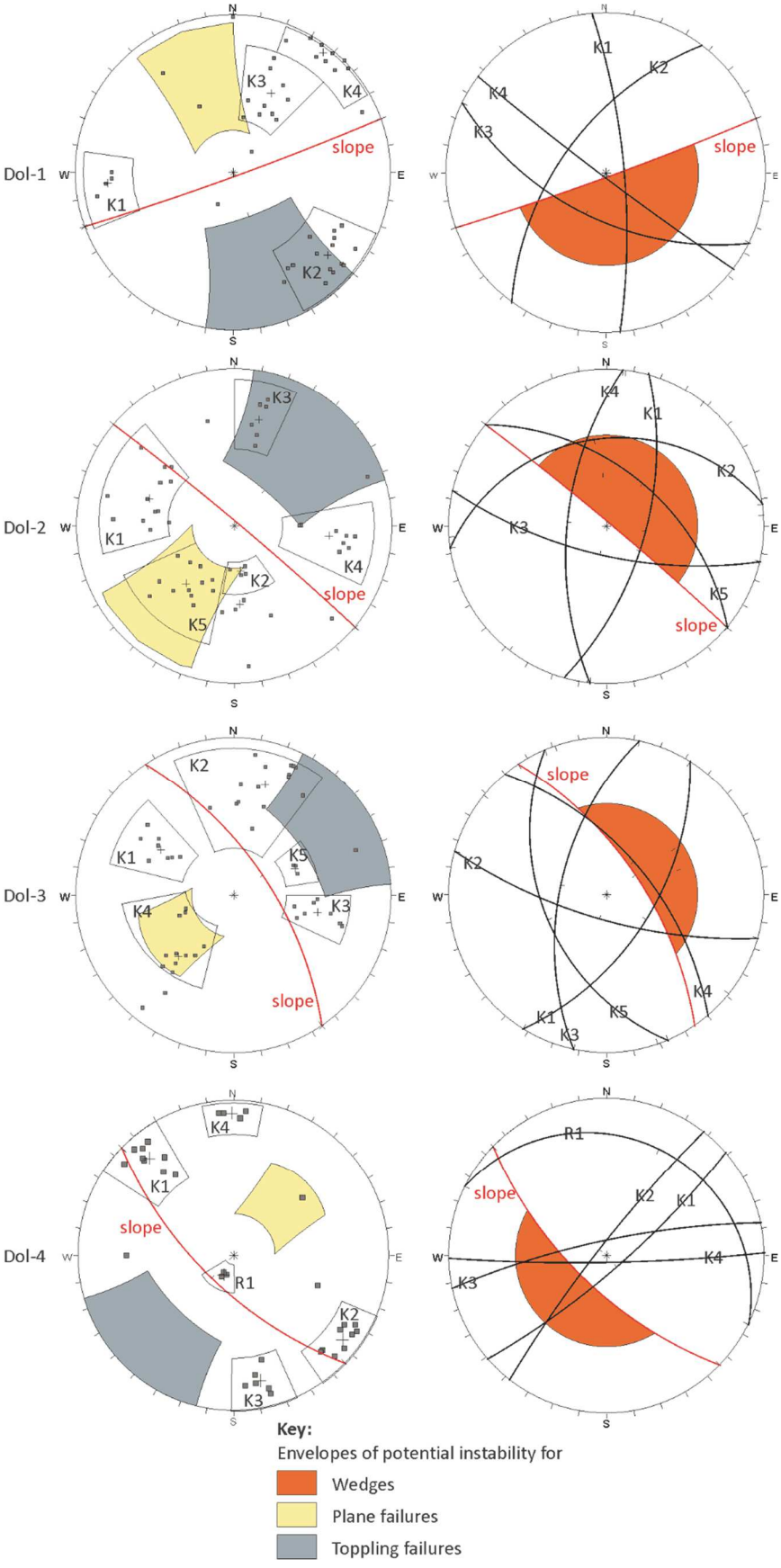

Figure 43: kinematic analysis for Dolostone outcrops.

5.3.2. Limestones

Limestone outcrops are characterized by a complex geostructural setting, which is likely to be the main responsible for the evident instability affecting such slopes. In particular, Lim-1 rock mass is affected by a great number of scattered poles, which were grouped into 7 discontinuity systems. The large number of sets along with the presence of random poles is index of a poor quality slope from the mechanical point of view. Planar sliding is mainly possible along K3 system, while toppling could involve K2 and some random pole. In this perspective, random discontinuities may give rise to local failures, which has to be always taken into account. Wedge sliding is possible between two or three planes belonging to most of the systems (**Figure 44**).

Lim-2 is unstable for planar sliding due to the geometrical attitude of K1 and K6; although such sets falls only partly within the critical area, they must be considered unstable, because of the slightly variable orientation of the slope face. This consideration is valid also for toppling failures with reference to K2 system. Wedge sliding may occur at the intersection of K1, K3, and K6 (**Figure 44**).

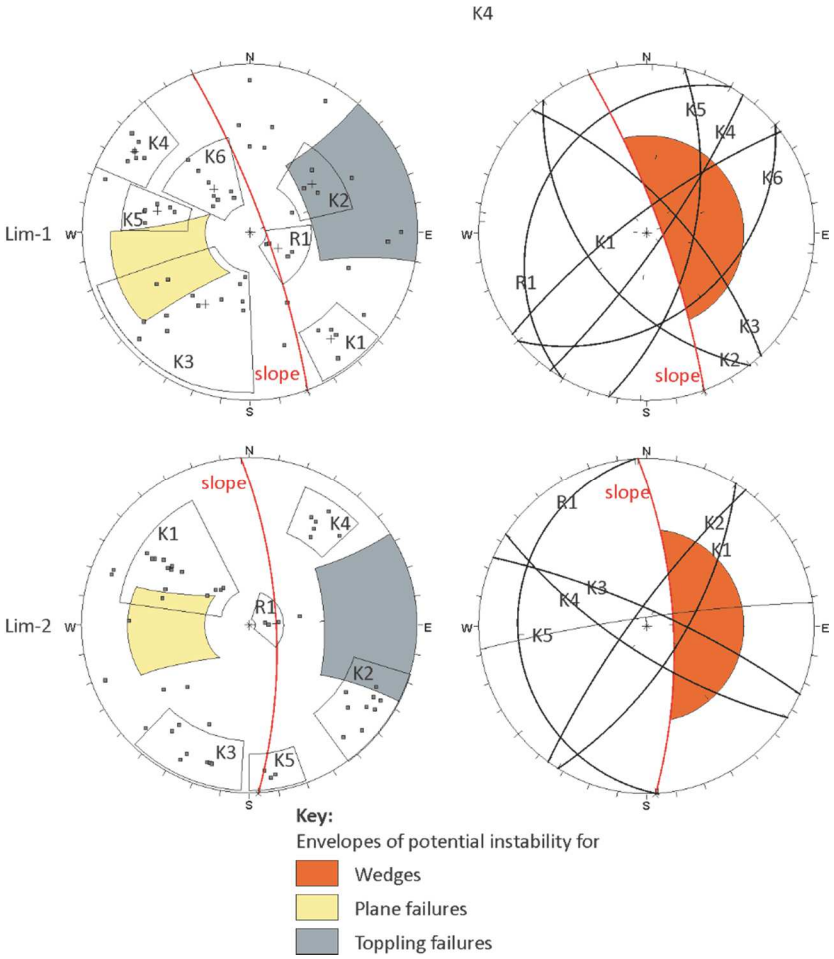

Figure 44: kinematic analysis for Limestone outcrops.

5.3.3. Porphyroids

The geostructural setting of porphyroids leads to a high predisposition of slope failure through wedge sliding, followed by plane and topple patterns (**Figure 45**). As for the above reported intensely fractured lithologies, when the rock mass is characterized by numerous discontinuity systems, there is a high probability of intersection between them, resulting in potentially unstable wedge configurations.

In particular, the K3 set at Por-1 strikes almost parallel to the slope face, leading to a critical plane sliding predisposition. Moreover, the intersection between such plane and K1-K3 sets gives rise to the most critical unstable feature of the rock mass, represented by asymmetric wedges. On the other hand, some poles belonging to K2 set fall within the critical area for topples.

A similar setting characterizes Por-2 rock mass, where K3 and K5 can be regarded as potentially unstable sets for toppling and planar sliding respectively, while K2, K4 and K5 form unstable wedge patterns.

Por-3 represents the most complex station of the investigated lithology, characterized by numerous unstable intersections between discontinuity systems, giving rise to wedges formed by two or three intersecting planes. K5 and K1-K4 are regarded as unstable sets for toppling and planar failures respectively, although they do not fall entirely within a critical area.

Por-4 is affected by possible planar sliding along K4 and K7 sets and toppling at K2 and, probably, K5. The intersection between K1, K4, K6 and K7 forms unstable wedges enclosed between two planes.

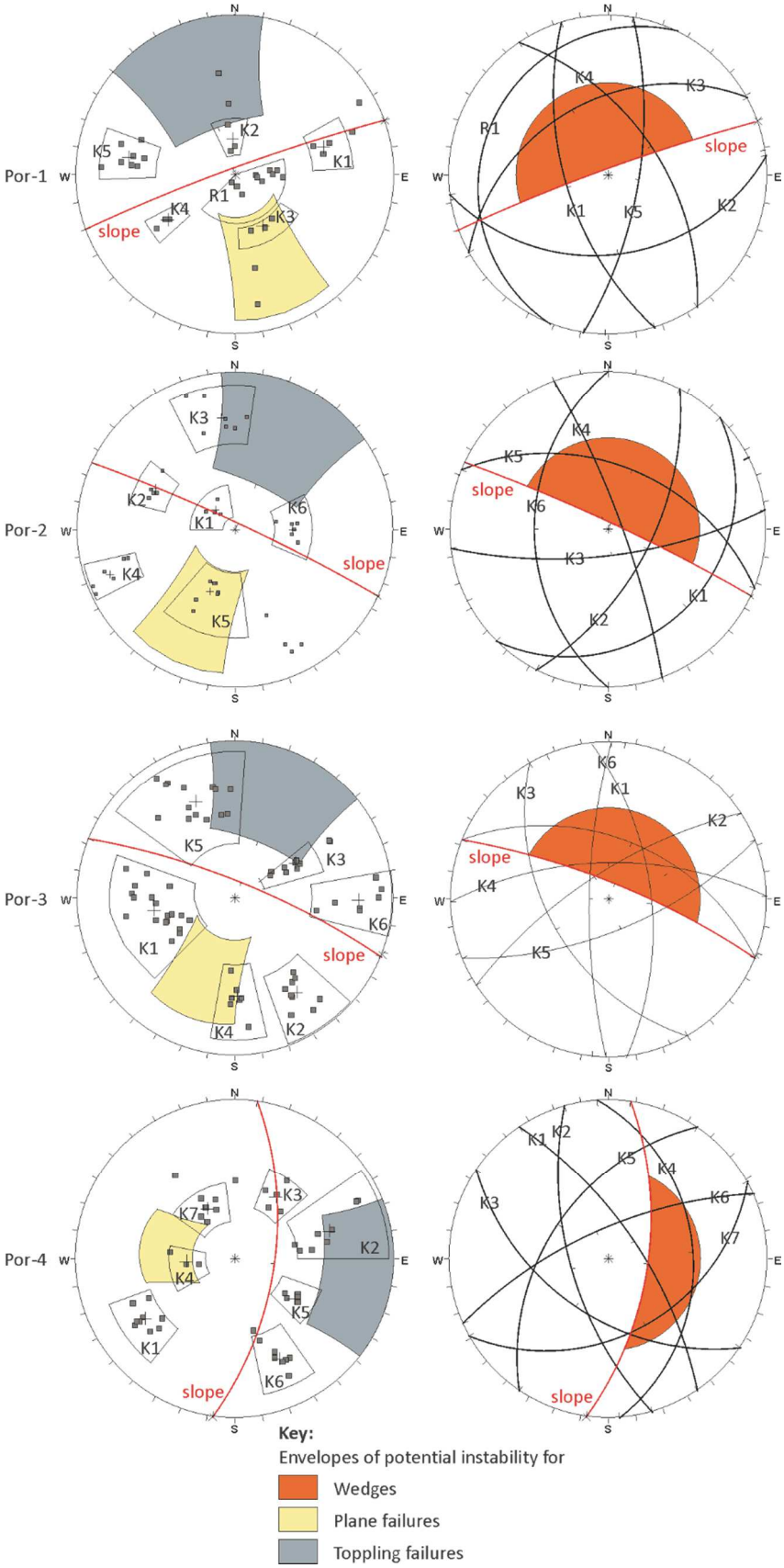

Figure 45: kinematic analysis for Porphyroid outcrops.

5.3.4. Medolo

According to the geostructural setting, also Medolo outcrops are characterized by widespread unstable features, due to the unfavorable orientation of some discontinuity systems. In particular, Med-1 is affected by a system with the same orientation of the slope face, although with a lower dip, representing the most critical condition for planar sliding. This system (R2) intersects K1, K2, K3 and K4 to form unstable wedges whose failure would be probably driven by the dip-slope R2 set, thanks to its orientation. Toppling is possible along K5 set and some random planes.

A similar setting affects Med-2, where the dip-slope system is K4, which is unstable both for planar and wedge sliding. Toppling would affect K3 system, although some poles fall outside the critical area for toppling pattern.

Unlike the other surveyed rock masses, Med-3 lacks of the dip-slope plane and only a few scattered poles fall within or near the critical area for plane sliding. K1 and K2 are the only systems giving rise to a symmetric unstable wedge pattern, while K3 resulted unstable for toppling.

Finally, Med-4 shows instability conditions along K3, R1 (planar sliding) and K5 (toppling) and deserves a specific comment for wedge sliding. In fact, although no intersection lines fall within the critical area, wedge failure patterns should be evaluated case by case, because some great circles intersect at the edge of the instability area (**Figure 46**). This means that slight variations of the friction angle will play a key role for the stability of such feature.

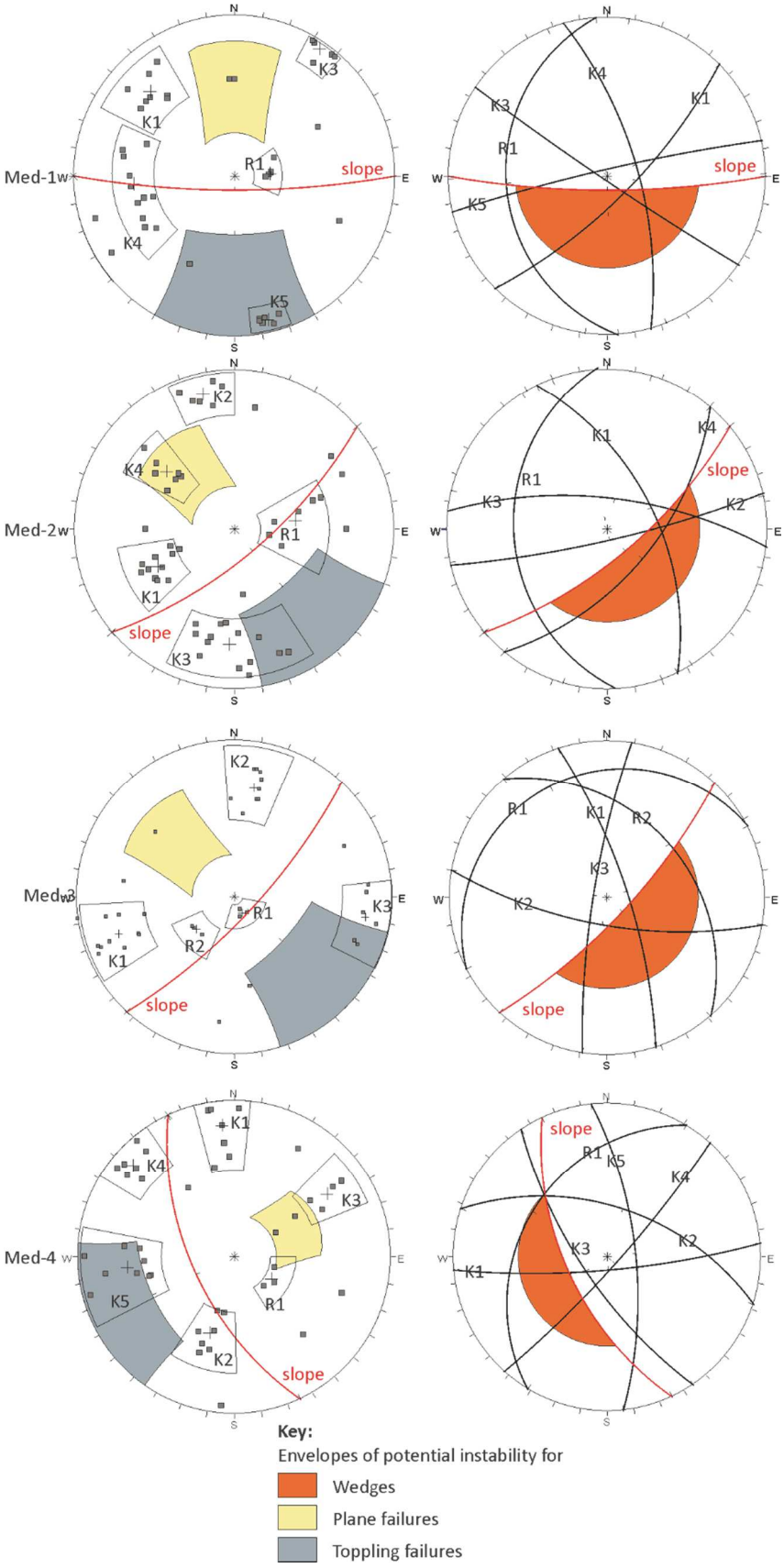

Figure 46: kinematic analysis for Medolo outcrops.

CHAPTER 6

GEOMECHANICAL CLASSIFICATION OF ROCK MASSES

Although sometimes instability problems are confined within specific portions of a slope, the study of a rock mass cannot lack of specific consideration on its geomechanical attitude. International literature provides several approaches, known as *classification systems*, which allow assigning a quality class to the rock mass according to the main parameters measured during the field survey. This section provides a general overview on two scientifically relevant approaches (i.e. the Rock Quality Designation method and the Rock Mass Rating system), which were taken into account herein for the geomechanical classification of the surveyed rock masses.

6.1. The main classification systems

6.1.1. The Rock Quality Designation

The Rock Quality Designation index (RQD) was developed by Deere et al. (1963) to provide a quantitative estimation of rock mass quality from drill core logs. It is defined as the percentage of intact core pieces longer than 100mm in the total length of the core.

Such index is an easy and quick measurement as only core pieces with a certain length are included. It is, therefore, frequently applied in core logging and is often the only method used for measuring the degree of jointing along a core drill hole (**Figure 47**).

It is self-evident that RQD is a directionally dependent parameter and its value may change significantly, depending upon orientation of the borehole or scanline with respect to the discontinuity systems. However, such index has been widely used in the rock mechanics for the past years and it is now one of the required parameters by the most known geomechanical classifications methods for rock masses.

According to the RQD value measured in field, the rock mass quality is defined as reported in **Table 20**. In this light, a high RQD value is index of a low fractured rock succession, characterized by a good mechanical quality, while an intensely fractured rock succession would be affected by very low RQD values.

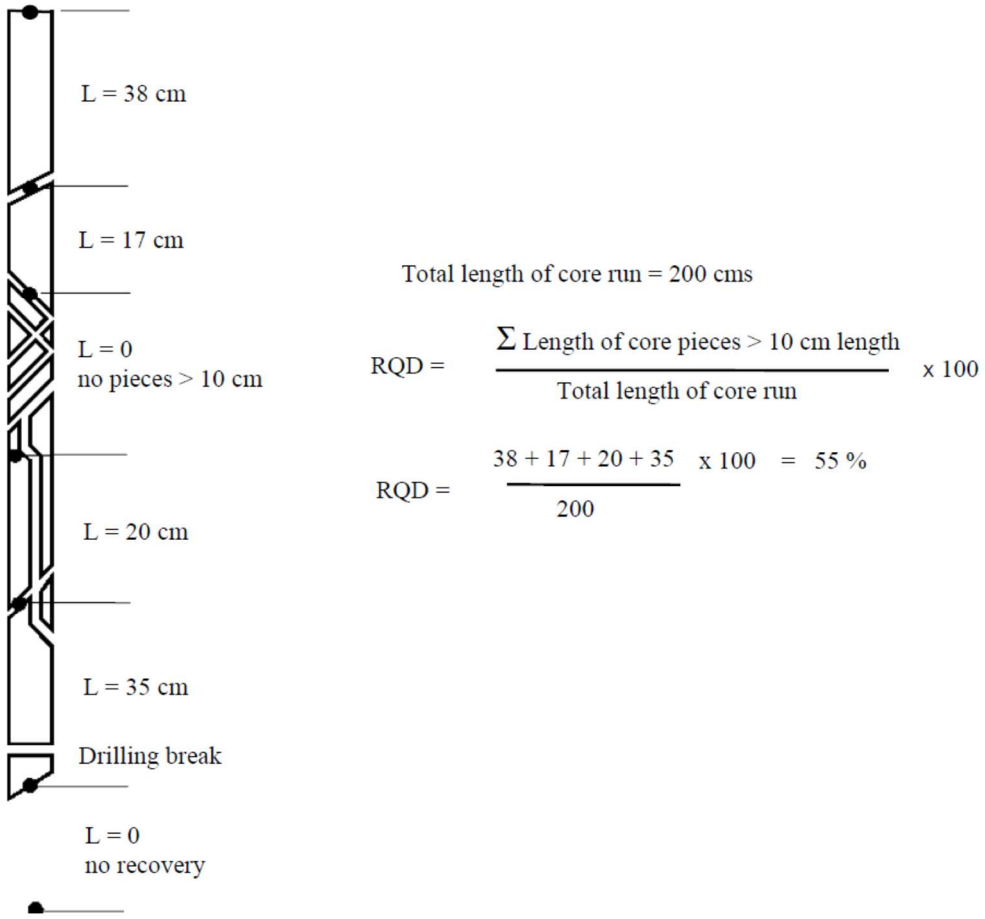

Figure 47: procedure for measurement and calculation of RQD (after Deere, 1989).

Table 20: relation between RQD and the rock mass quality.

RQD (%)	Rock mass quality
<25	Very Poor
25-50	Poor
50-75	Fair
75-90	Good
90-100	Very Good

6.1.2. The Rock Mas Rating classification system (Bieniawski, 1989)

In 1976, Bieniawski published the details of a rock mass classification system called Rock Mass Rating (RMR). Over the years, this system has been refined and the final version (1989) is one of the most reliable classification methods in the rock mechanics. This system allows classifying a rock mass, from the geomechanical quality point of view, according to 6 parameters:

A1) Uniaxial Compressive Strength (UCS) of the rock material.

A2) RQD

A3) Spacing of discontinuities.

A4) Condition of discontinuities.

A5) Groundwater condition.

A6) Orientation of discontinuities (to take into account only for mining purposes).

Since generally a rock mass can be affected by a certain degree of heterogeneity, it should be divided into *structural regions* to be classified separately. The boundaries of such regions are usually defined by a major structural feature, such as a fault, or by a change in rock type. Sometimes, relevant changes in geostructural features or rock properties, within the same rock type, may necessitate the further division of the rock mass into smaller structural regions.

Based on the results of the rock mass survey, a score is assigned to each parameter above mentioned by solving proper equations. For expeditious computations, the ranges of values reported in **Table 21** can be taken into account for the assignment of a score to each parameter. Finally, the sum of all the resulting scores represents the RMR value.

Since this research does not involve any mining works, A6 parameter will not be considered and the final score can be defined as the *basic RMR* (RMR_b).

Based on the final value, the rock mass can be classified according to five quality classes are defined, as reported in **Table 22**.

$$RMR_b = A1 + A2 + A3 + A4 + A5 \text{ (eq. 3)}$$

Table 21: rating of RMR classification parameters.

A1	**UCS (MPa)**	>250	100-250	50-100	25-50	5-25
	score	15	12	7	5	2
A2	**RQD (%)**	90-100	75-90	50-75	25-50	<25
	score	20	17	13	8	3
A3	**Spacing (cm)**	>200	60-200	20-60	6-20	<6
	score	20	15	10	8	5
A4	**Condition**	Rough, closed, not weathered	Slight roughness, aperture<1mm, slight weathering	Slight roughness, aperture<1mm, weathered	Slickensided, aperture1-5mm,filling<5mm	Smooth, aperture>5mm , filling>5mm
	score	30	25	20	10	0
A5	**Groundwater**	Dry	Damp	Wet	Dripping	Flowing
	score	15	10	7	4	0

Table 22: RMR classes and related geomechanical quality.

RMR	Class	Rock mass quality
100-81	I	Very Good
80-61	II	Good
60-41	III	Fair
40-21	IV	Poor
≤20	V	Very Poor

The utility of RMR_b value resides also on the possibility of employing such value for the indirect estimation of the main mechanical parameters of a rock mass. In particular, cohesion (kPa), internal friction angle (°) and elastic modulus (GPa) can be obtained by the following equations, although several versions are available in literature (e.g. Serafim and Pereira (1983); Nicholson and Bieniawski (1990); Asef et al. (2000)).

$$c = 5RMR_b \qquad \text{(eq. 4)}$$

$$\varphi = 0.5RMR_b + 5 \qquad \text{(eq. 5)}$$

$$E = 2RMR_b - 100 \text{ (for RMR>50)} \quad \text{(eq.6)}$$

$$E = 10^{(RMR-10)/40} \text{ (for RMR<50)} \quad \text{(eq.7)}$$

6.2. Geomechanical classification of surveyed slopes

The Rock Quality Designation was empirically calculated for each rock mass, according to Palmström (1982), along two perpendicular scanlines in order to intercept all the surveyed discontinuity sets. In particular, Dol-1 is the outcrop affected by the best geomechanical quality, showing a RQD value of 85%, thus falling within the I class (very good quality). This datum reflects the field condition, as this measurement station is characterized by a low number of discontinuity systems, if compared to other outcrops of the same rock type, as already pointed out in the rock mass survey section.

Dol-2 and Dol-3 are characterized by a very poor quality, with RQD ranging from 5% and 15%. In fact, such rock masses show an intense degree of fracturing, and sometimes hold also crushed portions. Dol-4, located in the southernmost sector of the study area, lies between classes III and IV, with RQD of 42%, therefore it can be classified as a fair/poor quality rock mass.

Limestones and phorphyroids show a similar fair quality condition, represented by RQD ranging between 53% and 55% at limestones and between 32% and 57% at porphyroids. Even in this case, Por-3 and Por-2 are close to the lower border with the “poor” class.

Med-1 and Med-2 are affected by a condition similar to Dol-3, while Med-3 and Med-4, located in the southern sector of the area are affected by a better quality, given by RQD values from 46% to 49% (**Figure 48**).

RQD values were employed, along with all the other main geomechanical parameters retrieved during the field surveys, for the estimation of the RMR index.

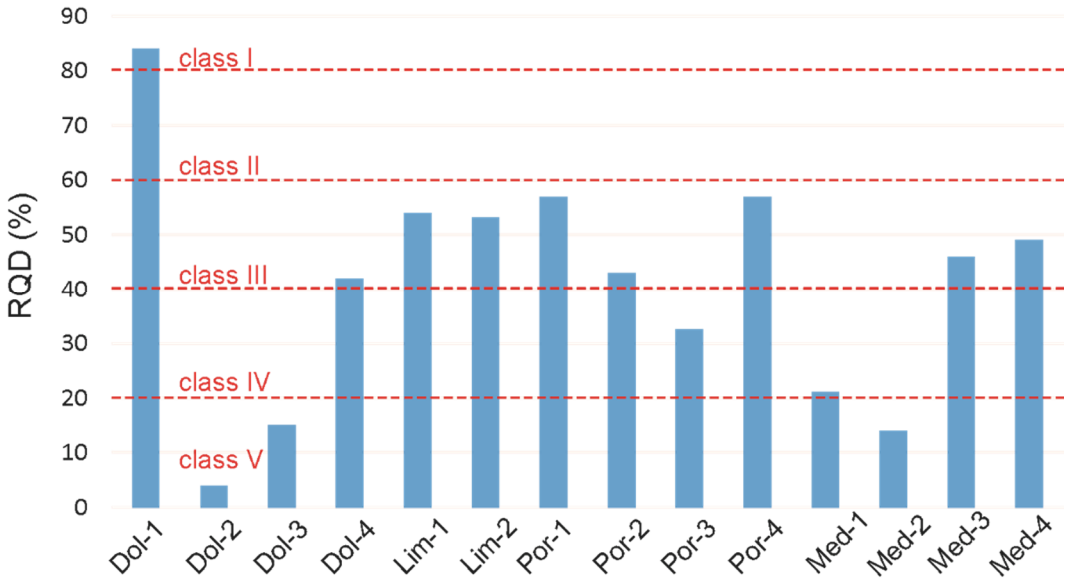

Figure 48: histogram on the RQD values for each surveyed rock mass.

Results (**Table 23**) show that all the slopes fall in the III class (fair quality), according to Bieniawski (1989). One of the most conditioning parameters in this classification system is the *groundwater condition*, whose variation may imply a strong reduction of the final score. In this research, the rock mass condition was assumed as *Damp* because of the presence of widespread vegetation on the slope face, as well as of slight weathering affecting some planes, index of water circulation within the rock mass.

Moreover, considering that the transition RMR value between classes III and IV is 40-41, it is worth noting that Dol-2, Dol-3, Med-1 and Med-2 are very close to the Poor class. This is a confirmation of the poor geomechanical quality of these slopes, already supposed during the in situ survey, as can be deduced by **Figure 49**.

According to the equation reported in the previous section, the main geomechanical parameters of the rock mass were empirically calculated. Besides slight values of cohesion, an interesting consideration concerns to the internal friction angle values. In fact, for all the rock mass except Dol-1, they do not exceed 30°, which is a low value for rock masses. This is symptomatic

of the bad mechanical condition of the rock masses taken into account herein and represents an "alarm bell" for a series of potential instability.

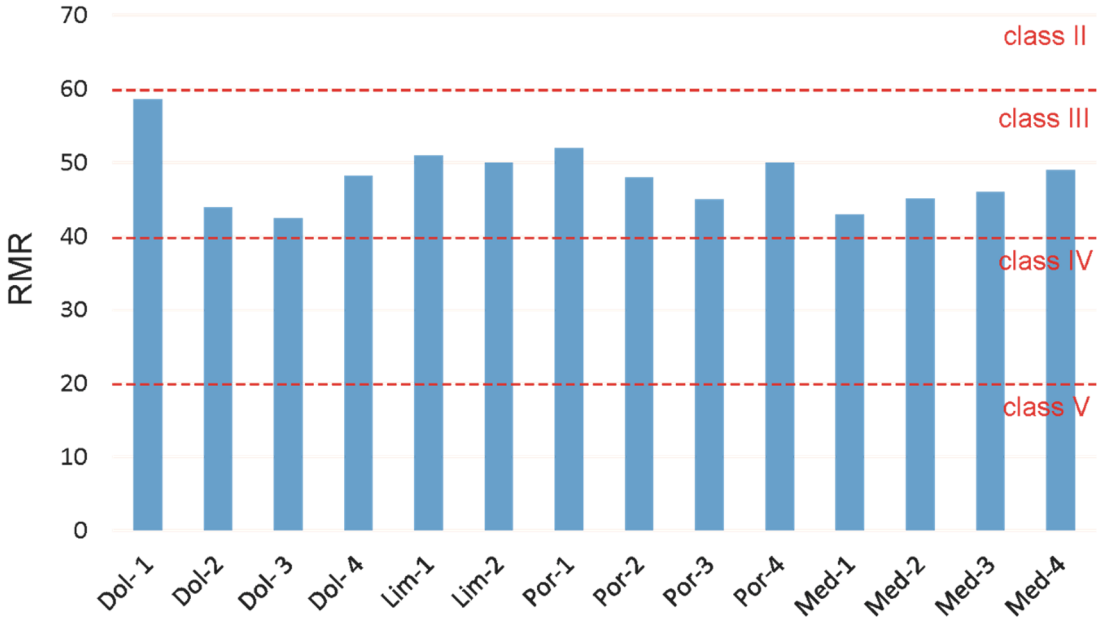

Figure 49: histogram on the RMR values for each surveyed rock mass.

Table 23: RMR classification scores for surveyed rock masses and related geomechanical parameters.

Station	A1	A2	A3	A4	A5	RMR_b	Class	c (kPa)	φ(°)	E (GPa)
Dol-1	4	19	12	13	10	58	**III**	290	34	16
Dol-2	5	3	6	20	10	44	**III**	220	27	7
Dol-3	5	3	6	19	10	43	**III**	215	26	7
Dol-4	5	9	7	17	10	48	**III**	240	27	9
Lim-1	5	11	8	17	10	51	**III**	255	30	10
Lim-2	5	11	7	17	10	50	**III**	250	30	10
Por-1	5	11	11	15	10	52	**III**	260	31	10
Por-2	5	9	9	15	10	48	**III**	240	29	9
Por-3	5	7	7	17	10	46	**III**	230	28	8
Por-4	5	11	6	17	10	50	**III**	250	30	10
Med-1	4	5	7	16	10	42	**III**	210	26	7
Med-2	5	5	7	18	10	45	**III**	225	27	7
Med-3	5	9	9	13	10	46	**III**	230	28	8
Med-4	5	10	7	17	10	49	**III**	245	30	9

CHAPTER 7

INFRARED THERMOGRAPHY SURVEY

In the previous sections, the key role played by both the jointing and the condition of discontinuities in the stability of rock slopes was discussed, highlighting the importance of the in situ survey for the slope modeling.

Nevertheless, according to the growth of technology, satisfactory outcomes are nowadays achieved also through remote surveys, which are often considered important support methodologies to the field campaign. In this light, looking for an innovative and scientifically interesting approach in the rock mass survey, the InfraRed Thermography (IRT) was tested herein as a pioneering remote survey methodology to find out what kind of information can be retrieved by its application in the study of fractured rock masses.

The experience and procedures reported in this section are probably the first complete international attempt, focused and properly developed for the study of the rock mass fracturing (Mineo et al., 2015a; Pappalardo et al., 2016a).

7.1. The InfraRed Thermography technique

Electromagnetic radiation travels in waves and spans a wide spectrum from very long radio waves to very short gamma rays. This spectrum is divided into a number of regions, called “bands”, distinguished only by their wavelength (**Figure 50**). Among these, the Infrared band, lying between the visible and the microwave bands, comprises the wavelengths ranging between 0.7 and 1,000 μm (e.g. DeWitt, 1988; Wolfe and Zissis, 1993). All forms of matter, with temperature above the absolute zero, emit thermal radiation as a result of thermally excited electron oscillations or transitions within the matter itself; its intensity is function of the temperature of the material. Thermal radiation occurs in the portion of the spectrum between 0.78 and 1000 μm, including parts of the ultraviolet, along with all visible and infrared regions (**Figure 50**).

However, most of the thermal radiation falls in the infrared part of the spectrum, so it is not detectable by human eyes. According to the known optical principles, the radiation can be deflected, focused with a lens, or reflected from surfaces (Hillel, 1998). Based on the amount of energy reflected or absorbed by a body, emissivity ranges from 0 (when all the energy is reflected) to 1 (when all the energy is absorbed). The last condition is related the "black bodies", which are capable to re-emit 100% of the absorbed energy. However, these cases are purely theoretical, since bodies capable to reflect or absorb all the radiation do not exist in nature. All the materials have intermediate emissivity values and are known as "grey bodies". Mathematically, emissivity is the ratio between the infrared radiation emitted by a body and the radiation emitted by a black body at the same temperature. According to the Stefan-Boltzman law (eq. 8), the total energy emitted by a body (J), across all wavelengths, is proportional to the Stefan-Boltzman constant (σ), to the surface temperature of the body (T) to the fourth power and to its emissivity (ε) (Hillel, 1998).

$$J = \varepsilon \sigma T^4 \qquad \text{(eq. 8)}$$

Based on these concepts, the InfraRed Thermography (IRT) technique allows determining the temperature of an object by capturing its emitted infrared radiation (Shannon et al., 2005) and subsequently by converting it to temperature. The device able to perform such operation is the thermographic camera, which generally operates in the range of wavelengths as long as 13-14 μm and building images using the infrared radiation. The output is a color-scaled image representing a map of the temperature variation. Each image consists of a matrix of pixels whose values are analyzed by softwares allowing, among other things, the isolation of specific temperature ranges, the detection of thermal anomalies, the measure of a temperature difference between two

or more points/pixels, the choice of the most suitable color palette. However, the radiation measured by the camera depends not only on the temperature of the object, but it also originates from the surrounding environment; this is the case of the "parasite radiation", which is reflected by the object and partially absorbed or dispersed by the atmosphere (Prendes-Gero et al., 2013; FLIR, 2015).

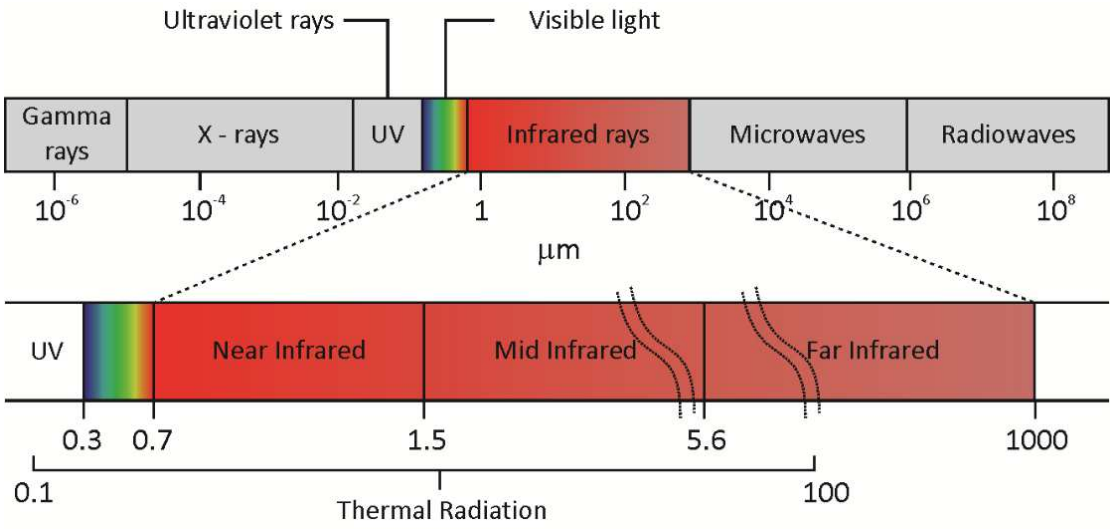

Figure 50: schematic representation of the electromagnetic spectrum (after Pappalardo et al., 2016a).

7.2. State of the art on the application of IRT in the geosciences

The main advantages of IRT reside in its non-destructive application, rapidity of execution and absence of contamination risk (Kastberger and Stachl, 2003; Liu et al., 2011). Moreover, since it is a remote sensing methodology, it can be used for a great variety of purposes and for the investigation of several phenomena spanning many fields, such as military, industry, medicine, and science (Hudson, 1969).

Currently, infrared imaging system is being applied in the medical field (Meola and Carlomagno, 2004), botany (Wisniewski et al., 1997), environmental pollution (Cehlin et al., 2000), to monitor mechanical equipment at electric

power plants and to investigate convective heat fluxes over complicated body shapes (Shannon et al., 2005). In civil engineering and architecture, it proved a useful technique for the detection of building defects, such as thermal bridges, air leakage or moist spots, particularly in the context of energy conservation (e.g. Grinzato et al., 1998; Titman, 2001; Tavukcuoglu et al., 2005; Cluni et al., 2015). In earth sciences, IRT is applied also to monitor high-temperature volcanic gases arising from the magmas (Furukawa, 2010), while in engineering geology it allows the detection of crevasses and cave openings along a slope by exploiting the difference of temperature between the inner part of the void and the external environment (Rinker, 1975). It was also used for mapping open fractures along unstable rock slopes of Czech Republic and Austria (Baron et al., 2012), while Teza et al. (2012) proposed a method based on the analysis of thermal images taken during the night cooling of a rock cliff. Wu et al. (2005) applied this technique to assess the integrity of rock mass behind a shotcreted slope and Mineo et al. (2015b) used IRT as a complementary technique to identify potential source areas for rockfalls along an unstable slope in northern Sicily. More recently, Mineo and Pappalardo (2016a-b) tested a pioneering methodology for the indirect estimation of porosity in intact rock through the analysis of thermograms and the monitoring of the cooling behavior of artificially heated specimens. Furthermore, Pappalardo and Mineo (2017) proved that IRT can be useful also in the identification of the persistence and interconnection of voids in intact rock specimens.

7.3. IRT shooting campaigns

7.3.1. Brief introduction

According to the theoretical principles of IRT, thermograms show the surface temperature values at the surveyed rock masses, highlighting the differences in a color-scale image. One of the purposes of the experimental application of IRT in this research is to find out if the thermal output is related either to the degree of fracturing or to some peculiar features of the rock mass, so to establish the utility of this methodology in this field of sciences. To this purpose, the acquisition of thermograms was carried out at some of the outcrops surveyed and commented herein, so to ensure a reliable comparison with the IRT output. Furthermore, shooting sessions took place at different times of the same day, so to look for differences between thermograms at different daily conditions. Nevertheless, the study area is affected by strong seasonal climate changes; therefore, the same campaign was performed both in the warm and in the cold seasons. In this way, a complete comparison between daily and seasonal thermograms would allow understanding not only what kind of features are highlighted by IRT, but also if a specific time of the day can be suggested as the ideal time-condition for the shots.

Moreover, the acquisition of several images at different phases of the day, allowed monitoring the daily temperature variation at each outcrop. Daily variations are likely to depend on the sun exposure and on the heat exchange between the rock mass and the external environment, while seasonal variations are related to the different climate conditions affecting the heating and the cooling phases of the rock itself.

Temperature records were used for the reconstruction of the cooling trend of the rock masses, describing the decrease of the temperature during the survey time. Interesting considerations are proposed herein with reference to a new index, properly named Cooling Rate Index (CRI), estimated to study how rock

masses, conditioned by the fracture nets, behave while transferring heat to the external environment. Such behavior was related to the degree of fracturing of the rock masses, in order to find a relation linking the IRT data to the main quantitative fracturing indexes (i.e. Volumetric Joint Count and Rock Quality Designation according to Deere, 1963 and Palmström, 1974, respectively).

7.3.2. Field methodology

For the IRT campaigns, six rock masses facing NE were chosen, so to ensure a direct sun radiation in the morning and shadow condition during the afternoon. In particular, dolostone, limestone and phorphyroid outcrops were thermally mapped during one-day surveys both in the dry and cold seasons, with the aim of evaluating what kind of differences occur within daily and seasonal thermograms. Campaigns were carried out in June (**Figure 51**a) during a sunny day, and in January during a cloudy, partly rainy day (**Figure 51**b). From now on, the June and January surveys will be referred to as "summer campaign" and "winter campaign" respectively.

The image acquisition was conducted by using a FLIR B-335 infrared camera, with accuracy calibrated within +/– 2°C or +/– 2% of reading, a range of measurable temperature between -20° and +120° C, a spectral range of 7.5–13 µm and an integrated laser pointer. A tripod ensured immobility of the camera during the shots, while a marking pen was used to mark the laser point on the rock mass. The camera had a constant horizontal trim and the shooting point was located about 3 m away from the slopes, so to have a significant detail in the picture, while the position of the tripod was marked on the ground to maintain always the same shooting point during the surveys. A handheld sensor was employed to measure ambient temperature and relative humidity, while the emissivity coefficient was assumed according to Hudson (1969) and FLIR (2015).

In both campaigns, thermograms were acquired at four different times of the same day, based on the seasonal daylight condition, as follows (Pappalardo et al., 2016a):

1) t1: images taken in the morning, when the sun radiation directly hit the slope face, especially in June, transferring heat to the rock mass.

2) t2: images taken at noon, when the slope had just been shadowed. In this phase, the heat transfer may occur both from the external environment towards the rock mass and vice versa.

3) t3: images taken in the afternoon, when the slope had slowly been cooling down for some hours, releasing heat from the inside towards the external environment.

4) t4: images taken at nighttime, with absence of parasite radiation. In fact, neither natural nor artificial source was lighting the slope face.

After the acquisition stage, images were processed by the software FLIR Tools, a suite specifically designed to edit radiometric images to thermal tune level and span, change the palette, or adjust parameters such as emissivity and reflective temperature. In particular, it also allows measuring temperatures using spots, areas, lines and isotherms, highlighting difference of temperature within the same photo, isolating specific temperature ranges and defining the best representative output.

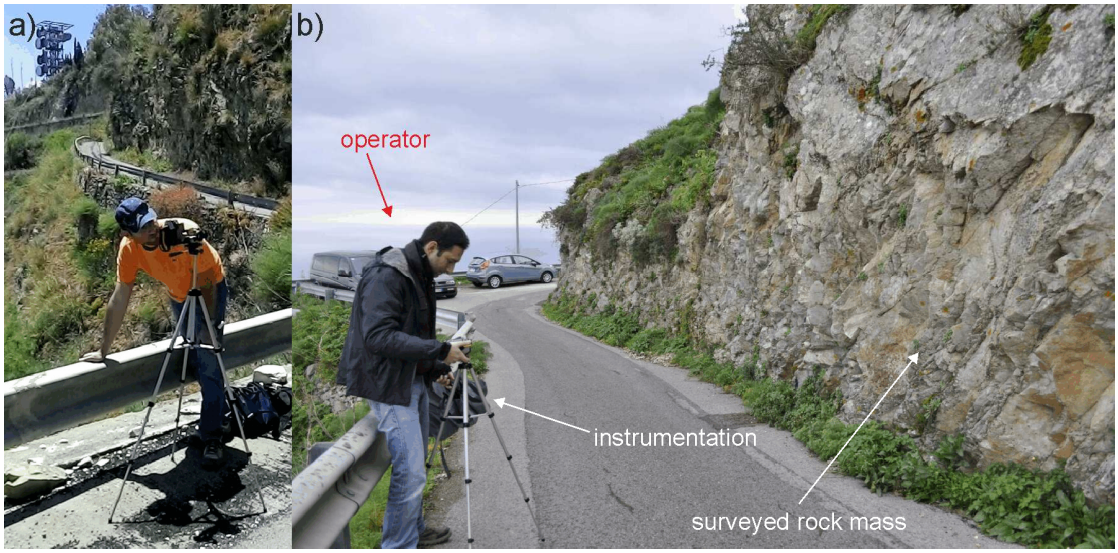

Figure 51: field operation during the summer (a) and winter (b) campaigns (after Pappalardo et al., 2016a).

7.3.3. Comparison of daily thermograms

In the summer campaign, during the first shots (t1), due to the strike of the surveyed rock faces (facing northeast), the sun had been irradiating the rock masses since the sunrise. As long as the sun radiation hits the rock face, the heat transfer to the rock mass mainly occurs through radiation and conduction (Adamovsky et al., 2012). However, the irregularity of the slope, resulting in an indented rock face, leads to a non-uniform warming of the rock, which is known to be a bad heat conductor (De La Beche and Broderip, 1972). Therefore, jutting portions are radiated by the sunrays, gaining heat and projecting their shadow on the hollow parts. In this way, the only information retrievable by heating thermograms (t1) is related to the three-dimensionality of the slope, since the hottest sectors are those directly affected by the sun radiation (juts) while the coldest are the shadowed parts (hollows) (**Figure 52**, **Figure 53**, **Figure 54**).

When the direct radiation is over, all the gained heat is slowly released through the discontinuity systems, from the inner rock mass outwards. This is the beginning of the rock mass cooling, characterized by various thermal anomalies, whose definition increases as the external temperature decreases.

In particular, positive anomalies are typical of fractures, caves and hollow parts, which remain warmer, while negative anomalies are related to low fractured planes, as well as weathered portions and jutting sectors, which are more exposed to the ventilating air. Nevertheless, since natural light is still present at t2 and t3, the influence of parasite radiations cannot be excluded. In nighttime (t4), when neither artificial nor natural sources light the slope, i.e. thermal radiation is no longer influenced by parasite disturbs, the best IRT output is achieved (**Figure 52**, **Figure 53**, **Figure 54**). In this phase, the highest temperatures are related only to the main discontinuity systems, along with the most fractured/hollow sectors where sometimes it is hard to detect defined structures.

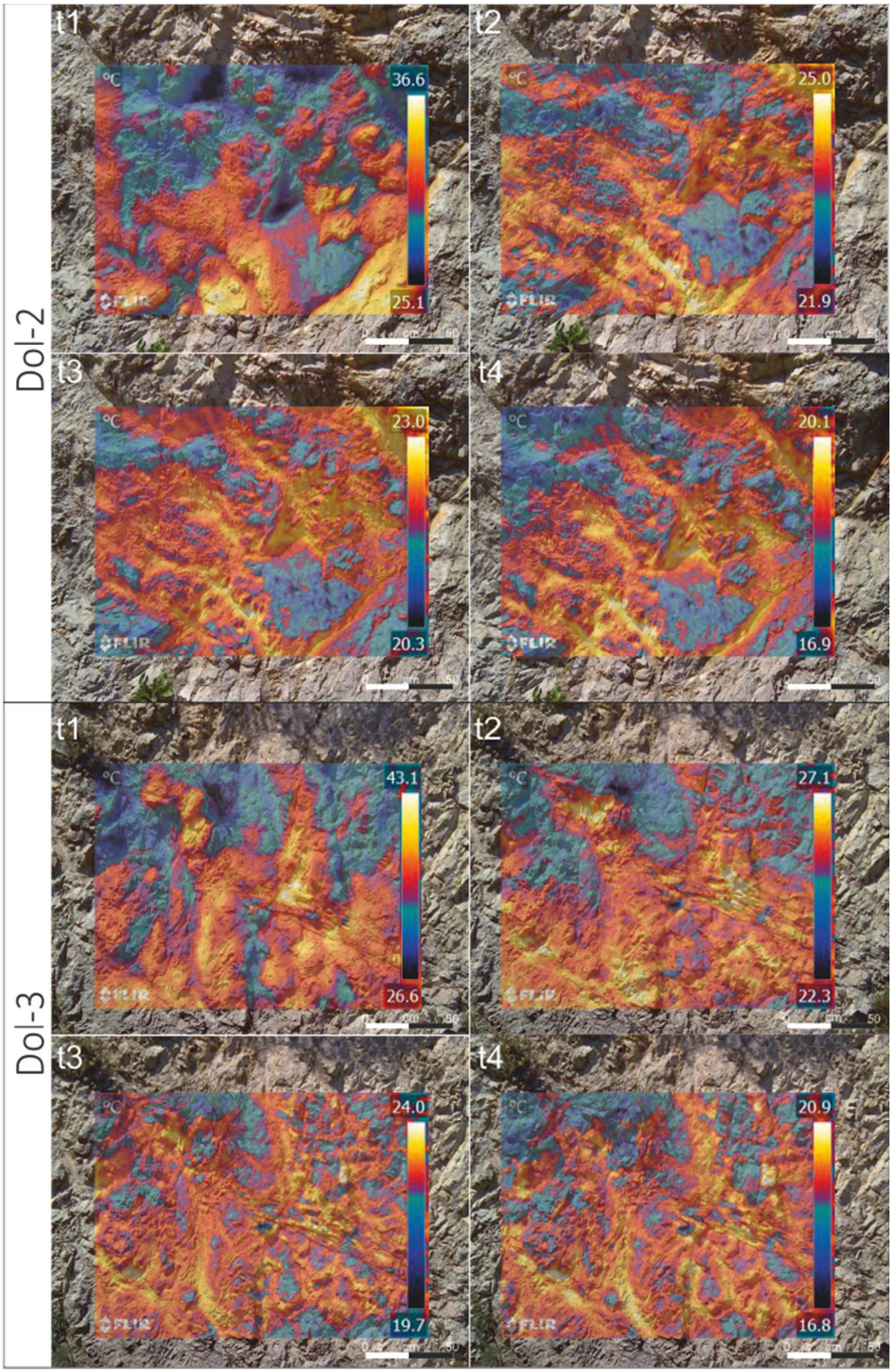

Figure 52: dolostone thermograms overlapped to a digital photo of the rock mass. Thermograms refer to the different summer daily stages, while the rock mass photo on Background was taken in daylight (after Pappalardo et al., 2016a).

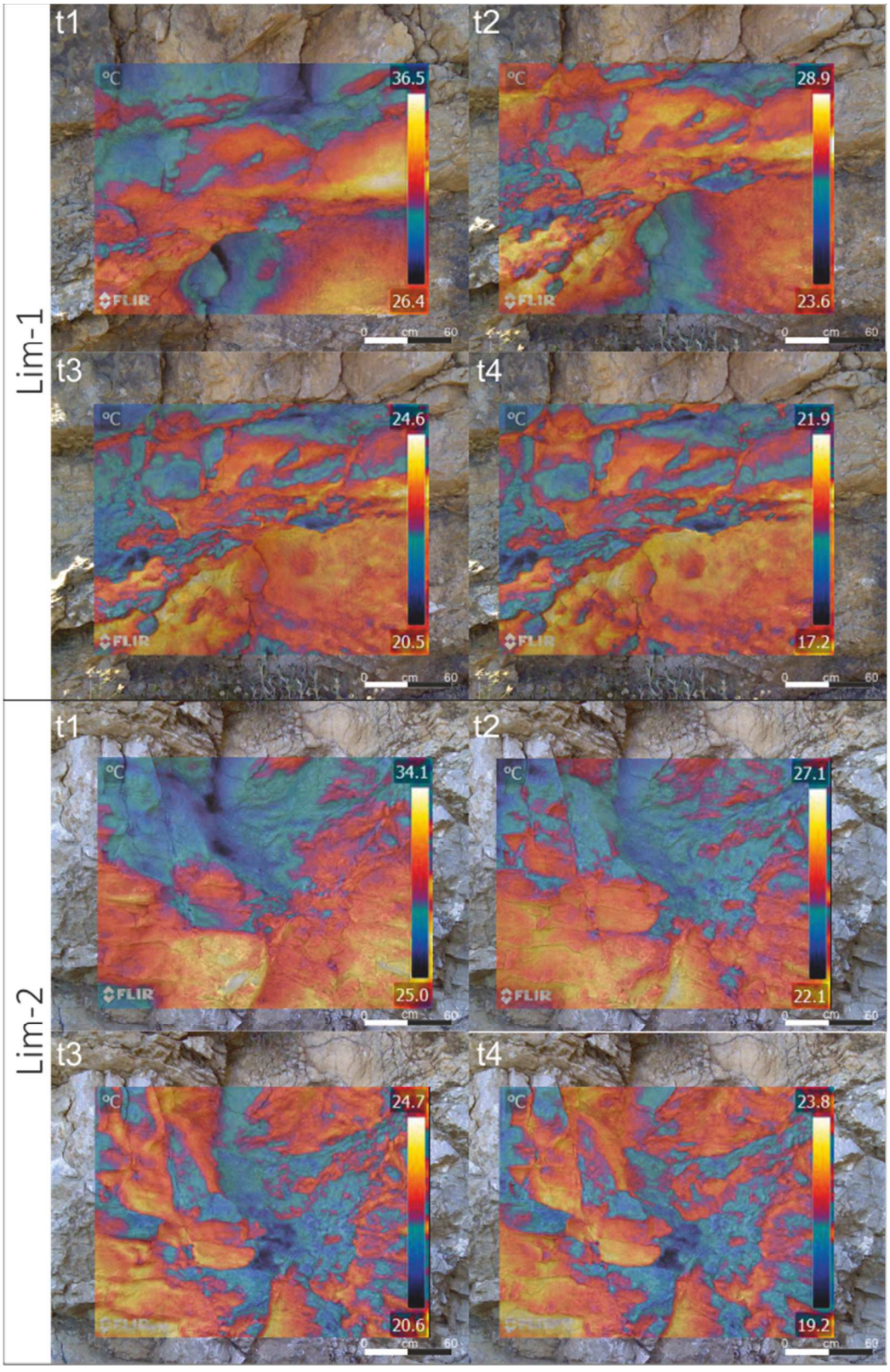

Figure 53: limestone thermograms overlapped to a digital photo of the rock mass. Thermograms refer to the different summer daily stages, while the rock mass photo on Background was taken in daylight (after Pappalardo et al., 2016a).

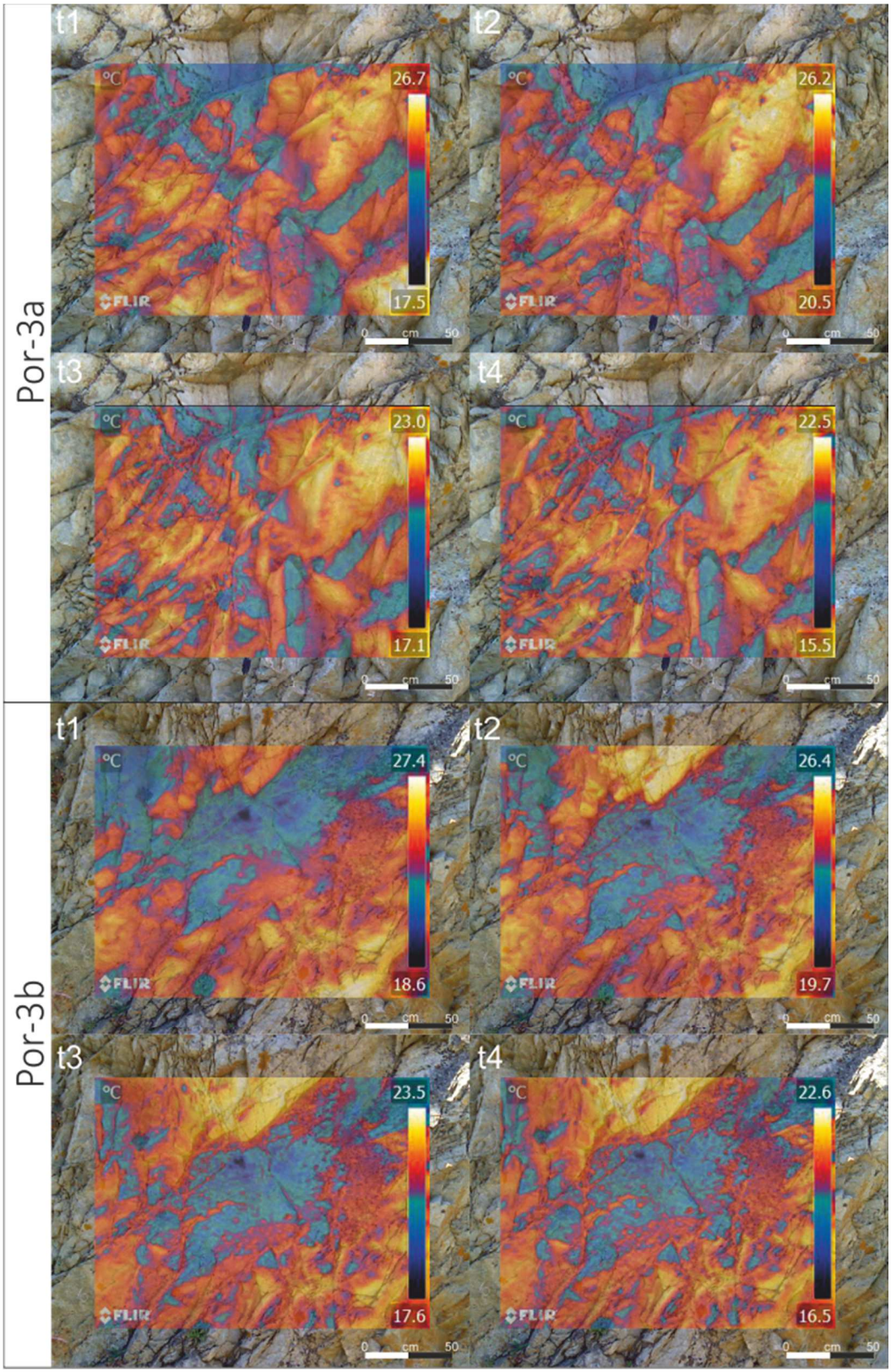

Figure 54: porphyroid thermograms overlapped to a digital photo of the rock mass. Thermograms refer to the different summer daily stages, while the rock mass photo on Background was taken in daylight (after Pappalardo et al., 2016a).

7.3.4. Comparison of seasonal thermograms

By repeating the daily surveys at the same rock masses in the cold season, the acquired thermograms were compared to find out what differences occur between summer and winter images.

The first dissimilarity is in the definition of the winter thermograms, which generally look poorly defined and, sometimes, blurred (**Figure 55**). This is likely due to the weather conditions since, unlike the summer campaign, the winter shots were performed in a cloudy and partly rainy day (although shots were taken in absence of rain to avoid whatever effect on the image). Clouds behave as a natural filter on sunrays, therefore there is no direct radiation at the rock face and the warming of the rock is rather weak. This condition results in less-heated rock masses, characterized by a narrow range of temperatures. Indeed, assuming the algebraic difference between the maximum and minimum temperatures recorded in each survey phase as ΔT_{rm}, it can be noticed how all the rock masses show a summer ΔT_{rm} noticeably wider than the winter ΔT_{rm} (**Figure 56**). Such a difference is emphasized at t1, since the heating conditions are different in summer and winter. This means that in winter, if the direct radiation of the rock face is not present, the temperature of the rock mass is almost constant, with small fluctuations, resulting in a less defined IRT output. Moreover, the wet rock face in winter may be the cause of the blurred effect occurring in some images, although no water flow has been observed along the discontinuity systems. However, for both summer and winter campaigns the best IRT output is achieved with nighttime shots (t4), although summer images are more detailed (**Figure 55**).

Another difference was found in the t1 thermograms: summer t1 images allow the recognition of jutting and hollow portions of the rock face, but when the direct radiation does not take place (because of clouds) the rock mass does not show hot radiated sectors that may be related to jutting portions of the rock

mass itself. Therefore, heating proceeds in a uniform way and the information retrievable from t1 winter images are comparable with those belonging to cooling phase images, although with a low definition (**Fig. 57**).

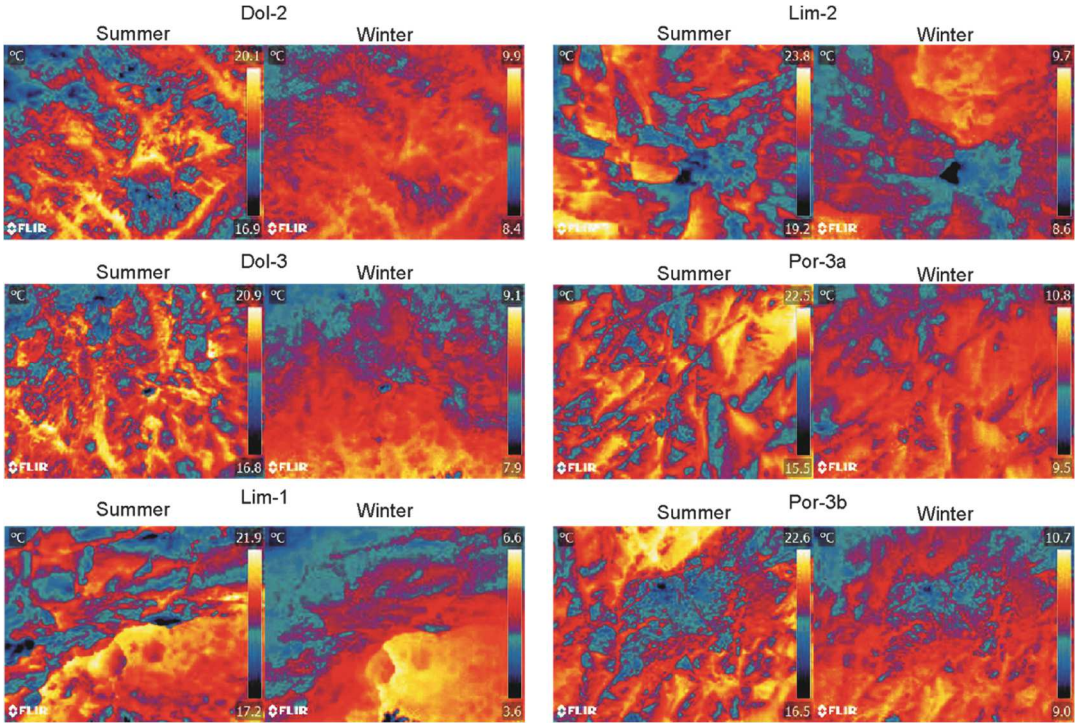

Figure 55: comparison between t4 thermograms of summer and winter campaigns (after Pappalardo et al., 2016a).

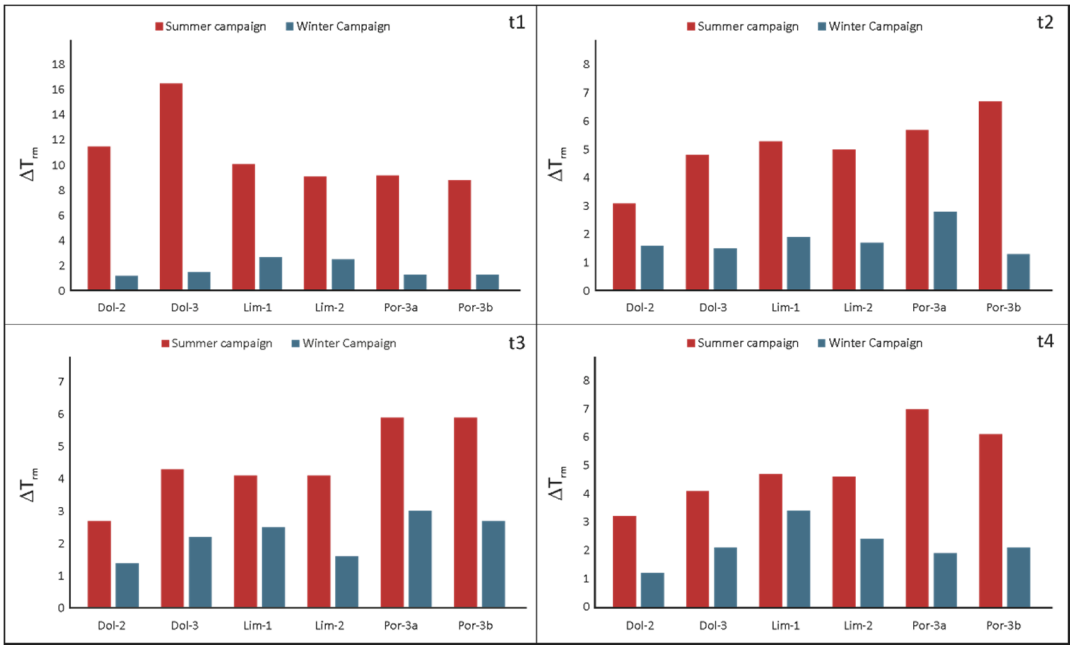

Figure 56: histograms reporting the temperature variation of rock masses (ΔT_{rm}) for each survey stage (after Pappalardo et al., 2016a).

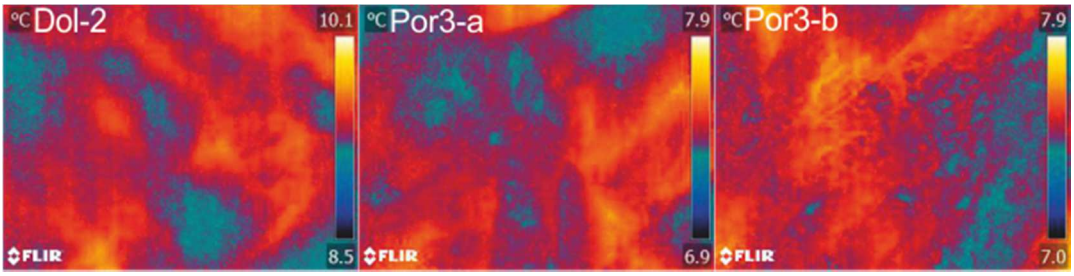

Fig. 57: t1 winter representative thermograms, showing the blurred effect due to the low warming of the rock mass (after Pappalardo et al., 2016a).

7.4. The Cooling Rate Index

7.4.1. Temperature curves and CRI

Based on the recorded temperatures, the cooling behavior of the rock masses was studied and a specific index, which numerically describes it, was calculated. The digital processing of IRT images allows the estimation of the maximum, minimum and average temperatures captured by the infrared camera. While maximum and minimum temperatures are related to one or more pixels of the image, the average temperature is a weighted value of the whole thermogram. In order to describe the thermal behavior of the rock masses, the average temperatures of each rock mass was plotted against time on a two-variable diagram. The thermal behavior is outlined by a curve (**Figure 58**), where heating and cooling phases are described by increasing and decreasing trends respectively (Pappalardo et al., 2016a). According to Newton's Law of Cooling, the loss of heat of an object in a colder environment is described by a cooling curve, where the slope of the tangent to the curve at any point gives the rate of fall of temperature. From now on, I will refer to this rate as the rock mass Cooling Rate Index (CRI), which can be calculated by equation 9, representing a temperature variation per unit of time (Pappalardo et al., 2016a):

$$\mathrm{CRI} = \frac{\Delta T}{\Delta t} \qquad \text{(eq. 9)}$$

where ΔT is the variation of temperature and Δt is the considered time interval. The higher CRI, the faster the rock mass cooling. In this view, dolostone rock masses are characterized by summer curves showing decreasing trends, where the heating condition is related to t1, and the cooling phase occurs in the time interval t2-t4. Cooling phases of Dol-2 and Dol-3 are characterized, on average, by CRI of 0.65° and 0.84° per hour respectively.

Also limestones show decreasing temperatures during the IRT summer survey, with average CRI ranging between 1.02° (Lim-1) and 0.41° per hour (Lim-2). However, Lim-1 is a particular case, since it is characterized by a hollow portion, which behaves like a cavity preserving warm air and, sometimes, enhancing its cooling when external temperature lowers. This condition explains why so different CRI values have been obtained at two similar rock masses.

On the other hand, a different behavior is held by porphyroids; indeed, a slight heating phase between t1 and t2 is outlined. This is due to the local setting, since Por-3a and Por-3b are partly shadowed by a protruding upper portion of the rock face at t1. In this case, direct radiation is partly inhibited, so the warming of the rock mass is slower and lasts until t2, when the cooling phase begins, with average CRI of 0.58° per hour in both cases.

An interesting aspect is related to the late cooling phases of the rock masses, occurring between t3 and t4. In fact, while limestones and phorphyroids show a sub-horizontal curve in the last stretch, dolostone curves are affected by an increasing slope (i.e. higher CRI). It is known, by Newton's Law of Cooling, that the rate of change of the temperature is proportional to the difference between the temperature of the rock mass and the ambient temperature. This means that the cooling of a body is faster when the difference with the ambient temperature is higher. Therefore, both limestones and porphyroids reach a thermal equilibrium with the external environment during the t3-t4

phase. On the other hand, the increase of CRI, with a maximum value of 1.28° per hour at D2, means that the cooling phase of dolostones had not finished yet at t4 and that it had been accelerating since the external temperature was lowering after the sunset. The winter curves (**Figure 58**) show that in the cold season the rock masses are characterized by narrow ranges of temperature. Dol-2 is characterized by a sub-horizontal curve, while Dol-3 has a weak heating phase between t1 and t2. The other rock masses gain heat until t3; then the cooling phase begins with CRI ranging from 0.28 (Por-3b) to 0.56° per hour (Lim-2). L1, with a 2.2° per hour, is an exception because of the morphology of its rock face, as highlighted above. As a result, when the direct radiation of the rock face is absent, the heating proceeds in a slower and more uniform way. Otherwise, it is necessary to wait for the shadowing of the rock face before being allowed to study the cooling behavior of the rock mass.

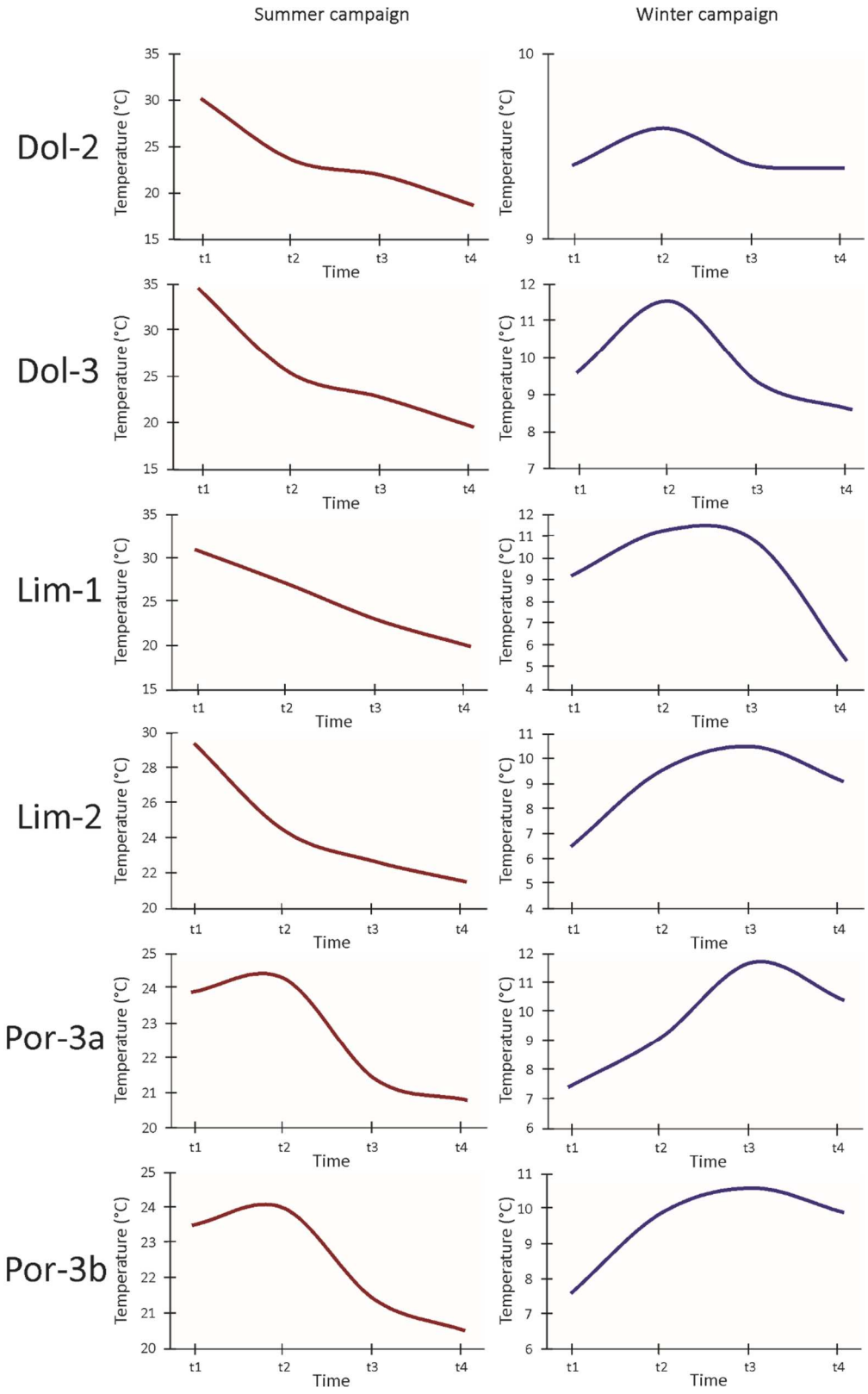

Figure 58: temperature curves for each surveyed rock mass (modified after Pappalardo et al., 2016a).

7.4.2. Correlation with RQD

Literature data demonstrate that the thermal characteristics of rock masses are strongly conditioned by its macroscopic and microscopic fracturing (Squarzoni et al., 2008). After having introduced CRI, which can be considered an index describing the cooling velocity of the rock mass, a further challenge of this research is to find out a relationship between CRI and the fracturing condition of the rock.

The main quantitative rock mass engineering classification systems take into account, either explicitly or implicitly, this aspect by involving the geomechanical parameter of Rock Quality Designation (RQD).

RQD was developed by Deere et al. (1989) to provide a quantitative estimate of rock mass quality from drill core logs giving an average measurement of the degree of jointing along a section (Palmström, 2005).

By plotting RQD against CRI, a negative linear relation is found. This means that as the RQD increases (i.e. improvement of the rock quality) CRI decreases (**Figure 59**); this is easily guessed since the intact rock (with no visible fractures) is a bad conductor of heat. The best fitting of such relationship was obtained by taking into account the CRI calculated only within the summer nighttime cooling phase (t3-t4), when the difference with the ambient temperature is maximum. Indeed, the cooling of rock masses will accelerate proportionally to their degree of fracturing, resulting in higher CRI (**Figure 59**).

Such relationships show the reliability of CRI as a potential index for the remote estimation of the quality/degree of fracturing of a rock mass, although further measurements at outcrops with different properties should be performed.

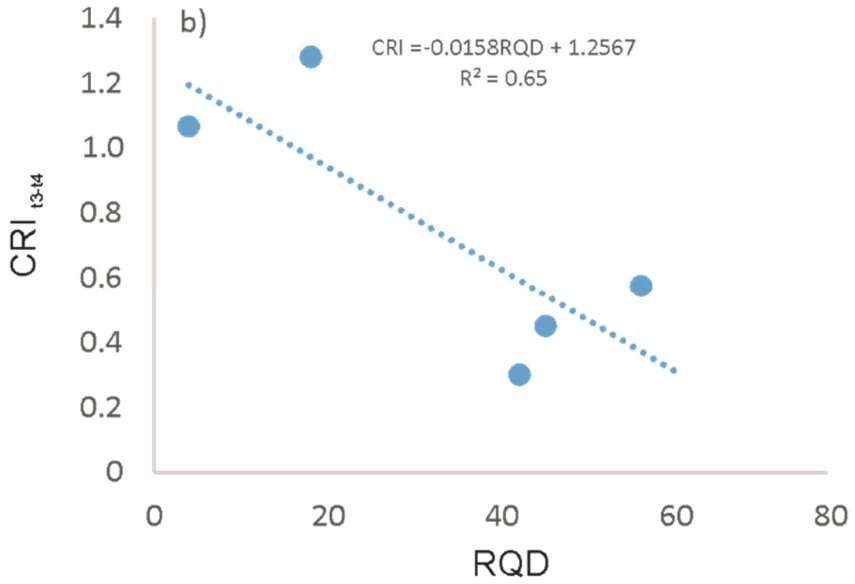

Figure 59: relationship between CRI t3-t4 and RQD.

CHAPTER 8

ROCKFALL TRAJECTORIES ANALYSIS

The rockfall phenomenon takes place in two distinct stages: the initial–failure stage, describing the instability condition of the slope and the circumstances triggering the detachment of a number of blocks, and the post failure stage, describing the motion of those blocks along the slope.

While the first stage has already been addressed in the previous sections, ascertaining the widespread instability affecting the study area, the post failure stage is analyzed herein.

In this perspective, this section provides the results of the statistical analysis performed by simulating the rockfall trajectories, with the aim of studying the behavior of falling boulders and identifying the potential elements at risk. Rockfall simulations were carried out by using both bi-dimensional and three-dimensional codes and by taking into account numerous representative sections (2D) and the morphology of the area (3D).

8.1. Theoretical background

Once the movement of a rock boulder along a slope has been initiated, the falling block will rebound or roll along the slope, following a specific trajectory, until the morphological condition (or other external factors) will allow it to stop. The major difficulty in modeling the behavior of a rockfall event is characterizing all the dependent variables thoroughly (De Almeida and Kullberg, 2011). Indeed, the relative movement of a falling boulder down a slope depends on a series of factors: the rock lithology, the topography and gradient of the slope (Parise, 2002), the size and shape of the boulder (Schweigl et al., 2003). Consequently, it is certainly not a simple problem to forecast a rockfall trajectory accurately. In particular, among the most important features controlling the fall trajectory, the geometry of the slope and its constituting

the material play a key role. In the first case, the inclination of the face affects the horizontal and vertical components of the block movement after a rebound, while the material laying above the slope controls the energy of the block itself. For example, a bare rock surface does not retard the movement of the falling or rolling block to any significant degree. On the other hand, surfaces covered in talus material or gravel absorb a considerable amount of energy, slowing the falling rock down until a complete stop. This example introduces the essential concept of the energy exchange between the block and the slope surface. In this kind of analysis, such interaction is simulated through the *coefficients of restitution (CR)*, which are defined as the decimal fractional value representing the ratio of velocities (or impulses or energies) before and after an impact of two colliding entities (or a body and a rigid surface) (Asteriou et al., 2012). Theoretically, a perfect elastic collision is represented by a CR=1, while an inelastic collision is given by CR<1. On the other hand, a CR that equals zero is obtained when the object instantaneously stops at the surface without bouncing, describing a plastic behavior (Goldsmith, 1960). In real rockfall cases, each interaction between the block and the slope is accompanied by a certain energy dissipation and, when in contact with the slope, the magnitude of the block velocity changes according to the CR value. It is self-evident that CR is assumed to be an overall value taking into account all the characteristics of the impact and its calibration is therefore essential for a correct and reliable simulation procedure.

From the kinematic point of view, CR is defined based on the lumped-mass impact theory, according to Newton's theory of particle collision. For an object impacting a steadfast surface the definition, known as kinematic coefficient of restitution (v_{CR}), is simplified as

$$v_{CR} = v_r / v_i \qquad \text{(eq. 10)}$$

where v_r and v_i are the magnitudes of the rebound and impact velocities, respectively (**Figure 60**).

Based on equation 10, CR can be differentiated into normal (Rn) and tangential (Rt) components of impact and rebound velocities, according to equations 11 and 12

$$Rn = v_{nr}/v_{ni} \qquad \text{(eq. 11)}$$

$$Rt = v_{tr}/v_{ti} \qquad \text{(eq. 12)}$$

where v_{nr} and v_{ri} are the magnitudes the magnitudes of the normal (tangential if denoted by the subscript "t" in equation 12), to the steadfast surface, components of the rebound and impact velocities respectively.

Typical values of such coefficients are retrievable in the international literature (e.g., Pfeiffer and Bowen, 1989; Giani, 1992; Robotham et al., 1995; Chau et al., 1998; Dorren and Seijmonsbergen, 2003; Massey et al., 2006; Budetta, 2010; Pantelidis and Kokkalis, 2011; Asteriou et al., 2012; Saroglou et al., 2012), but these values, depending basically on the material type and in some cases on the vegetation cover, can be also estimated by field tests and back analyses taking into account field evidences of previous events. The latter case, with particular reference to the study area, is discussed in the following section.

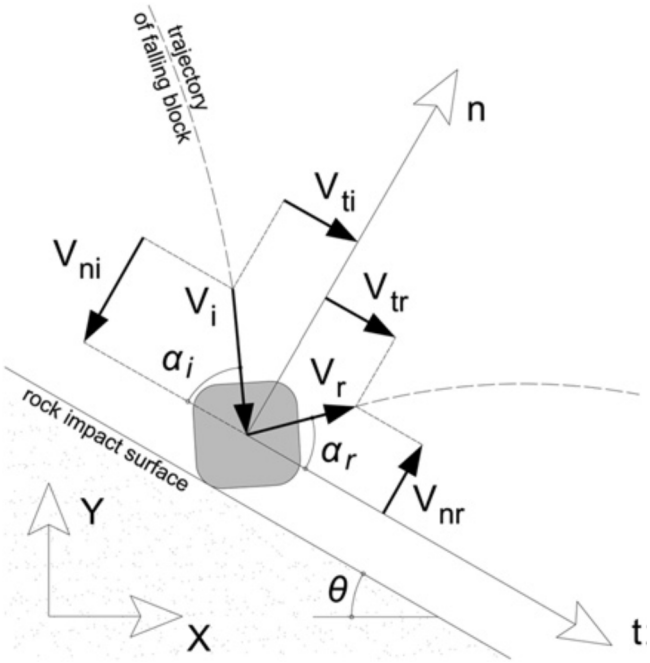

Figure 60: schematic representation of the components controlling the interaction between a block and its impact surface (after, Asteriou et al., 2012).

8.2. Back analyses

The analysis of past rockfalls occurred in the study area is a hard matter, because events were poorly documented over time. The only proof of a widespread instability is the presence of numerous boulders laying along the slopes and the roadsides, supported by tales of local people representing a reliable source. Even the most relevant events, reported in the local chronicles, were poorly studied and never mapped. Therefore, now it is hard to identify their source areas and trace their falling route with the aim of back-assessing reliable coefficients of restitution for the investigated slopes.

A recent scientific study, focused on rockfalls threatening the SP-10 road at MRA, reported on a set of simulations based on coefficients of restitutions retrieved from the international literature (Pappalardo et al., 2014). Furthermore, Pappalardo and Mineo (2015) provided a rockfall model for CA by considering a back analysis performed on some representative trajectories.

Nevertheless, during the field campaigns of this research, two main rockfalls occurred in the Castelmola area. Such events, already described at section 3.4, were taken into account for back analyses to assess the most suitable coefficients of restitution for the studied slopes (**Table 24**).

In particular, the 2014 rockfall affected a steep slope at CA, characterized by a sub-vertical summit portion, mainly showing bare and loosened limestone rock, and by a vegetated sector in its final part (**Figure 61**a). Along the slope, a secondary road is a tourist connection route between Taormina and Castelmola, which is usually traveled on foot by visitors. The initial rock block detached from the steep summit of the cliff (**Figure 61**b), rebounding and rolling as far as the secondary road (**Figure 61**c), where it broke into 3 pieces. The movement of two of them was enhanced by the impact with the road and their fall continued toward the downstream vegetated portion. Here, the blocks were slowed down until the complete stop in one case. The other boulder reached the main road (SP-10) at a rest area on the roadside, leaving evident traces on the asphalt (**Figure 61**d-e-f).

Several rockfall simulations were performed to achieve a reliable model by considering different coefficients of restitution, starting from those already available in literature. In the final model (**Figure 61**a), where 1000 trajectories were simulated, most of the blocks are slowed down and stopped by vegetation in the downstream portion of the slope. Only a small percentage of rocks reaches the rest area and the next roadway.

Similarly, a second back analysis was performed for the 2015 event at MRA (**Figure 62**a). In this case, blocks detached from an unstable limestone outcrop, right downstream a secondary road connecting Castelmola to local villages (**Figure 62**b-c). In this case, the movement started with a rolling path, which evolved into some rebound as the velocity increased along the slope (**Figure**

62d). Blocks reached the main road at an almost 90° bend, stopping in the middle of the road and leaving grooves on the asphalt (**Figure 62**e-f).

Such events, occurred at slopes representative of the whole area, allowed assessing the coefficients of restitution, which were employed for the rockfall simulations discussed in the next sections. In particular, 5 classes of materials were considered:

1) *Bare rock*, mainly affecting the summit of the cliff at CA and the upstream outcrops at MRA.
2) *Rock and vegetation*, affecting the lower sector of CA, where falling blocks are usually slowed down.
3) *Rock with little soil or vegetation* in the middle portions of slopes at MRA.
4) *Rock debris* at CA, especially at the foot of the rock cliff.
5) *Asphalt,* at the SP-10 and secondary roads.

Assessed coefficients are similar to literature data and can be considered representative for all the investigated slopes.

Table 24: Estimated Coefficients of restitution for rockfall simulations.

Material Type	R_t	R_n
Bare rock	0.80	0.50
Rock and vegetation	0.74	0.24
Rock with little soil or vegetation	0.86	0.34
Rock debris	0.65	0.15
Asphalt	0.90	0.40

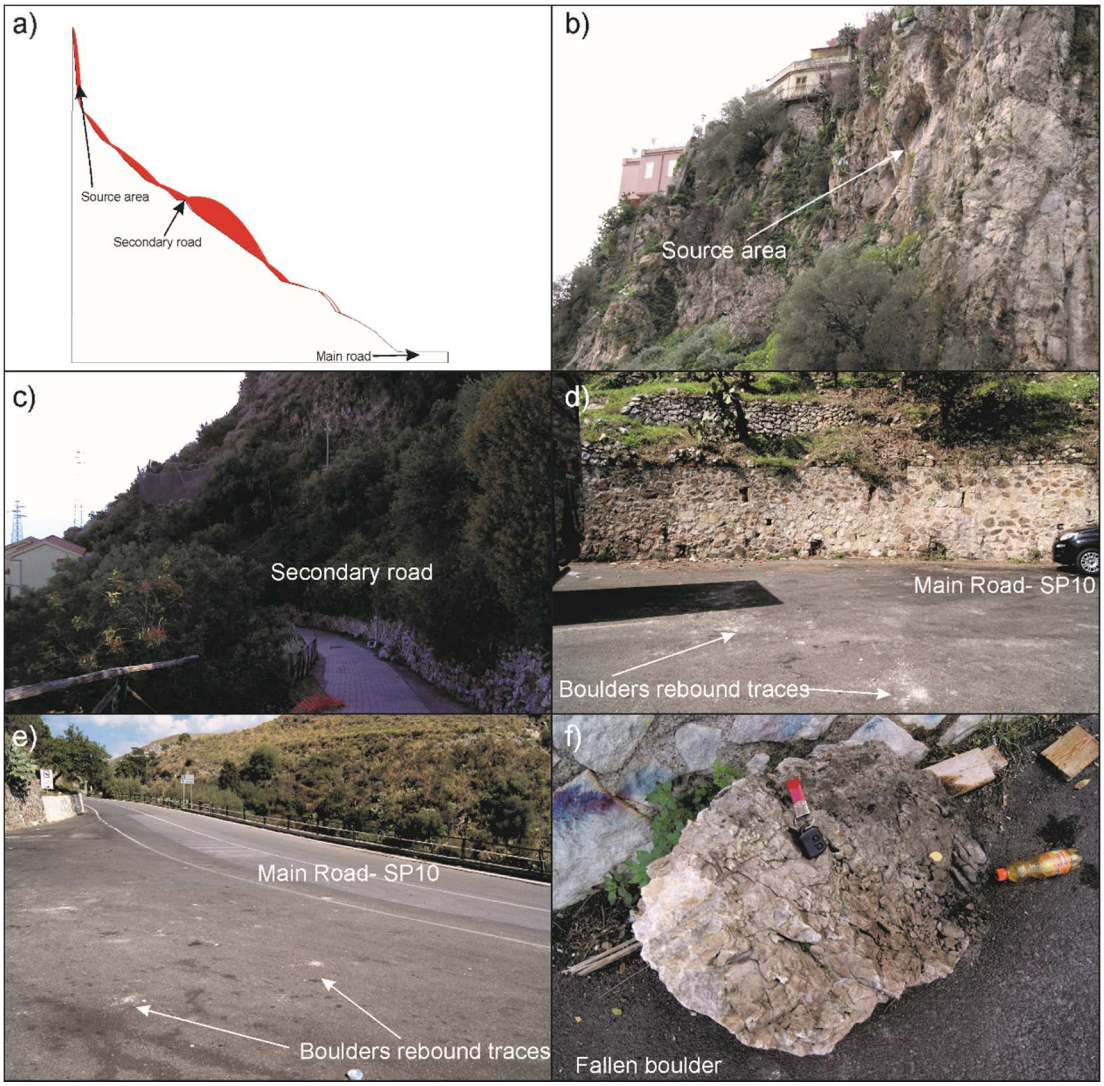

Figure 61: field evidences of the 2014 rockfall at CA: a) bi-dimensional simulation of the trajectory; b) particular of the source area; c) secondary road affected by the transit of falling blocks; d) end point of the boulders on the main road; e) boulders rebound traces; f) one of the fallen blocks on the roadside.

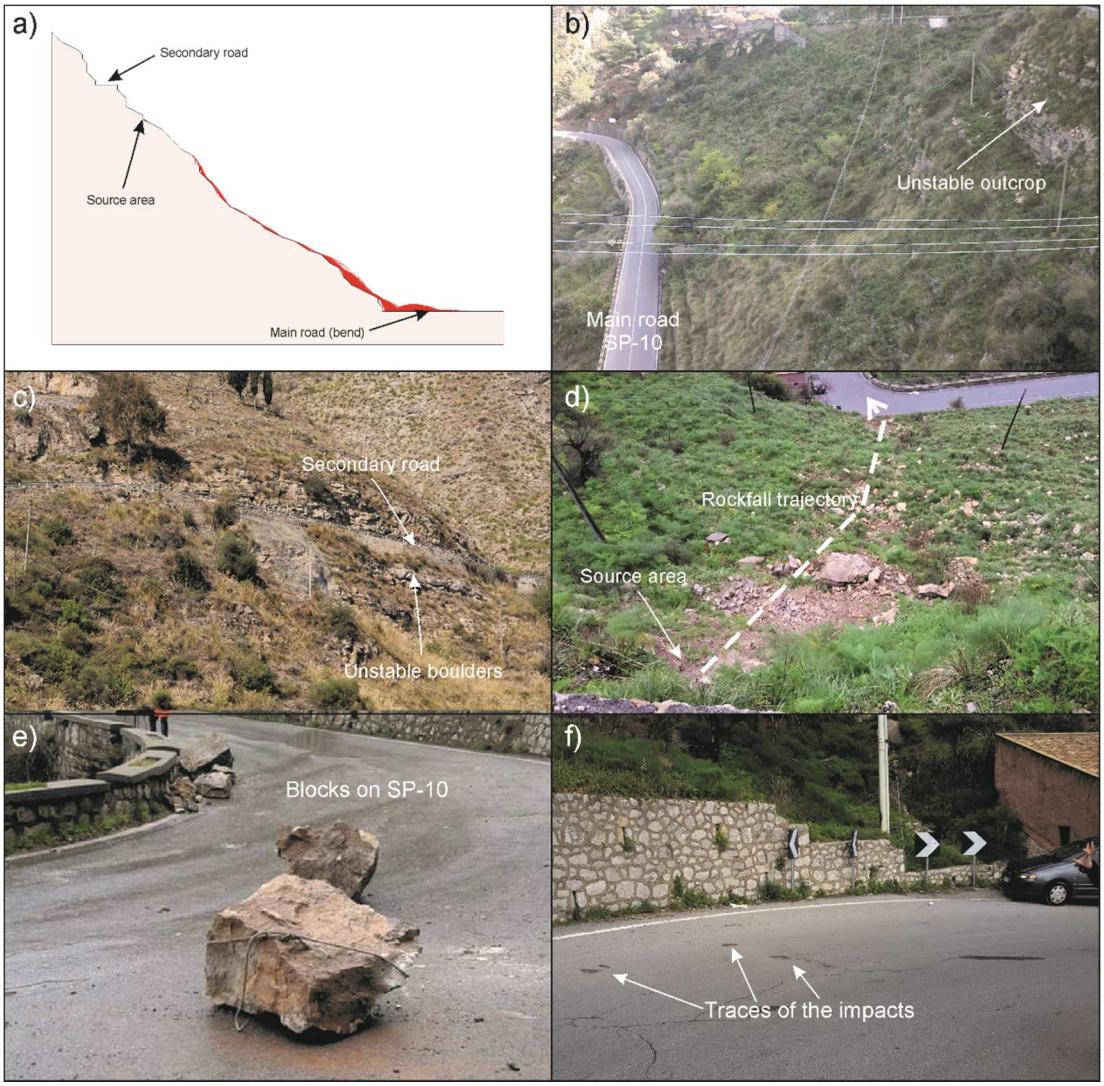

Figure 62: field evidences of the 2015 rockfall at MRA: a) bidimensional simulation of the trajectory; b) particular of the source area impending over the SP-10; c) panoramic view of the unstable boulders; d) traces of the rockfall seen from above; e) boulders stopped on the SP-10; f) Traces of the impacts on the asphalt after the removal of the blocks.

8.3. 2D simulations

For two-dimensional analysis of rockfall trajectories, a computer program operating a "lumped mass" analysis was employed. In particular, the lumped mass engine uses a particle analysis (Hoek, 1987), which is composed of three distinct sections: the particle algorithm, the projectile algorithm, and the sliding algorithm. The particle algorithm makes sure all of the simulation parameters are valid, sets up all of the initial conditions in preparation for the projectile and sliding algorithms and then starts the projectile algorithm.

The projectile algorithm is used to calculate the movement of the rock while it is travelling through the air, bouncing from one point on the slope to another. The sliding algorithm is finally used to calculate the movement of the rock while it is in contact with the slope.

Each rock is assumed as a particle, which may be thought of as an infinitesimal circle, therefore there is no interaction between particles, but only with the slope segments and eventual structures (e.g. rockfall barriers). For this reason, each rock boulder behaves as if it is the only rock acting in the simulation.

Nevertheless, although the size of rock is neglected, this method takes into account the mass of the falling block, which is used to calculate the kinetic energy of the rock. Such value is constant during the whole simulation and, with respect to this study, it was considered according to the fallen boulder surveyed in the study area.

Finally, the slope is modeled as one continuous group of straight line segments, connected end to

end, and no frictional interaction between blocks and air is considered. Therefore, the path of the rock through the air is, because of the force of gravity, a parabola.

For 2D simulations, representative sections were located along the most critical slopes both at CA and MRA, trying to trace the most likely path that a

falling boulder would follow, according to the morphology of the area. In particular, provided sections cross both the upper and the lower segments of SP-10, involving also the secondary roads and the group of houses hit by the 2006 and 2015 rockfalls. 5000 trajectories were simulated for each section and achieved results, with particular reference to “end point” and “kinetic energy” data, were used to create thematic contour maps of the studied areas aimed at graphically showing the spatial variation of such parameters.

8.3.1. 2D simulations at Cliff Area

In this area, detachment points are mostly located at the top of the cliff on which Castelmola village lies. **Figure 63** shows the most representative cross sections taken into account for bidimensional simulations of rockfall trajectories. All sections cross the area from the top of the cliff to the SP-10 road, which is likely to be considered the main element at risk, followed by the group of houses and the secondary road.

The first path of the falling boulders is characterized, in the northern sector, by free-fall along the sub-vertical face of the cliff (e.g. sections A-A',B-B', C-C'); then blocks rebound on rock debris to roll down towards the secondary road, which is reached by almost the totality of the boulders, although some of them are stopped by widespread weeds on the rock debris.

The secondary road acts both as end spot for slower boulders and as rebound point for the others; in particular, these last ones head downstream with a total kinetic energy of about 130 kJ at the rebound points on the secondary road. Along the slope, most of the blocks are then stopped by shrubs, while the others reach the SP-10 road with kinetic energies ranging, on average, between <10 and 50 kJ. Section D-D' is an example of boulders stopping along the slope after having rebounded on the secondary road, while section E-E' shows the worst scenario analyzed herein, i.e. boulders hitting the houses. In this case, the existing rockfall barrier, built in 2006 to protect the houses, was not considered because of its potential inefficiency due to the presence of a thick debris behind it, maybe accumulated due to poor maintenance (the latest blocks bypassed it in 2014). In this case, 100% of simulated blocks would hit the houses with a total kinetic energy up to about 150 kJ. Finally, sections F-F' and G-G' simulate trajectories in the southern sector, where blocks would rebound along the slope and on the secondary road, reaching, in some cases, the SP-10 road.

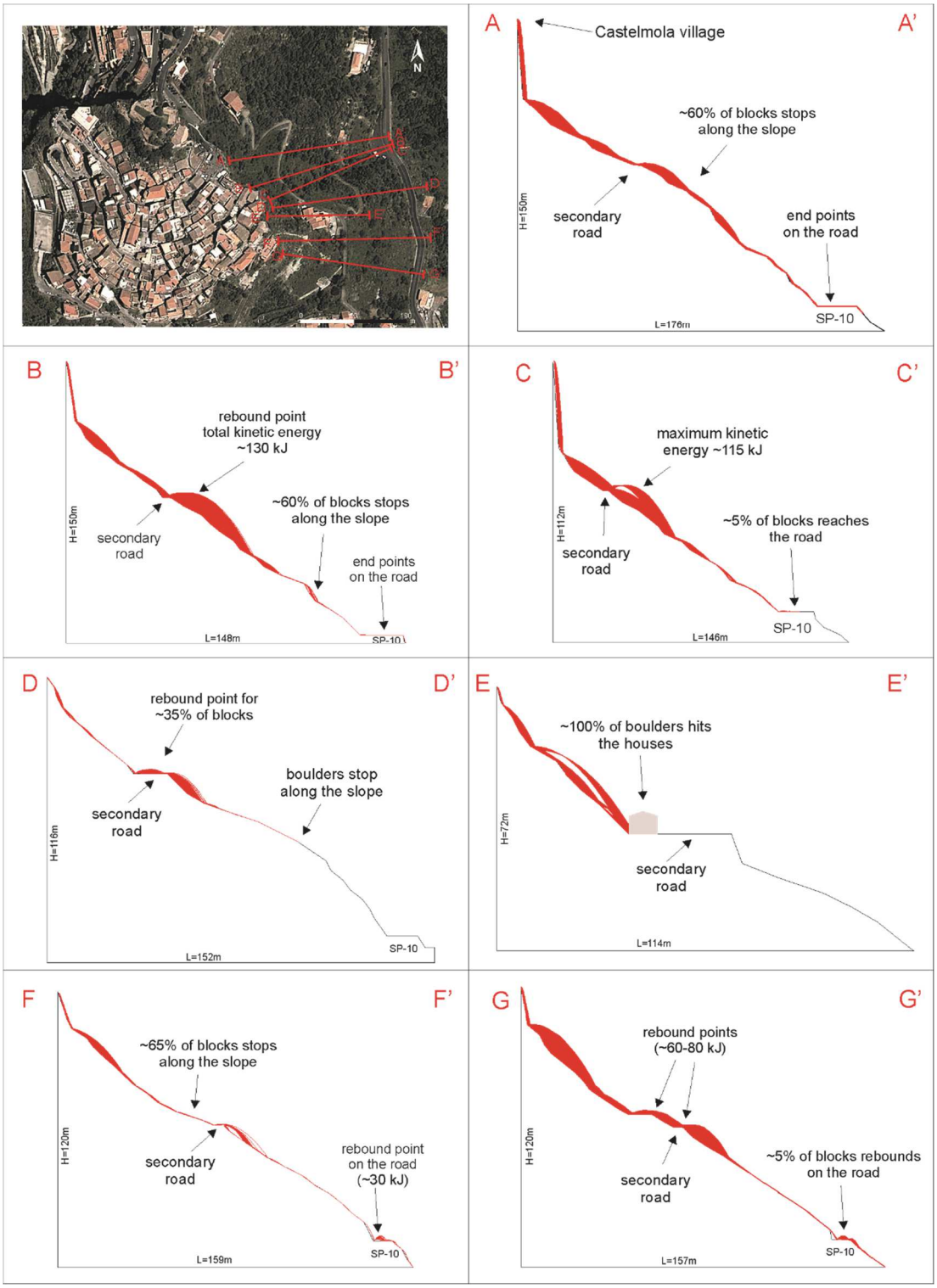

Figure 63: bidimensional simulations of rockfall trajectories along representative cross-sections of CA.

8.3.2. 2D simulations at Main Road Area

At MRA, the closest sector to Castelmola entrance, blocks mainly detach from the high limestone and dolostone outcrops and head downstream through steep slopes, crossing the SP-10 road.

In this sector, the road runs following a winding path, giving rise to two parallel segments at different altitudes. Therefore, from now on, such road portions will be referred to as upper and lower segments, located at about 440 and 410 m of altitude, respectively.

Rockfall trajectories were simulated along sections originating from the highest altitudes, where the unstable outcrops were surveyed, and crossing both segments of SP-10, along with one or more secondary roads at the top of the slopes.

Figure 64 shows the location of cross sections, distinguished by different colors only for an easier reading of the figure. In particular, the northernmost sections are the closest in space to the 2015 rockfall trajectory, whose blocks stopped on the upper segment of SP-10 at the bend (**Figure 62**). Simulations show that 10 to 30% of blocks stops along the upstream slope, before reaching the road. About 10-20% of blocks would stop at the upper segment of SP-10, while the remaining percentage would rebound towards the lower segment, where they can either stop or keep heading downstream. Sections from K-K' to L-L' cross the straightest portions of the main road, usually reached by falling boulders, with average kinetic energies ranging from 80-100 kJ at the upper segment to 130-150 kJ at the lower one. Even the secondary road is affected by the transit of blocks, which stop therein in about 30% of cases.

Sections O-O', P-P' and Q-Q' were located at a bend sector, where unstable porphyroid rock masses impend over the main road. In this case, detached blocks would involve the upper segment of SP-10 in almost 100% of cases; then, according to their energy, they can either stop at the bend (very low

visibility) or proceed downstream, crossing a vegetated slope, which will slow them down until the lower segment of the road is reached. In some cases, blocks would firstly reach the lower segment, with a total kinetic energy of about 30 kJ, to finally proceed downstream. In some other cases, blocks will never reach the downstream segment, stopping along the vegetated slope.

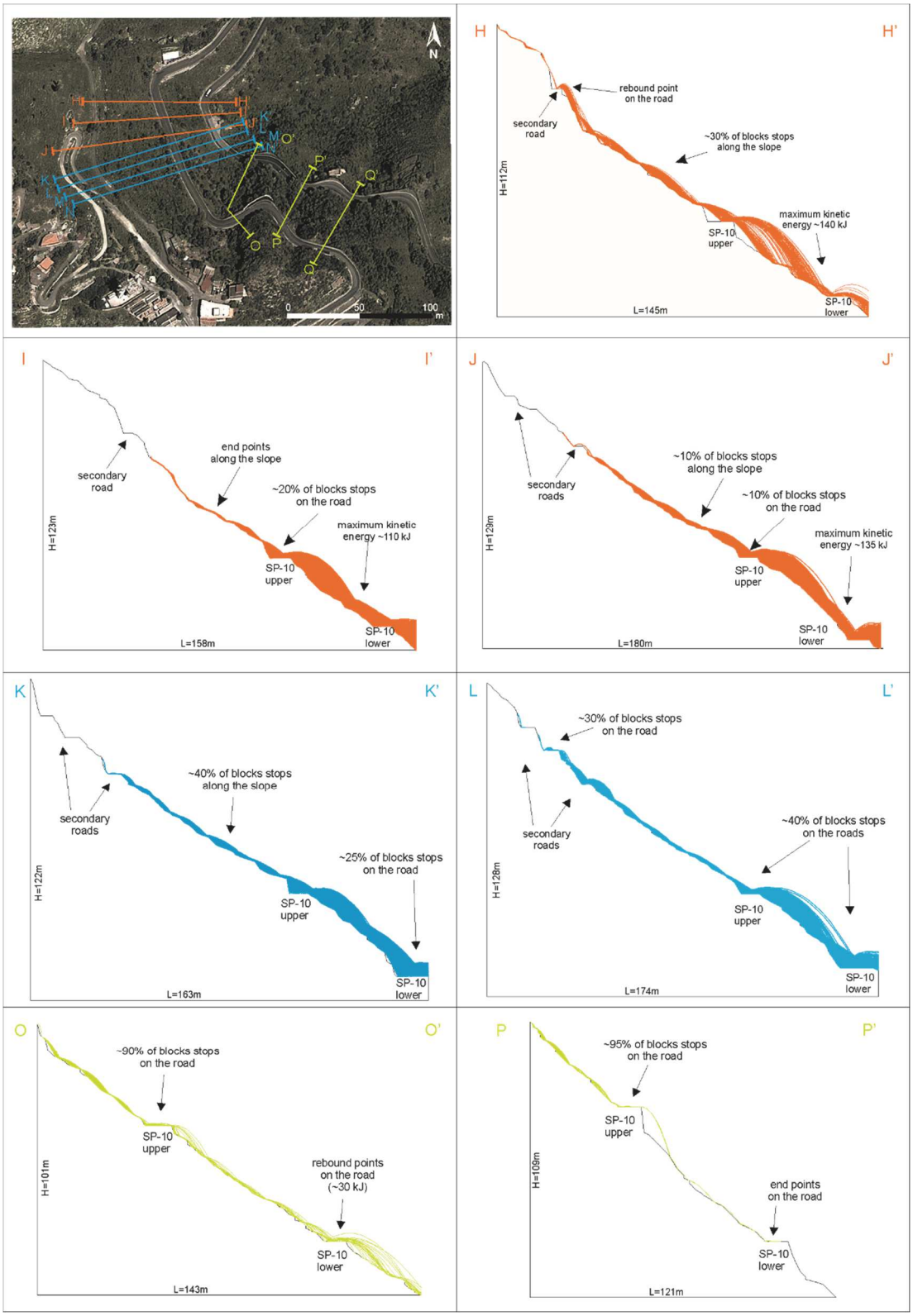

Figure 64: bidimensional simulations of rockfall trajectories along representative cross-sections of MRA.

8.4. Thematic maps

With the aim of representing in a graphical way the spatial distribution of achieved results, thematic maps were drawn by interpolating punctual data retrieved from each 2D section. in particular, the percentage of blocks stopping at peculiar points and the total kinetic energy of falling boulders were taken into account to highlight the most hazardous areas, as well as the extent of the studied issues.

With respect to the first case, maps in **Figure 65** show the concentration of end points related to simulated rockfalls. In particular, interpolated data are referred to the percentage of blocks that stop in a particular point along their route. Therefore, sectors labeled with the highest values are those spots where the maximum percentage of falling blocks would stop. On the other hand, sectors labeled with lower values mainly represent transit areas, where blocks pass (but do not stop) to head downstream.

In this perspective, **Figure 65**a shows the contour maps of end points at CA, where one of the most critical sector is represented by the group of houses, already hit by falling blocks in 2006 and 2014. Here and along the secondary road, most of the blocks would stop, representing a threat for tourists and residents. A further interesting element is the concentration of end point along the incision in the northern sector, which is also a preferential way for blocks to reach the main road. In this case, blocks would stop along this incision in 40 to 90% of cases, due to the presence of shrubs. Nevertheless, there is a rate of blocks reaching the SP-10 road, such as the one triggered in 2014, stopping as far as it.

Finally, another element deserving a comment is the high end-points concentration area in the eastern part of the contour map: here, the presence of rock masses impending over the road, as well as of some unstable blocks

along the slope, leads to relevant possible concentrations of blocks stopping at the main road, possibly affecting also some private houses downstream.

MRA (**Figure 65**b) is characterized by a high percentage of boulders stopping in the northern sector, at the bend already involved in the 2015 event. Here, due to the morphological setting of the road, blocks reaching this point tend to stop rather than heading downstream. Nevertheless, there is a fair percentage of blocks, which reaches the lower segment of the road, sometimes overstepping it.

The middle sector is mainly characterized by transit of blocks heading downstream, due to the steep gradient of the slope. To the south, the metamorphic rock masses impending over the SP-10 road lead to a direct threat to this infrastructure, since the majority of detached blocks would directly reach the road stopping on it.

Based both on the knowledge of the study area, achieved during the field surveys, and on the latest rockfall events, it is possible to affirm that maps provided in **Figure 65** show a reliable datum, since they well match with boulders accumulation spots surveyed in the area.

Similar considerations can be carried on with reference to the kinetic energy of falling blocks. This feature is very important when remedial works are planned and, although this research is not directly focused on the design of protection structures, the distribution of total kinetic energy can be useful to understand the entity of potential rockfalls.

In this perspective, **Figure 66**a shows the distribution of total kinetic energy at CA, where three main high energy areas can be found. In particular, the northernmost area affects a steep sector driving falling boulders along the morphological incision as far as the SP-10 road. Here a progressive decrease of the kinetic energy is caused by the vegetation, slowing down the boulders in the downstream sector before they reach the main road. The second high

concentration area coincides with the group of houses, where blocks would be stopped by the impact with these structures at a relevant kinetic energy. The third area is located in the southern sector of CA, at the initial portion of the simulated rockfalls, where the morphology of the slope allows a progressive acceleration of the block motion. SP-10 road in this sector is labeled with lower energy values because of the presence of vegetation along the final portions of the slopes.

Figure 66b shows that at MRA the highest values of total kinetic energy affect the lower segment of SP-10 road in the northern sector of the area, where the morphology of the slopes allows a progressive acceleration of falling blocks, which gain energy as they proceed downstream. On the other hand, lower energies are found in the southern sector of SP-10 and along the secondary roads, which are suddenly reached by blocks falling from the impending rock masses. Intermediate values label the upper segment of the road, which is the first target of boulders coming from upstream and which acts both as end point and as rebound point enhancing, in the latter case, the rockfall movement.

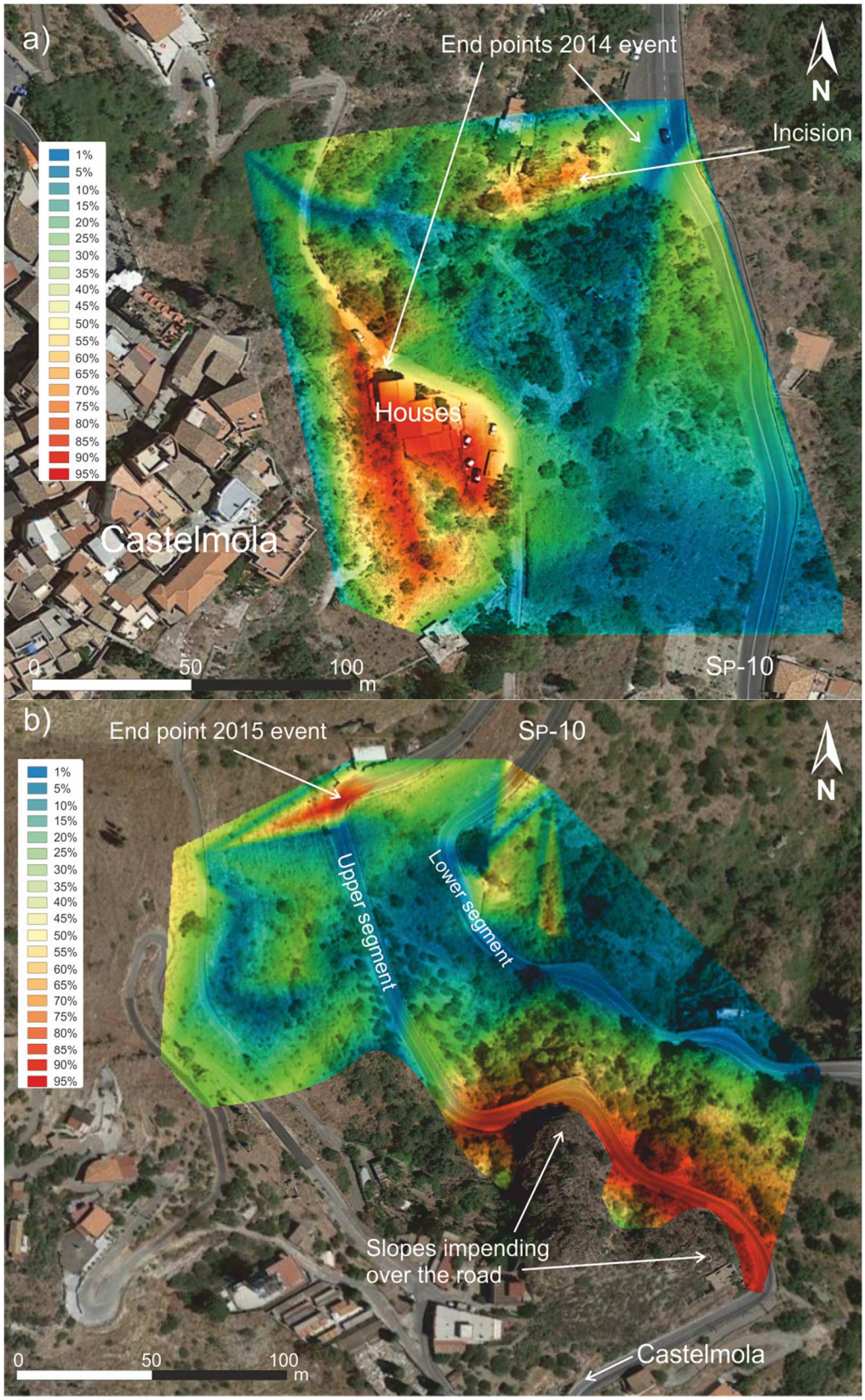

Figure 65: contour maps showing the concentration of end points, according to performed rockfall simulations, for MRA (a) and CA (b).

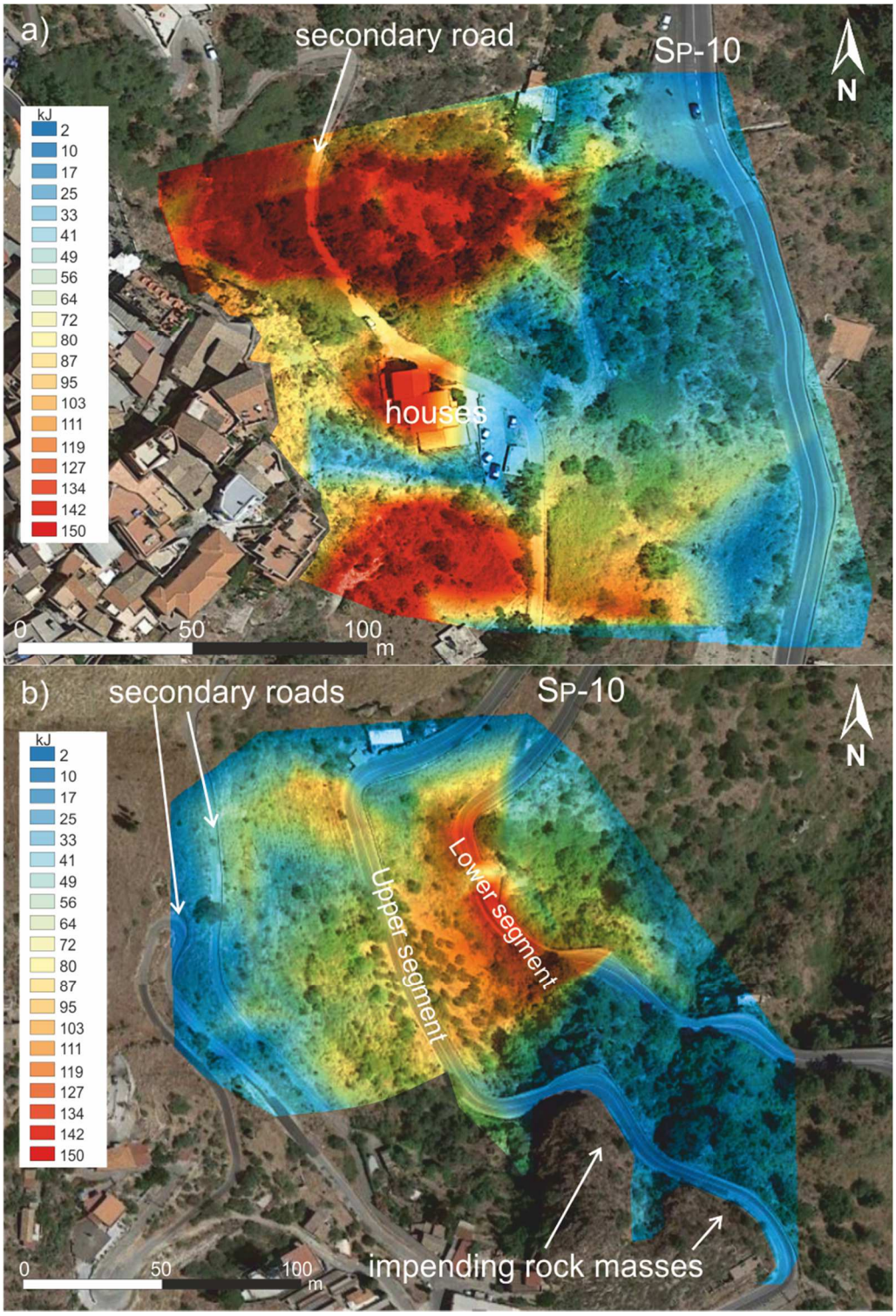

Figure 66: contour maps showing the distribution of total kinetic energy of falling boulders, according to performed rockfall simulations, for MRA (a) and CA (b).

8.5. 3D simulations

Rockfall simulations were carried out also on 3D models of the study area to analyze the behavior of falling boulders according to the real morphology of the slopes. In this case, three-dimensional models of CA and MRA were generated from xyz meshes achieved by processing a Digital Terrain Model (DTM) with a 2m regular grid, providing a good morphological detail.

The models, discretized in homogeneous zones, allowed the analysis of the trajectories by taking into account realistic morphological features of the considered slopes. For this kind of approach, the block is assumed as a sphere rotating around its center of gravity, while its mechanical characteristics are hardness and mass, calibrated according to the boulders fallen in the latest years.

Block is “launched” from a pre-established site and its motion is described by impacts on an elevation attributed plane. This plane is formed by a grid of tridimensional nodes forming a triangular mesh, which represents the entire area between the launch and the stopping points of the blocks.

The value added in such tridimensional approach, if compared to the corresponding 2D models, is the possibility of considering the spatial distribution of the rockfall trajectories, which usually is influenced by the plano-altimetric trend and cannot be modeled on bi-dimensional cross sections.

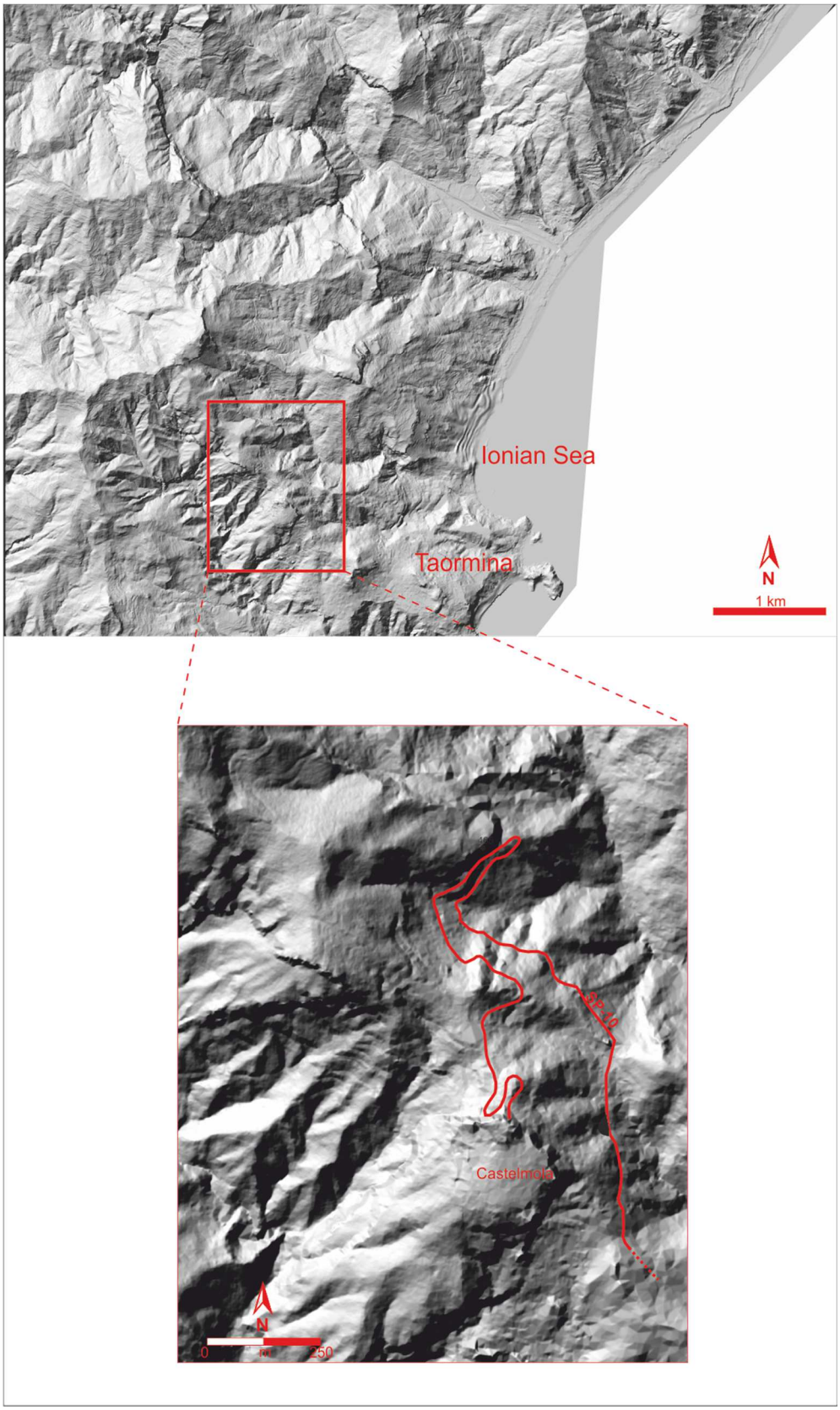

Figure 67: Digital Elevation Model of the study area (property of Regione Siciliana, authorization number 215-B-1160 granted to Simone Mineo on 19 March 2015).

8.5.1. 3D simulations at Cliff Area

CA model comprises one of the most critical sectors of the study area, where the main potential elements at risk are represented by the group of houses involved in the 2015 event along with the SP-10 road and the secondary road connecting Castelmola to Taormina (**Figure 68**a).

Launch sites were set both at the top of the cliff and downstream, where several loosened outcrops are located.

The outcome is a quite realistic model of the possible distribution of rockfall trajectories; in particular, in the northern sector most of the boulders converge in a shallow incision driving them as far as the SP-10 road. Blocks following this route would either stop along the incision, where vegetation is present, or reach the main road at a rest area, invading also the carriageway (**Figure 68**b). This is the case of one of the blocks involved in the 2014 rockfall, whose movement ended on the SP-10 road (**Figure 61**e).

In the middle sector, detached blocks would reach the residential area (point 2 in **Figure 68**b), threatening the public safety.

In the southern sector, blocks can be slowed down by vegetation or stopped by existing rockfall barriers, built in the 2000's; nevertheless, some possible trajectories would affect the downstream complex of houses (point 4 in **Figure 68**b).

Attention was also paid to the eastern sector of the area, by considering some launch sites along the lower slopes, hosting some loosened outcrops. In this case, all the boulders would reach the SP-10 road, threatening some private structures and the main communication route (point 7 in **Figure 68**b).

Achieved results show that the rockfall trajectories are, on the whole, spatially distributed and that SP-10road can be considered the main target of falling boulders, followed by the secondary road and the private houses. The main concentration of block routes is the morphological incision in the northern

sector, which drives falling blocks as far as the main road. Vegetation would play a slowing role in the block movement, as some trajectories end on vegetated areas, although this cannot be considered a reassuring element due to the frequent occurrence of fires baring the slopes, especially in the summer periods (**Figure 69**).

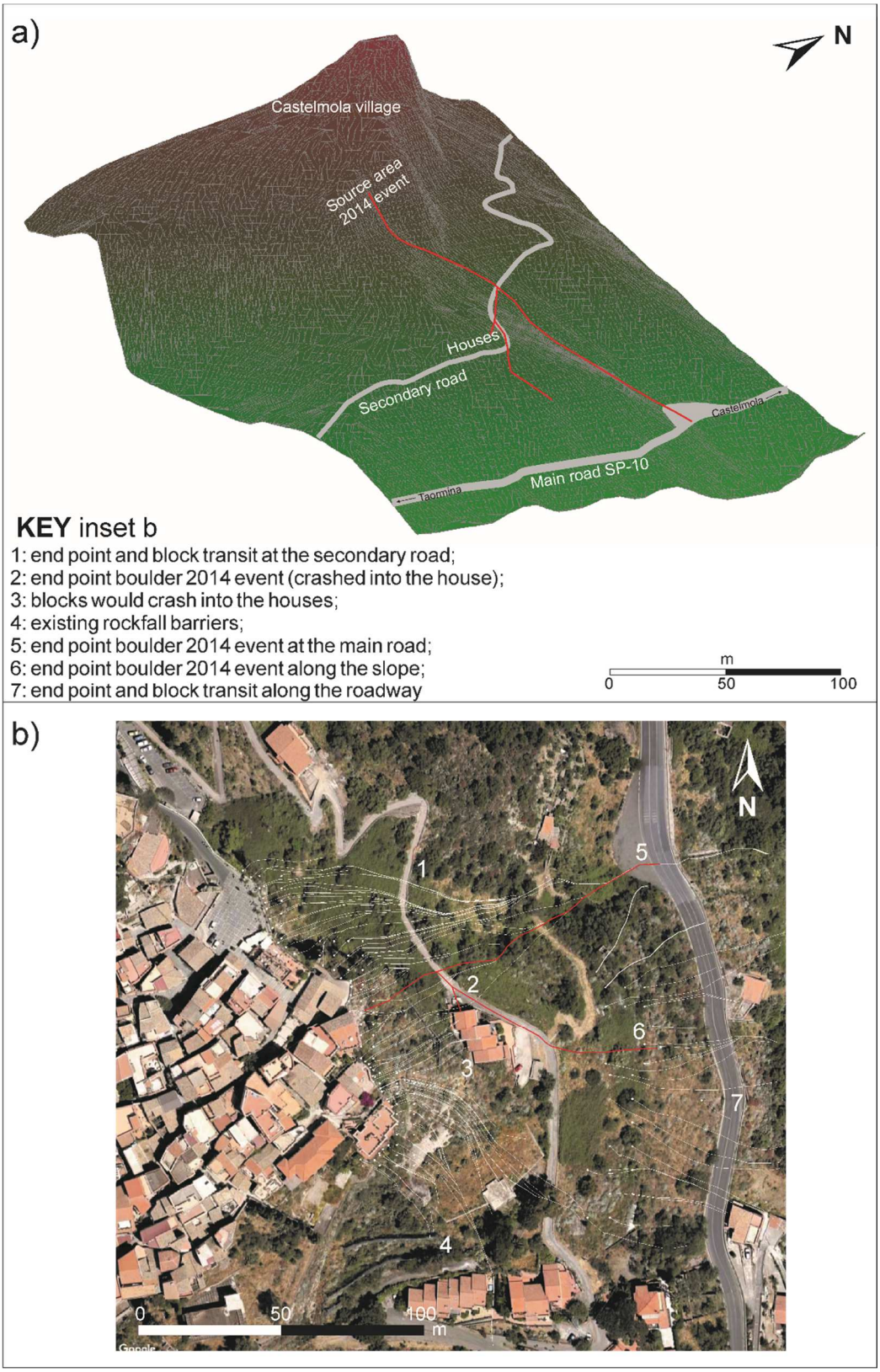

Figure 68: output of 3D simulations at CA. a) 3D model with main elements at risk; b) map of the rockfall trajectory overlapped to an aerial photo of the area. Red trajectories in insets a and b are referred to the 2014 event.

8.5.2. 3D simulations at Main Road Area

MRA trajectories were modeled considering numerous launch points, due to the morphological setting of the area. In fact, from a morphological point of view, it is an important incision representing a receptor for falling boulders, which are likely to cross the road segments regardless of the real source area (**Figure 70**a). In particular, **Figure 70**b shows all the trajectories of rockfalls originating from a zone of loosened limestone and dolostone outcrops (**Figure 62**c-b). Most of the blocks would reach the SP-10 road at its upper segment, where they could either stop (as already occurred in 2015) or rebound to head downstream towards the lower segment. The secondary road would be involved by rock material detached from the highest altitude, while some blocks could end their fall along the slopes. This latter eventuality deserves a critical consideration. In fact, blocks stopped along a slope are kept in a precarious equilibrium between forces by various elements (e.g. the presence of vegetation, another boulder, peculiar morphological conditions). If one of these elements lacked (because of a fire burning the vegetation, or after an earthquake for example), the movement would be susceptible of reactivation. Therefore, most of the blocks laying along the slopes after a fall cannot be considered in safety condition (**Figure 69**a).

For this reason, some of the calculated trajectories are referred to real critical cases of blocks prone to fail and projecting on the road, such as points 6, 12 and 14 reported in **Figure 70** and shown in **Figure 69**.

In particular, three unstable blocks impending over the SP-10 road are highlighted in **Figure 69**a. Such blocks, whose dimension can be easily guessed by comparing them with the passing car immortalized in **Figure 69**a, are one of the most worrying feature of this sector. Moreover, some month after the shooting of the photo in **Figure 69**a, the leftmost block fell down reaching the SP-10 road, fortunately causing no victims (**Figure 69**d)

As for CA, achieved outcomes confirm that in this sector SP-10 and the secondary roads are targets for potential rockfall events, which would involve different segments of the roads threatening the daily traffic. Moreover, 3D models show that while the upper segment is characterized by diffuse points of impact, the lower one is reached at more localized spots. However, such simulations cannot take into account any sudden and unpredictable change in the block trajectory caused by peculiar circumstances, as those which led some blocks bypassing the barriers at CA in 2006.

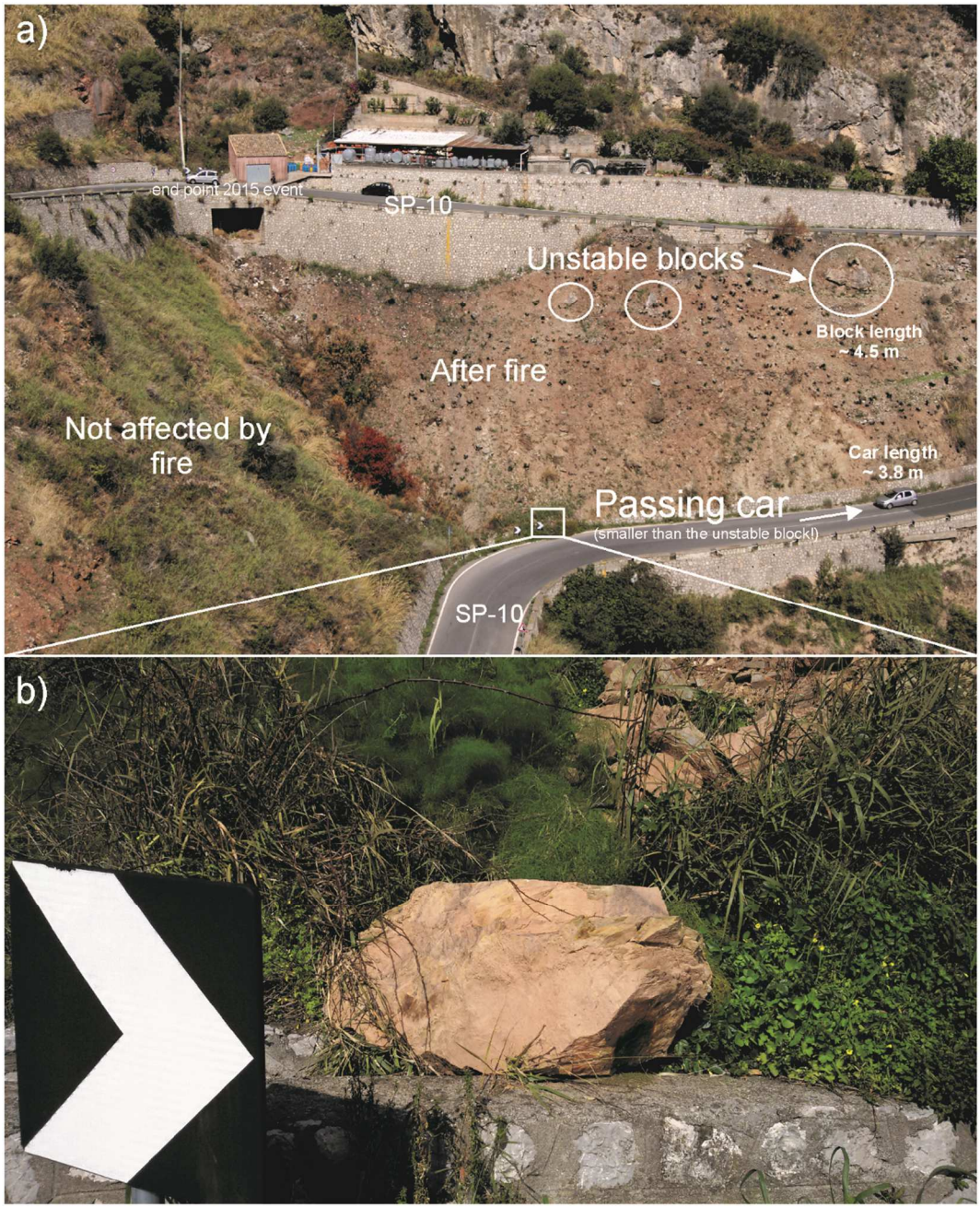

Figure 69: a) panoramic view of MRA after a fire. Three unstable blocks are prone to fail towards the downstream sector of SP-10 road (simulation at point 6 of **Figure 70**b); b) the leftmost block in **Figure 69**a after having been mobilized some month later the shooting of the photo.

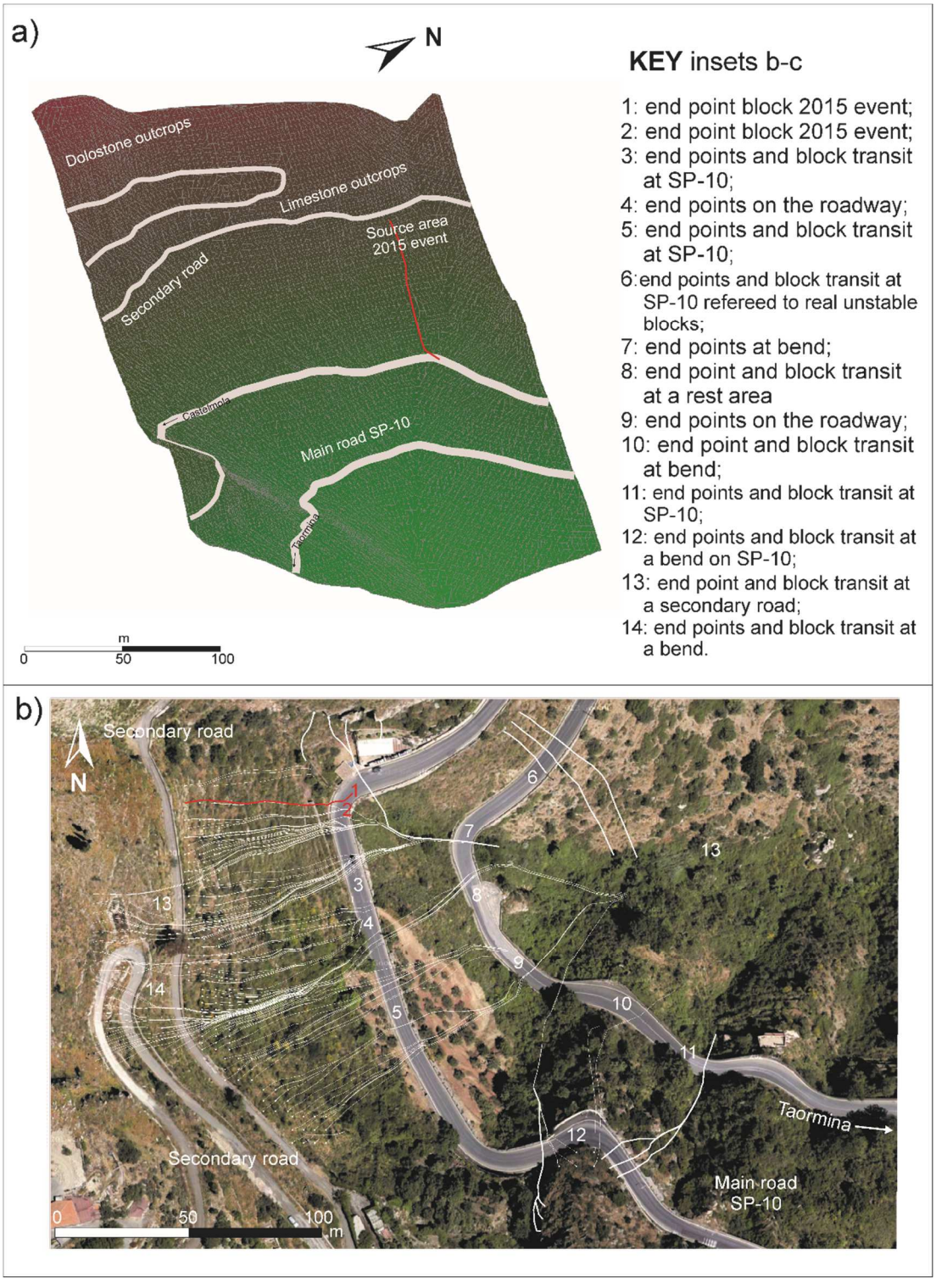

Figure 70: output of 3D simulations at MRA. a) 3D model with main elements at risk; b) map of the rockfall trajectories overlapped to an aerial photo of the area. Red trajectory in insets a and b is referred to the 2015 event.

CHAPTER 9

RISK ASSESSMENT

9.1. Available literature data

Data achieved throughout this research are preparatory to a risk analysis aimed at assessing the probability of injuries, caused by rockfalls, involving the main elements at risk. In this case, the main elements at risk are the group of houses at CA and the SP-10 road running through CA and MRA and connecting Castelmola to Taormina, followed by the secondary roads running within the area.

With respect to MRA, Pappalardo et al. (2014) proposed a preliminary hazard assessment along the SP-10 road, according to the modified Rockfall Hazard Rating System (RHRS) proposed by Budetta et al. (2004) after Pierson et al. (1990). This is a semi-quantitative classification system, developed by the Oregon Department of Transportation (USA), to assess the risk associated with rockfalls (Pierson et al., 1990; National Highway Institute, 1993; Scesi et al., 2001), in order to identify dangerous slopes which require urgent remedial works or further studies. The method was subsequently modified in order to make it more suitable to the geometrical features and to the traffic standards of the Italian roads (Budetta, 2004).

It consists in the assignment of a score to 9 categories concerning the rockfall hazard (i.e. slope height, geologic character, volume of rockfall/block size, climate and presence of water on slope and rockfall history) and the vehicle vulnerability (i.e. ditch effectiveness, average vehicle risk, percent of decision sight distance, roadway width) (**Table 25**). The summation of all the assigned scores assesses the degree of the exposition to the risk along roads. If the RHRS final value is lower than 300, the remedial works on the slope will be considered “with low urgency”; whereas the final score is higher than 500, the slope will need “immediate stabilization works” (Pierson et al., 1990). Slopes

with intermediate scores are considered with "high priority of remedial works", although it would be appropriate a case-by-case evaluation (Budetta, 2004).

According to such procedure, Pappalardo et al. (2014) assessed that SP-10 is a high rockfall hazard road requiring immediate stabilization measures (**Figure 71**).

Table 25: Summary sheet of the modified Rockfall Hazard Rating System (Budetta, 2004).

Category	Rating criteria by score			
	Points 3	Points 9	Points 27	Points 81
Slope height	7.5 m	15 m	22.5 m	> 30 m
Ditch effectiveness	Good catchment: properly designed according to updates of Ritchie's ditch design chart + barriers	Moderate catchment: properly designed according to updates of Ritchie's ditch design chart	Limited catchment: wrongly designed	No catchment
Average vehicle risk (% of time)	25%	50%	75%	100%
Decision sight distance (% of design value)	Adequate (100%)	Moderate (80%)	Limited (60%)	Very limited (40%)
Roadway width	21.5 m	15.50 m	9.50 m	3.50 m
Slope Mass Rating (SMR)	80	40	27	20
Block size	30 cm	60 cm	90 cm	120 cm
Boulder volume	26 dm^3	0.21 m^3	0.73 m^3	1.74 m^3
Volume of rockfall per event	2.3 m^3	4.6 m^3	6.9 m^3	9.2 m^3
Annual rainfall and freezing periods	h=300 mm or no freezing periods	h=600 mm or short freezing periods	h=900 mm or long freezing periods	h=1200 mm or long freezing periods
Rockfall frequency	1 per 10 years	3 per year	6 per year	9 per year

Pappalardo and Mineo (2015) carried out a rockfall risk assessment at CA, taking into account the risk related to the presence of the houses according to the modified Rockfall Hazard Rating System (RHRS) by Saroglou et al. (2012). This method, similar to the previous one, is based on the calculation of rockfall risk of natural and man-made slopes and encompasses all those parameters, which are considered important for this purpose. It defines twenty rating parameters, grouped in four major categories according to the hazard and consequences, with a different weight in the assessment of the total risk are considered (**Table 26**).

Pappalardo and Mineo (2015) assessed for CA a risk ranging from Medium (risk class III) to High (risk class IV) (**Figure 72**). The highest risk was detected in

correspondence of the group of houses, already threatened by the 2006 and 2014 main events, while intermediate values (between classes III and IV) are found in areas with "low human activity" and absence of houses.

Nevertheless, Pappalardo and Mineo (2015) did not consider the SP-10 road, which now can be acknowledged among the most crucial elements at risk of CA sector, because they applied a method focused on natural slopes and not on infrastructures.

Therefore, with the aim of providing an alternative numerical risk assessment focused on the main transportation corridor, updated and supported by the new data achieved in this study, this section reports on the risk computation through the "Event Tree Analysis" (ETA) method (e.g. Peila and Guardini, 2008; Budetta et al., 2016). The great breakthrough of this approach is the possibility of customizing the Event Tree, by calibrating it according to the peculiar features of the study area (i.e. route of the road, trajectory simulations, probability of accident).

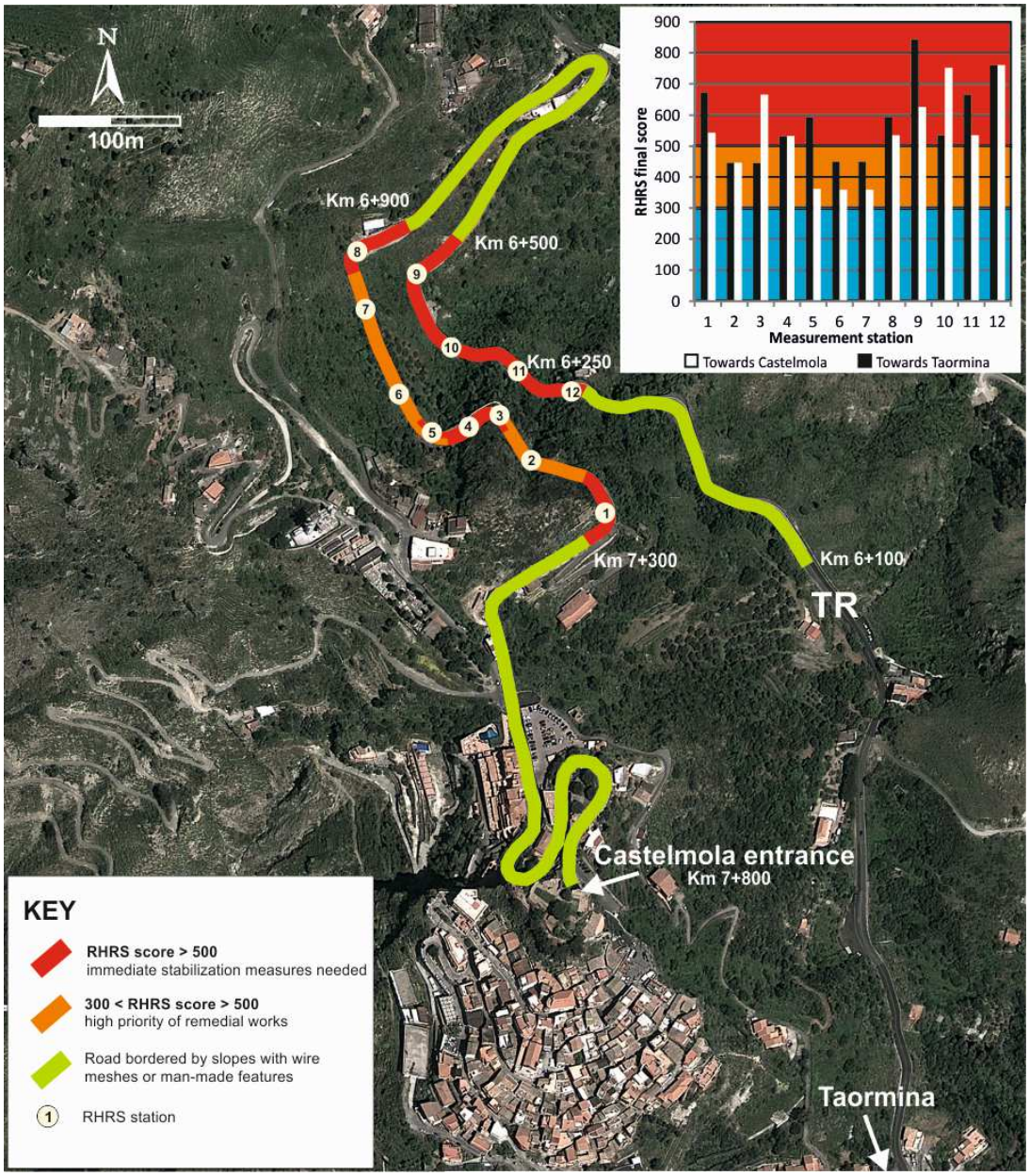

Figure 71: modified RHRS applied to a segment of the SP-10 road (Pappalardo et al., 2014).

Table 26: Parameters of all categories and rating of proposed rockfall rating system for natural rock slopes to define risk. (Saroglou et al., 2012).

Parameter	Category/ parameter weight factor	Rating					Score (Multiply rating with weight factor of parameter)
1. Slope angle (^{0})	A/7 %	25–40	Medium 40–50	High 50–60		Very high >60 Overhanging	
Rating		10	30	60		100	
2. Slope height (m)	A/4 %	<15	15–30	30–60		>60	
Rating		10	30	60		100	
3. Release area height (H is total height of slope)	A/7 %	Rockfalls from low slope areas (H/4)	Rockfalls from middle slope areas (H/2)	Rockfalls from middle to upper slope areas (3H/2)		Rockfalls from whole slope (H)	
Rating		10	30	60		100	
4. Slope roughness	A/3 %	Rough, planar, (friction reduces acceleration)	Planar smooth (helps acceleration)	Rough, presence of narrow benches, (helps bouncing)		Very rough, presence of narrow benches	
Rating		10	30	60		100	
5. Vegetation of slope	A/4 %	Dense vegetation, occurrence of high trees	Low raised vegetation, bushes	Sparse vegetation		No vegetation	
Rating		10	30	60		100	
int roughness / Filling material in joints/ Joint Opening	B/6 %	Rough, stepped	Smooth, stepped	Undulating or filling material with angular fragments independent of roughness or moderate opening of joints 2.5 to 10 mm	Slightly rough planar or filling with stiff clay >5 mm independent of roughness or very wide opening of joints 10–100 mm	Smooth planar or filling soft clay >5 mm independent of roughness or extremely wide opening > 100mm	
Rating		10	15	30	60	100	
7. Joint Orientation (or combination of joints)	B/5 %	Favorable for stability		Moderate	Adverse	Very adverse	
Rating		10		30	60	100	
8. Joint Persistence (m)	B/4 %	Very low <1m	Low 1–2 m	Moderate 2–5 m	High 5–10 m	Very high >10 m	
Rating		10	15	30	60	100	
9. Joint compressive strength (JCS, MPa, affects friction on joints)	B/1 %	>30	20–30	5–20		<5, weathered	
Rating		10	30	60		100	
10. Strength of intact rock (MPa, helps splitting of falling blocks if strength is low Facilitates bouncing if strength is high)	B/1 %	<10	10–30	30–60		>60 MPa	
Rating		10	30	60		100	
11. Rock mass blockiness / Block volume (m^3)	B/4 %	<1	1–2.5	2.5–4.0	4.0–8.0	>8.0	
Rating		10	15	30	60	100	
12. Estimated number of blocks (for the width of slope under assessment)	B/2 %	Null	1–5	5–10		>10	
Rating		10	30	60		100	
13. Karstic features	B/2 %	No karst	Sparse	Moderate undermined conditions		Frequent Undermined conditions	
Rating		10	30	60		100	
14. Rainfall conditions and intensity	C/3 %	Seldom	Sparsely	seasonal	often	Very often, during whole year	
Rating		10	15	30	60	100	
15. Permeability/ Condition of slope drainage	C/3 %	Very high	High	Moderate	Low	Very low	
Rating		10	15	30	60	100	

Table 26: continued (Saroglou et al., 2012).

Parameter	Category/ parameter weight factor	Rating					Score (Multiply rating with weight factor of parameter)
16. Seismic hazard (acceleration coefficient α)	C/4 %	$\alpha < 0.16$	$0.16 < \alpha < 0.24$	$0.24 < \alpha < 0.36$	$\alpha > 0.36$		
Rating		10	30	60	100		
17. Width of catchment zone (m)	D/10 %	>20	10–20	5–10	2–5	No	
Rating		10	15	30	60	100	
18. Rockfall history	D/5 %	Null to few	Occasional	Numerous	Often	Continuous	
Rating		10	15	30	60	100	
19. Slope accessibility	D/5 %	All types of stabilization possible	Most types of stabilization possible	A number of types of stabilization possible	Few types of stabilization possible	Access very difficult	
Rating		10	15	30	60	100	
20. Potential result of impact and value of structures	D/20 %	Negligible; no human structures and permanent activities	Low; areas of little human activity	Moderate human presence; low frequency of houses	High; frequent human presence, numerous houses	Very high, constant human presence, densely inhabited areas	
Rating		10	15	30	60	100	
Total Score (Maximum 100)							

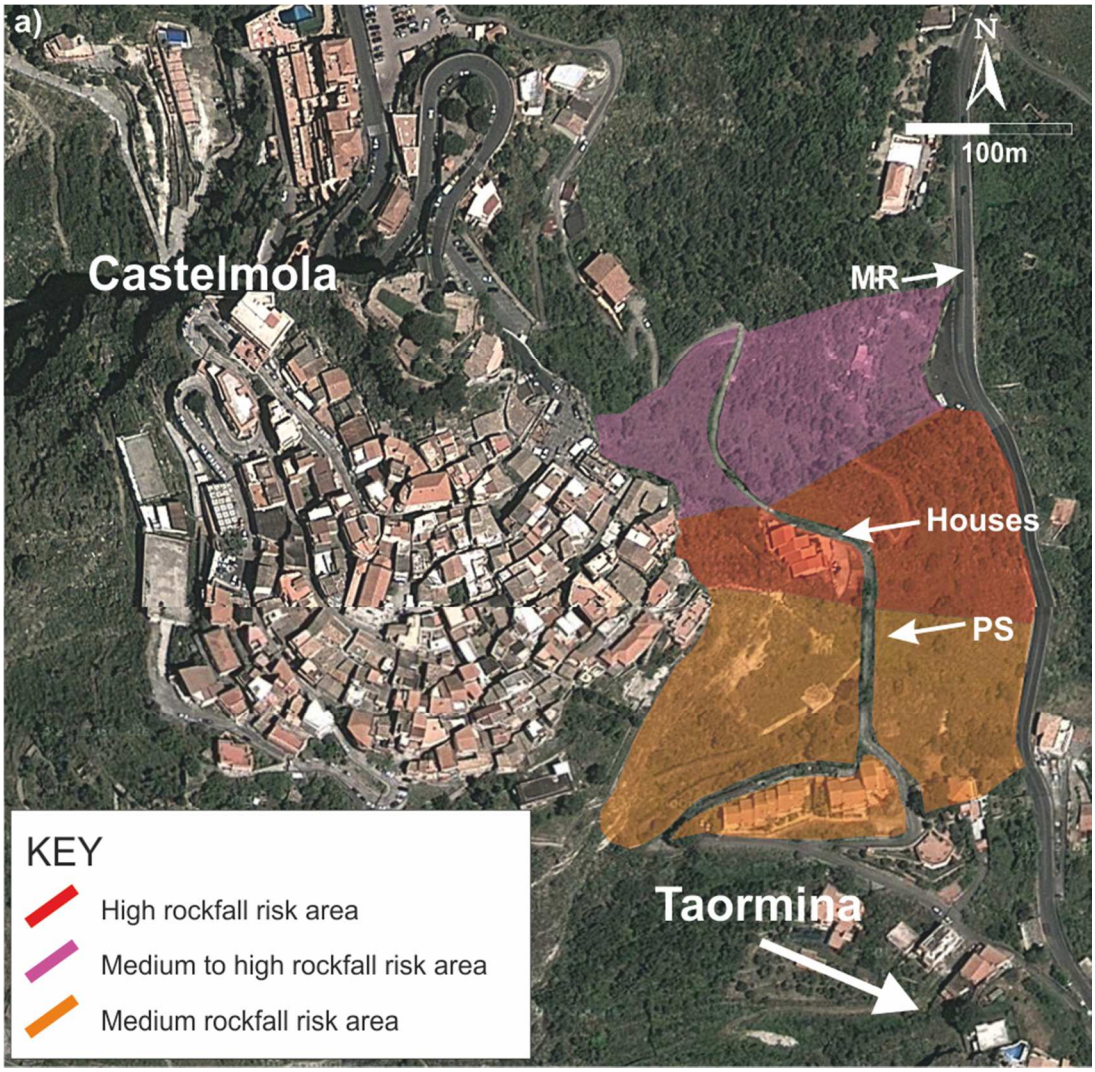

Figure 72: modified RHRS applied to some natural slopes at Castelmola Cliff (modified after Pappalardo and Mineo, 2015).

9.2. Risk definition

Risk is the expression of the likelihood and impact of an uncertain, sudden and extreme event which, if it occurs, may impact positively (opportunity) or negatively (threat) on the achievement of a project or program objective (UNESCO, 2010). The word *risk* is used frequently and in several different contests, from the financial to the medical ones, from the environment to the engineering ones, and so on.

With particular reference to the topic of this research, risk is defined as the probability that a rockfall will cause a certain kind of damage to one or more elements at risk (modified after Ball and Watt, 2001).

According to UNESCO (1972) *disaster Risk* is function of *Hazard, Vulnerability* and *Exposure* (**Figure 73**), where *Hazard* is defined as *a dangerous phenomenon, substance, human activity or condition that may cause loss of life, injury or other health impacts, property damage, loss of livelihoods and services, social and economic disruption, or environmental damage*; *Vulnerability* involves *the characteristics and circumstances of a community, system or asset that make it susceptible to the damaging effects of a hazard; Exposure* refers to *people, property, systems, or other elements present in hazard zones that are thereby subject to potential losses.*

In other words, rockfall risk results from the occurrence of a rockfall event (Hazard) where people or assets in harm's way are present (Exposure) with a lack of preparedness (Vulnerability).

In recent years, the term *Hazard* was eclipsed with the term *Risk*, due to the flexibility of the English language (Lee and Jones, 2014), leading to a conceptual similarity between the two words. In reality, *Hazard* and *Risk* are complementary but distinct, with hazard focusing on the causes of harm or loss and risk focusing on the consequences. For hazard to exist, situations have to arise where humans and goods can be adversely affected. For example, a

landslide on an uninhabited island is not hazard. Similarly, a landslide involving a busy road is acknowledged among the hazards and produces also a risk.

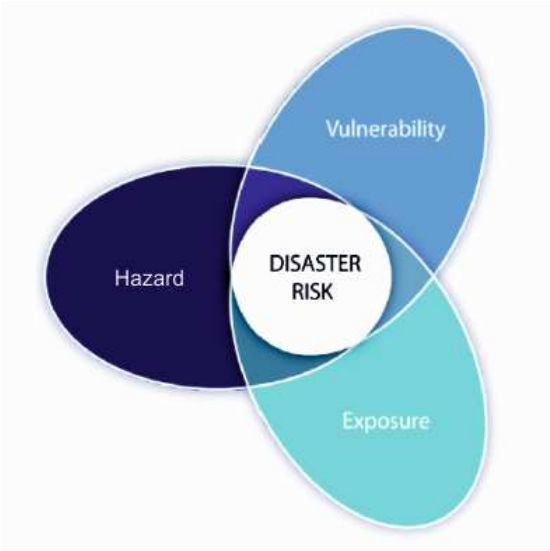

Figure 73: sketch on the three components of disaster risk.

9.3. The Event Tree Analysis

Event Tree Analysis (ETA) was developed in the 1960's as a form of decision analysis in the nuclear industry. The value of decision trees is that they provide a graphical insight to the way particular consequences might arise and can be used as a template for probability assessment (Lee and Jones, 2014). There is a long tradition of use of trees in the assessment of dam safety (e.g. Hartford and Baecher, 2004), and they have proved valuable in analyzing landslide risk, both on natural and engineered slopes (e.g. Bunce et al., 1997; Ho and Ko, 2009; Hoek, 2000; Hsi and Fell, 2005; Lacasse and Nadim, 2008; Lee and Moore, 2007, Peila and Guardini, 2008). The advantage of ETA quantitative risk assessment methodology is the possibility of personalizing the trees, adapting them to the faced problems by creating specific patterns for each analysis and considered elements at risk.

Event trees are typically organized left-right, and comprises the following elements:

1) The occurrence of an initiating event, such as a rockfall or a triggering event.
2) Branches mapping out all the alternative pathways that could develop following the initiating event.
3) Nodes acting as transitions from one position along a pathway to one or more alternative pathways. Typically, the nodes define binary (Yes/No) alternative pathways.
4) Terminal points (leaves), at the end of the braces, defining a unique end-state that is conditional on the preceding event.

The pathway options at each node should be collectively exhaustive; therefore, the sum of the probabilities of moving along any of the pathway options at a node will equal 1, according to equation 13:

$$P(A) + P(A') = 1 \quad \text{(eq. 13)}$$

where P(A) is, for example, the probability that a rockfall occurs, while P(A') is the probability that a rockfall does not occur.

Each terminal point represents an outcome (T), whose probability of occurrence will be the conditional probability of all the nodes along the pathway, starting with the initiating event, as shown by equation 14:

$$P(T) = P(A)\,P(B)\,P(C) \quad \text{(eq. 14)}$$

i.e. the product of the probabilities at each node.

Each outcome, with particular reference to this research, represents a possible scenario in case of rockfall with a positive epilogue (e.g. no damage) or a negative perspective (e.g. accident or damage). The total probability of a particular group of outcomes (e.g. *accident* in this case) will be the sum of the

probabilities related to each terminal point, since these events are mutually exclusive (equation 15).

$$P(accident) = P(T1) + P(T6) \quad \text{(eq. 15)}$$

Where P(T1) and P(T6) are the probabilities corresponding at the outcomes labeled as *accident*.

9.4. Customizing ETA for the Castelmola case study

Defining a unique tree model for the study area is not possible due to the different paths followed by the SP-10 road, which is almost straightaway at CA, while it is winding and divided into upper and lower segment at MRA. With reference to this latter sector, performed simulations highlighted that both segments, running almost parallel, are targets for blocks falling from upstream. Therefore, for the application of ETA method, different statistical conditions (e.g. percentage of impacting blocks and number of rocks) must be taken into account to differentiate the two segments.

In this perspective, ETA was applied to 23 sub-segments of the studied road chosen according to peculiar features of the road (e.g. change in direction at bends) or of the slopes (e.g. surveyed unstable blocks), as reported in **Figure 75**.

At MRA, where the main source areas are located at the upstream rock masses, the evolution of rockfalls at LW is function of the behavior of rocks impacting on UP, which can stop (thus representing no threat for LW) or rebound (representing a rockfall event for LW).

The Event Tree starts with the occurrence of a rockfall, which leads to two possible scenarios, according to the the rockfall trajectory simulations reported at section 8:

- P1: the falling boulder stops along the slope, before reaching the road, thus causing no damage (outcome n#1). In this case, the probability associated to this outcome equals P1. Such case includes also the amount of blocks possibly stopping at the secondary roads.
- P1': complementary to P1, is the probability that the falling boulder reaches the SP-10 road.

This latter scenario leads to further branches:

- P2: the falling block reaching the road hits a vehicle passing through that point in that moment.
- P2': the falling block reaching the road does not hit any passing vehicle.

For P2 to occur, a spatial and temporal correspondence between falling rock and passing vehicle must be verified. The probability associated to this step is therefore assessed according to eq. 16:

$$P2 = P(A)_v \cdot N_{v/a} \quad \text{(eq. 16)}$$

where $P(A)_v$ is the probability that a generic vehicle is hit by a rock and $N_{v/a}$ is the number of vehicles travelling on the road per year.

In this perspective, $P(A)_v$ is calculated following the equation 17

$$P(A)_v = P(S)P(T|S) \qquad \text{(eq. 17)}$$

where P(S) is the probability of spatial correspondence between the rock and the vehicle and P(T|S) is the probability of temporal correspondence between the rock and the vehicle.

P(S) is calculated according to eq. 18

$$P(S) = 1 - (1 - P(S|H))^{Nr} \qquad \text{(eq. 18)}$$

where Nr is the number of rockfall events per year that hit the road (herein assumed between 3 and 1) and P(S|H) is constant probability of rock detachment along the considered portion of road, simplified as the ratio between the vehicle length (Lv) and the slope length (Lp), according to equation 19.

$$P(S|H) = \frac{Lv}{Lp} \qquad \text{(eq. 19)}$$

P(T|S), above defined as the probability of temporal correspondence between the falling block and a passing vehicle, can be assumed equal to the part of the year occupied by a single passing of the vehicle through the section (eq. 20), where Vv is the vehicle speed.

$$P(T|S) = \frac{Lp}{Vv}/8760 \text{ (eq. 20)}$$

In this way, P2 eventuality leads to a negative outcome herein referred to as "accident". This is outcome #2 and its probability of occurrence results from the product of P1'and P2.

It has to be underlined that such probability refers to a generic probability of accident, without considering the possibility that the accident can be fatal (circumstance that would reduce the final probability value). For this computation a traffic volume of 2500 vehicles per day has been considered, according to Pappalardo et al. (2014).

On the other hand, if P2' is verified, two more branches can be added to the tree:

- P3, if the falling block reaching the road rebounds on the carriageway and heads downstream towards the lower segment of SP-10. This

probability is strictly related to the outcomes of the rockfall simulations above commented. In this case, a probability of damage on the road (outcome #3) can be assessed according to eq. 14 and the probability computation restarts from the beginning of the tree. In this case, the number of rockfall will be reduced, with respect to the one considered at the upper segment, according to P3 probability value.

- P3', if the fallen block stops along the road. In this perspective, a passing vehicle could either hit the boulder laying on the road (P4), due to peculiar condition of visibility of the road itself, or not hit the block (P4').

P4 will therefore be labeled as "accident" (outcome#4), while P4' would lead to a possible damage on the road (outcome #5).

P4 can be assessed according to Bunce et al. (1997), as it is linked to the possibility that the driver can see the block on the road and has the time to avoid the impact by changing trajectory or stopping the car. To evaluate this probability, it is necessary to introduce the Decision Sight Distance (DSD) parameter, which represents the length of road a driver needs in order to make a complex or instantaneous decision (Budetta et al., 2014). This parameter, linked to the type of road and to the speed of the car, can be calculated according to Ferrari and Giannini (1975) and CNR (1980) as the distance within which a 15 cm high stationary object is continuously visible from 1.10m above the road (i.e. the height of a driver's eye on the road). DSD is critical when obstacles on the road are difficult to perceive, or when unexpected or unusual maneuvers are required (Budetta et al., 2014). It is assumed that an accident will occur if the rockfall is within half of the DSD of the vehicle (Bunce et al., 1997).

P4 value, i.e. the annual probability of a vehicle crashing onto a rock on the road, can be therefore calculated according to equation 21 (after Lambert and Nicot, 2011).

$$P4 = 1 - (1 - P(S|H)')^{Nr} \qquad \text{(eq. 21)}$$

where, P(S|H)' is the probability of a vehicle crushing onto a rock on the road, according to Lambert and Nicot (2011).

Once calculated P4, P4' value can be computed for percentage difference. Even in this case, this probability is not specifically referred to a fatal accident, but to a generic accident event.

Finally, the total probability of each outcome is calculated backwards by multiplying the probability values at each node; then, the sum of outcomes 2 and 4 will be the total probability of *accident* in case of rockfall, the sum of outcomes 3 and 5 will be the overall probability of *damage* in case of rockfall, and outcome 1 is the probability of *no damage*.

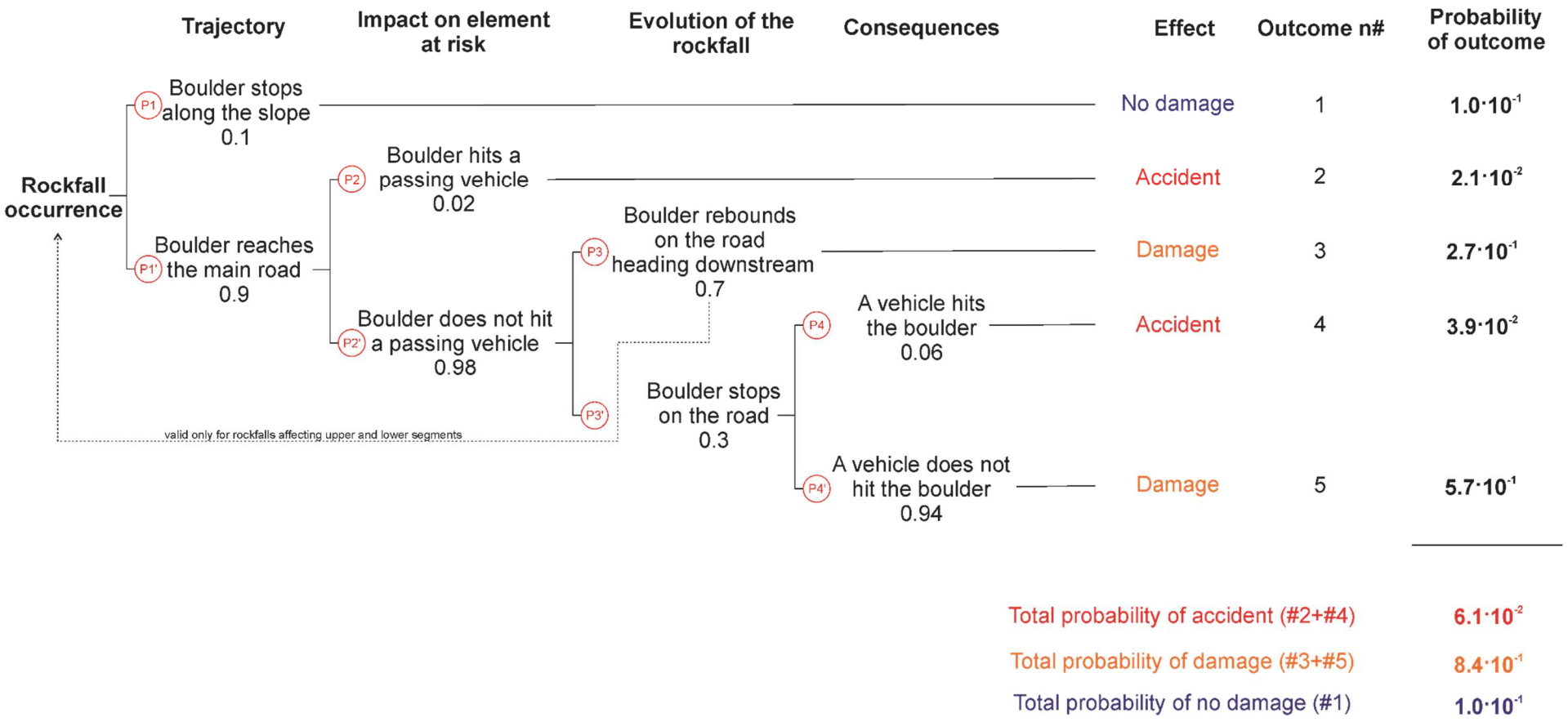

Figure 74: an example of Event Tree properly designed for the S16 sub-segment.

9.5. Results of risk analysis

According to the schemes proposed in the previous sections, the application of ETA led to the computation of the following three main values:

1) probability of *accident* in case of rockfall: probability that a falling block may cause an accident to a passing vehicle, due either to a direct impact during the fall or to a crash of a vehicle into a boulder laying on the carriageway;
2) probability of *damage* in case of rockfall: probability that a falling boulders reaching the road may cause damages to the infrastructure (e.g. asphalt, retaining walls, guard rail) during their transit or stop. In this case the word "damage" refers also to possible economic damages due to potential road disruption periods.
3) probability of *no damage* in case of rockfall: probability that a falling boulder may cause no damages to the road or passing vehicle because it stops along the upstream slope, before reaching its targets.

In this perspective, the probability of accident represents the worst scenario, because it involves the presence of people, regardless of the epilogue of the event (unharmed, injured or dead), while the probability of damage is related only to economic loss due to the disruption of the road and to remedial works. Results reported in **Table 27** show that the road is affected by a different probability zonation according to its path and to the analysis herein carried out.

The probability of accident, considering the sum of outcomes 2 and 4, ranges between $7.1 \cdot 10^{-3}$ and $8.4 \cdot 10^{-2}$, with an average value of $3.2 \cdot 10^{-2}$ (**Figure 75**). Such values are in accordance with literature data concerning, for example, the risk of fatal car accident in Campania (although in this research the assessed probability is not related only to fatal accident), which was assessed equal to $3.41 \cdot 10^{-2}$ (Budetta et al., 2016 and references therein). Highest values are

found at the upper segment of the road at MRA, which can be considered the first target of falling boulders. The highest probability of accident was detected at bend sectors and where rock masses impend over the road. The lower segment is characterized by a lower probability of accident, since the number of rocks reaching the road is reduced by the "protecting" effect of the upper segment. CA has the lowest values, due to the aerial distance of the road from the source areas located at the top of the cliff, and to the stop of several boulders along the slopes. Therefore, only a small percentage of blocks is likely to reach the road, although it is a reliable datum as confirmed by the latest rockfall events occurred in 2006 and 2013.

On the other hand, the probability that a falling boulder could reach the road in case of rockfall is definitely higher, as shown by **Figure 76**. This takes into account the sum of outcomes 3 and 5, which are related to the probability that a rock stops along the road or rebounds on it. In this case it would cause damages, meant as either road disruption, or material damage at road portions, or economic loss due to remedial measures. The average probability of damage is $6.4 \cdot 10^{-1}$, with maximum values mainly affecting UP and some portions of LW, where loosened rock slopes impend over the road and where the road acts as a receptor for falling blocks. In both cases, blocks would stop along this transportation corridor, leading to potential accidents and/or to road disruption. CA is characterized by lower values because of the aforesaid reasons; nevertheless in this sector the road is not the only target for falling boulders at CA. In fact, as already shown in the maps reported in **Figure 65** and **Figure 66**, also the secondary road and the group of houses are threatened by rockfalls and most of the blocks stops before reaching the road. ETA, as provided herein, is specifically designed for the risk assessment along important infrastructures, therefore it cannot take into account the risk for houses and secondary roads, but Pappalardo and Mineo (2015) already

highlighted the high risk affecting these natural slopes, with particular reference to the inhabited houses. Results clearly show the critical condition of the area, as documented during the numerous surveys carried out during this research.

Table 27: probability according to the performed ETA.

Sub-segment	Outcome n#							
	1	2	3	4	5	P accident	P damage	P no dam.
S1	$8.0\cdot10^{-1}$	$4.3\cdot10^{-3}$	$1.5\cdot10^{-1}$	$2.8\cdot10^{-3}$	$4.6\cdot10^{-2}$	$7.1\cdot10^{-3}$	$1.9\cdot10^{-1}$	$8.0\cdot10^{-1}$
S2	$3.0\cdot10^{-1}$	$7.0\cdot10^{-3}$	$5.2\cdot10^{-1}$	$4.4\cdot10^{-3}$	$1.7\cdot10^{-1}$	$1.1\cdot10^{-2}$	$6.9\cdot10^{-1}$	$3.0\cdot10^{-1}$
S3	$6.0\cdot10^{-1}$	$6.7\cdot10^{-3}$	$3.4\cdot10^{-2}$	$1.5\cdot10^{-2}$	$3.4\cdot10^{-1}$	$2.2\cdot10^{-2}$	$3.8\cdot10^{-1}$	$6.0\cdot10^{-1}$
S4	$6.0\cdot10^{-1}$	$6.6\cdot10^{-3}$	$1.6\cdot10^{-1}$	$1.0\cdot10^{-2}$	$2.3\cdot10^{-1}$	$1.7\cdot10^{-2}$	$3.8\cdot10^{-1}$	$6.0\cdot10^{-1}$
S5	$2.0\cdot10^{-1}$	$9.1\cdot10^{-3}$	$3.2\cdot10^{-1}$	$1.4\cdot10^{-2}$	$4.6\cdot10^{-1}$	$2.3\cdot10^{-2}$	$7.8\cdot10^{-1}$	$2.0\cdot10^{-1}$
S6	$4.0\cdot10^{-1}$	$9.1\cdot10^{-3}$	$2.4\cdot10^{-1}$	$1.4\cdot10^{-2}$	$3.0\cdot10^{-1}$	$2.3\cdot10^{-2}$	$5.8\cdot10^{-1}$	$4.0\cdot10^{-1}$
S7	$4.0\cdot10^{-1}$	$8.9\cdot10^{-3}$	$2.4\cdot10^{-1}$	$14\cdot10^{-2}$	$3.4\cdot10^{-1}$	$2.3\cdot10^{-2}$	$5.8\cdot10^{-1}$	$4.0\cdot10^{-1}$
S8	$4.0\cdot10^{-1}$	$8.6\cdot10^{-3}$	$2.4\cdot10^{-1}$	$1.3\cdot10^{-2}$	$3.4\cdot10^{-1}$	$2.2\cdot10^{-2}$	$5.8\cdot10^{-1}$	$4.0\cdot10^{-1}$
S9	$4.0\cdot10^{-1}$	$8.6\cdot10^{-3}$	$2.9\cdot10^{-1}$	$1.1\cdot10^{-2}$	$2.8\cdot10^{-1}$	$1.9\cdot10^{-2}$	$5.8\cdot10^{-1}$	$4.0\cdot10^{-1}$
S10	$4.0\cdot10^{-1}$	$9.4\cdot10^{-3}$	$4.2\cdot10^{-1}$	$6.9\cdot10^{-3}$	$1.6\cdot10^{-1}$	$1.6\cdot10^{-2}$	$5.9\cdot10^{-1}$	$4.0\cdot10^{-1}$
S11	$4.0\cdot10^{-1}$	$9.3\cdot10^{-3}$	$4.2\cdot10^{-1}$	$6.9\cdot10^{-3}$	$1.6\cdot10^{-1}$	$1.6\cdot10^{-2}$	$5.8\cdot10^{-1}$	$4.0\cdot10^{-1}$
S12	$2.4\cdot10^{-1}$	$2.4\cdot10^{-2}$	$6.9\cdot10^{-1}$	$3.6\cdot10^{-3}$	$3.5\cdot10^{-2}$	$2.7\cdot10^{-2}$	$7.3\cdot10^{-1}$	$2.4\cdot10^{-1}$
S13	$2.4\cdot10^{-1}$	$1.9\cdot10^{-2}$	$7.0\cdot10^{-1}$	$2.7\cdot10^{-3}$	$3.6\cdot10^{-2}$	$2.2\cdot10^{-2}$	$7.4\cdot10^{-1}$	$2.4\cdot10^{-1}$
S14	$4.0\cdot10^{-1}$	$9.3\cdot10^{-3}$	$4.1\cdot10^{-1}$	$7.2\cdot10^{-3}$	$1.7\cdot10^{-1}$	$1.7\cdot10^{-2}$	$5.8\cdot10^{-1}$	$4.0\cdot10^{-1}$
S15	$4.0\cdot10^{-1}$	$1.0\cdot10^{-2}$	$7.4\cdot10^{-2}$	$2.2\cdot10^{-2}$	$4.9\cdot10^{-1}$	$3.3\cdot10^{-2}$	$5.7\cdot10^{-1}$	$4.0\cdot10^{-1}$
S16	$1.0\cdot10^{-1}$	$2.1\cdot10^{-2}$	$2.6\cdot10^{-1}$	$3.9\cdot10^{-2}$	$5.7\cdot10^{-1}$	$6.1\cdot10^{-2}$	$8.4\cdot10^{-1}$	$1.0\cdot10^{-1}$
S17	$2.0\cdot10^{-2}$	$2.3\cdot10^{-2}$	$9.6\cdot10^{-2}$	$6.0\cdot10^{-2}$	$8.0\cdot10^{-1}$	$8.4\cdot10^{-2}$	$8.9\cdot10^{-1}$	$2.0\cdot10^{-2}$
S18	$2.8\cdot10^{-1}$	$2.0\cdot10^{-2}$	$5.9\cdot10^{-1}$	$8.6\cdot10^{-3}$	$1.0\cdot10^{-1}$	$2.9\cdot10^{-2}$	$6.9\cdot10^{-1}$	$2.8\cdot10^{-1}$
S19	$2.0\cdot10^{-1}$	$2.5\cdot10^{-2}$	$5.4\cdot10^{-1}$	$1.9\cdot10^{-2}$	$2.1\cdot10^{-1}$	$4.5\cdot10^{-2}$	$7.5\cdot10^{-1}$	$2.0\cdot10^{-1}$
S20	$2.0\cdot10^{-1}$	$1.7\cdot10^{-2}$	$7.8\cdot10^{-2}$	$4.0\cdot10^{-2}$	$6.6\cdot10^{-1}$	$5.8\cdot10^{-2}$	$7.4\cdot10^{-1}$	$2.0\cdot10^{-1}$
S21	$2.0\cdot10^{-1}$	$1.7\cdot10^{-2}$	$7.8\cdot10^{-2}$	$4.0\cdot10^{-2}$	$6.7\cdot10^{-1}$	$5.8\cdot10^{-2}$	$7.4\cdot10^{-1}$	$2.0\cdot10^{-1}$
S22	$2.0\cdot10^{-1}$	$1.7\cdot10^{-2}$	$1.6\cdot10^{-2}$	$4.4\cdot10^{-2}$	$7.2\cdot10^{-1}$	$6.2\cdot10^{-2}$	$7.4\cdot10^{-1}$	$2.0\cdot10^{-1}$
S23	$2.0\cdot10^{-1}$	$9.0\cdot10^{-3}$	$3.9\cdot10^{-2}$	$2.2\cdot10^{-2}$	$7.3\cdot10^{-1}$	$3.1\cdot10^{-2}$	$7.7\cdot10^{-1}$	$2.0\cdot10^{-1}$

Figure 75: Map showing the distribution of the probability of accident in case of rockfall (Outcomes #2+#4 of the event tree). The acronym "n.a." is for road segments where risk could not be assessed because of man-made structures or peculiar local setting.

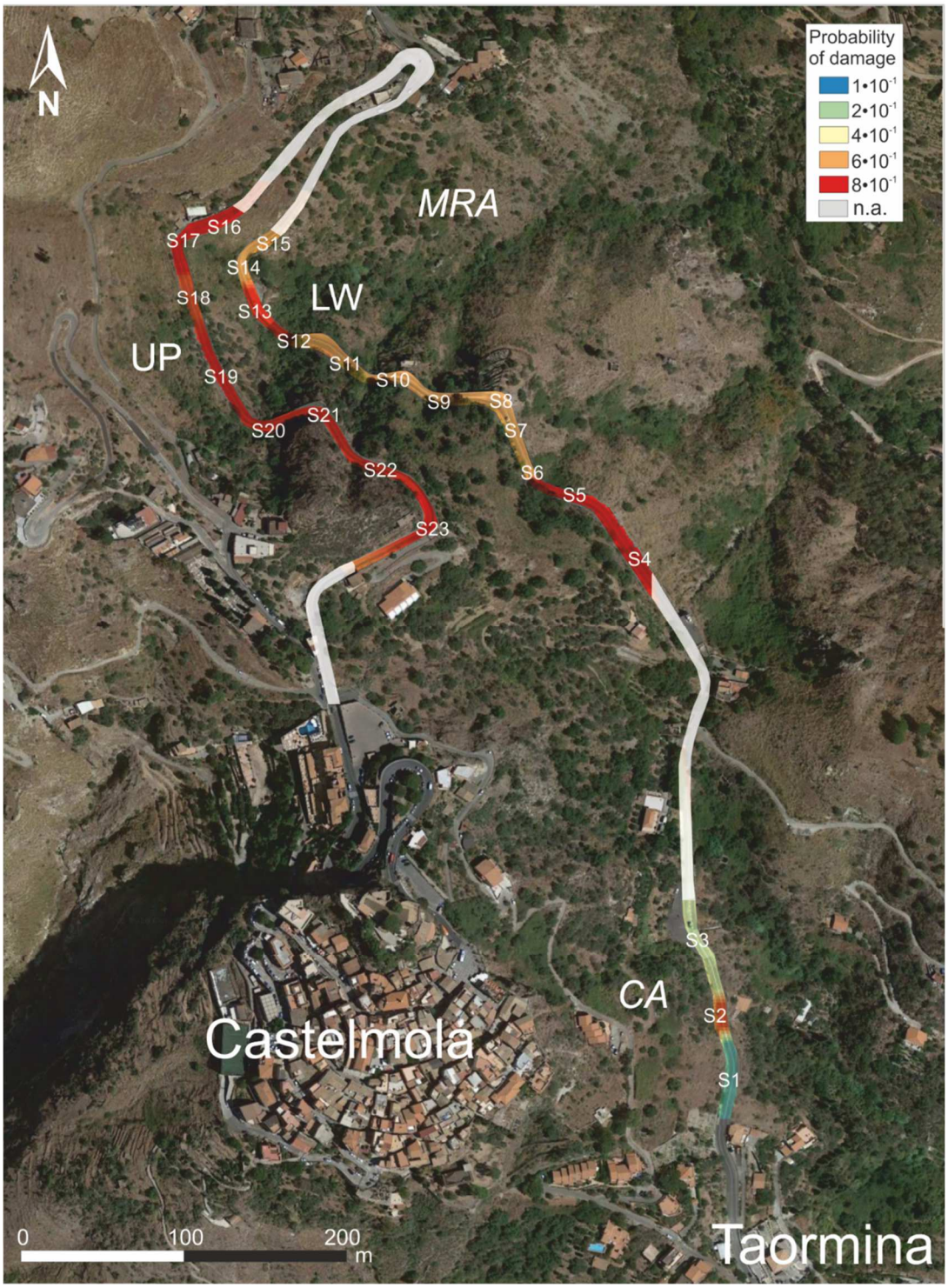

Figure 76: Map showing the distribution of the probability of damage in case of rockfall (Outcomes #3+#5 of the event tree). The acronym "n.a." is for road segments where risk could not be assessed because of man-made structures or peculiar local setting.

9.6. Comparison between ETA and RHRS methods

Results achieved herein through ETA, with particular reference to the risk assessed at MRA, can be now compared to recent literature data, concerning the application of the modified RHRS (after Budetta et al., 2004) to a segment of MRA.

Although such two methods cannot be directly compared, because they are based on different principles (the definition of a score for RHRS and the estimation of probability for ETA), a short comment on the relative outcomes is appropriate.

As aforesaid, Pappalardo et al. (2014) assessed that SP-10 is a high rockfall hazard road requiring immediate stabilization measures, highlighting that the highest risk can be found at bend portions, characterized by considerable changes in the Decision Sight Distance parameter.

On the other hand, the maps provided herein and achieved through a quantitative risk assessment approach allows highlighting a different zonation of the same road segment, with respect to the probability of accident, and a more uniform risk distribution in case of considering the whole probability of damage.

Both products agree in labeling the upper SP-10 with intermediate-high risk, with particular reference to the bend sectors, where RHRS considers a reduction of the DSD parameter due to lowered visibility condition. ETA approach, which is based also on trajectory simulation data, highlights that along the upper segment of the road there is a segment affected by a higher probability of accident or damage, due to the higher percentage of boulder potentially stopping on the road.

The main difference between the two outcomes is in the lower segment, which on one hand is labeled as high risk sector by the modified RHRS and, on the other hand, shows a lower probability of accident than UP according to the

quantitative ETA applied herein. This is because, RHRS, which is a semi-quantitative method, does not take into account the peculiar route of the road and the probability that falling boulders may stop before reaching the lower segment, but only the slope height. This is a key consideration because, although such methodologies are not really comparable, ETA proved a more versatile method for this kind of analysis because it can be customized for the studied road path. On the contrary, a strong limitation of ETA is that it is conditioned by the subjectivity of the operator. In fact, results can greatly change based on the number of rockfall considered and on the interpretation of the rockfall trajectory simulations.

CHAPTER 10

LATEST EVOLUTION OF THE EVENTS

After a scientific study, it is a good practice verifying all the achieved data with the aim of validating the proposed models.

With particular reference to the scientific issue discussed herein, dealing with rockfalls and associated risk means studying the predisposition of a territory to landslide, mainly based on the local geological and geomechanical settings and on field evidences. Sometimes, if such studies are carried out after the occurrence of a phenomenon, this can be back-studied to be used as reference for the calibration of the models.

Nevertheless, verifying the reliability of such studies is a hard practice, because rockfall is a noticeable event, which usually causes a relevant risk for the population; therefore it is desirable not to happen, especially in populated areas.

Contrariwise to this statement, on 16 November 2016, when this study was almost completed and all data had already been elaborated, a further event was triggered by heavy rainfalls at CA. Two blocks of about 0.3 m^3 detached from the top of the cliff, reaching the secondary road, few meters away from the houses (**Figure 77**a-b). Both blocks stopped on the secondary road, although the largest one wobbled at the edge of the road, prompting the rescue team to remove it in order to avoid a further fall downstream.

The end points of such blocks is located in a high-concentration area, according to the model designed herein (**Figure 77**c), underlying the reliability of proposed data and the actual risk associated also to secondary elements of this area.

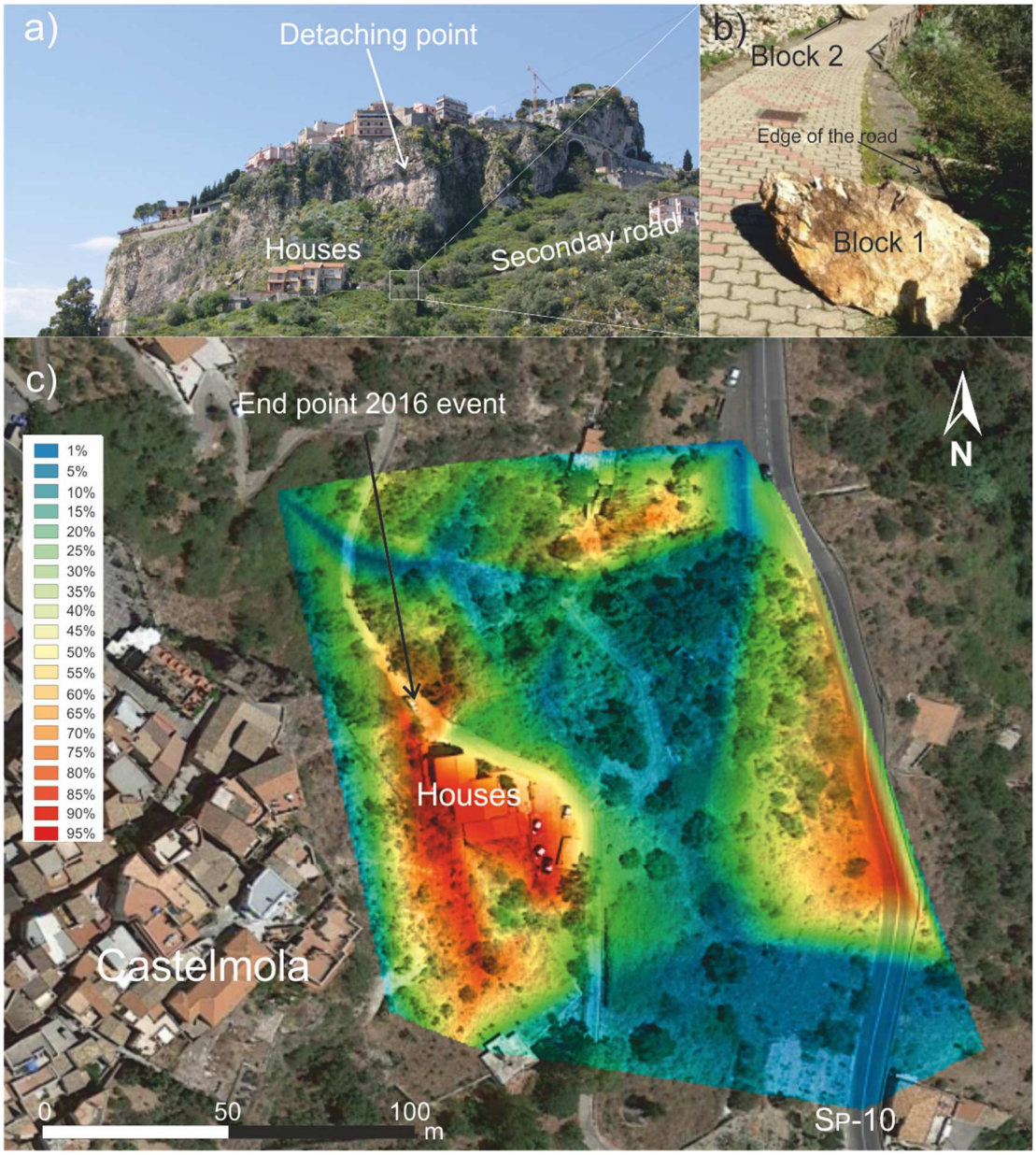

Figure 77: rockfall occurred on 16 November 2016. a) view of the cliff, b) particular of fallen boulders, c) end-points concentration map already reported in **Figure 65**, with location of the end point of this event.

CHAPTER 11

DISCUSSION

11.1. Risk assessment along the SP-10 Road

The research presented herein, focused on an approach for the quantitative rockfall risk assessment along strategic transportation corridors, highlighted how complex and diversified this kind of study is. The followed procedure, customized for the specific setting of the application area, was applied as example to a strategic road of northeastern Sicily (SP-10), which is the only communication route between the cities of Taormina and Castelmola. This road has already been the target of falling blocks during the latest years, although numerous events have never been documented.

Rock masses, surveyed herein both by in situ measurements and by InfraRed Thermography shooting campaigns, are heavily fractured and show a poor geomechanical quality, due to the complex geological history of the area, and are affected by several unstable kinematic patterns, which can be regarded as potential future events.

In particular, occurred rockfalls were usually characterized by the detachment of rock volumes up to metric size (**Figure 61**, **Figure 62**), which can be made of either a single boulder or a set of small blocks, cemented by calcite filling the less persistent discontinuities (especially for the carbonate lithologies), forming a unique boulder. Once detached, such blocks cross the slopes as far as the road, which can be hit at different segments. Therefore, numerous trajectory simulations were carried out, on 2D and 3D models, based on coefficients of restitution derived from back analyses performed on occurred events. Such simulations highlighted that the road can be regarded as an element at risk, because a relevant percentage of simulated falling boulders (up to 100%) would reach it. Results have been graphically reported on contour maps, which are a useful tool for the immediate recognition of the most critical

sectors (**Figure 65**, **Figure 66**). They show that a great percentage of falling rocks would cross the road heading downstream with variable kinetic energies (up to about 150 kJ), leading to potential worrying fatalities seen the great rate of tourism of the area. In fact, maps in **Figure 66** clearly shows that the highest kinetic energies are found at the most critical sectors of the study area. These values resulted from trajectory simulations based on single blocks of constant mass, according to the ones surveyed in the study area and actually fallen.

Moreover, with particular reference to MRA, although a variable percentage of end points is located along the upper segment, the articulated road path and the steepness of the slopes make the lower segment vulnerable by blocks rebounding on the upper segment. These, after having rebounded, gain kinetic energy towards the lower road.

Such complex and comprehensive analysis is the starting point for the quantitative risk assessment along this road, which was carried out through the Event Tree Analysis. This approach allows the estimation of probability values related to possible scenarios in case of rockfall, with a positive epilogue (e.g. *no damage*) or a negative perspective (e.g. *accident* or *damage*). The choice of the different branches composing the Event Tree has been conditioned by the peculiar geomechanical setting of the area and by the geometry of the road path, which at its northern sector can be divided into two parallel segments running at different altitudes (upper and lower). In this perspective, the probability calculation has been carried out at 23 sub-segments, chosen according to peculiar features of the road (e.g. change in direction at bends) or of the slopes (e.g. surveyed unstable blocks), by taking into account the trajectory of falling boulders, which represent the main conditioning element in this analysis.

The probabilities related to possible negative outcomes in case of rockfall were estimated by taking into account the possibility that boulders could either

damage the road, thus leading to economic loss and disruptions, or cause accidents to passing vehicles. Results prove that this sector of road is subjected to a relevant probability of accident, especially along its upper segment, which would be the first target of falling boulders. The highest values characterize those portions directly bordered by impending rock masses, while lowest values are mainly related to the downstream segments, where a lower amount of blocks is likely to go as far as.

Results were represented on final thematic maps (**Figure 75**, **Figure 76**), with the aim of providing a useful and intuitive tool for the representation of the risk variation along linear infrastructures.

The probability zonation is in accordance to the rockfall history of the area, because the most critical sectors actually represent portions of the road threatened by falling blocks in the past.

This study represents an example of scientific and analytic procedure, which can be applied in several critical areas worldwide, especially where the complexity of the geological conditions or of the road path may lead to important risks for people. The Event Tree can be customized according to specific patterns of the area and final maps can be drawn with all the probability values estimated during the analysis (e.g. probability of accident, probability of no damage), based on the aimed purposes. Furthermore, if necessary, the probability computation can also be further articulated, in case the estimation of injuries and deaths is needed (e.g. Bunce at al., 1997).

11.2. Application of InfraRed Thermography for the survey of rock slopes

Infrared Thermography has been employed herein as a new technique for the survey of jointed rock slopes, achieving interesting results based on the thermal behavior of rock masses. In this research, IRT outputs were analyzed and compared, with respect to the different time of the day and seasons, to find out what kind of information they offer. The methodological approach was very strict to ensure the reproducibility of the measurements and the critical evaluation of the results.

The comparison between the summer daily phases highlighted that the rock mass, regardless of the lithology, gains heat as long as it is exposed to the sunrays (**Figure 52**). Then, it begins to release heat through the fracture systems and the best IRT output is recorded in nighttime, when parasite radiation is lower and the difference between rock mass and ambient temperatures is at its maximum.

The discontinuity traces, along with fractured/crushed sectors, are marked by positive thermal anomalies, while regular planes (with no visible fractures) keep a lower temperature. This contrast makes easy to trace the main discontinuity systems and to map intensely jointed sectors. Such practice would be useful for a survey of unreachable rock masses, where a geostructural characterization is hard to perform (e.g. higher sectors, coastal cliffs).

Winter thermograms show a worse definition, due to the low heating of the rock face if direct radiation is not present (for example on a cloudy day). This means that the rock, on average, keeps a constant temperature during the day, resulting in less defined thermal outputs.

Among all the analyzed thermograms, the best outputs are related to the late cooling phase of rock masses (i.e. the nighttime shots), both in summer and winter. Such a result is in accordance with Teza et al. (2012), who suggested

measurements during the cooling phase because a direct sun heating induces high disturbance, with significant effects due to the relative position between the source and the facets of the surface.

An experimental index for the description of the rock mass cooling was introduced. This is the Cooling Rate Index (CRI), related to the cooling velocity of the rock. The cooling rate depends not only on the difference between the object and ambient temperatures, but it is strongly conditioned by the fracturing of the rock. For this reason, a preliminary relationship between CRI and RQD was established. The regression analysis resulted in a negative linear trend, showing that the higher the degree of fracturing of the rock, the faster its cooling. In this view, IRT could be employed also as a brand new, independent technology for the remote estimation of the degree of fracturing in rock masses, although further measurements in different contexts are needed to refine these relationship.

CONCLUSIONS

More than one conclusive consideration can be draw by archived results, with respect to both the specific study area and the followed procedure.

Starting from the first aspect, the highlights of this study are summarized as follows:

1) the analysis carried out at a strategic sector of eastern Sicily demonstrated that rock masses of Castelmola-Taormina area are affected by a great predisposition to landslide, thus they represent a worrying threat for the only communication route, traveled by a great tourism rate each year.

2) SP-10 road is a high risk infrastructure, threatened by a high probability of *damage* and by a relevant probability of *accident* in case of rockfalls.

3) The geometrical path of a road, especially in mountainous sectors, strongly condition its rockfall risk, because the road segments may act either as end point for blocks or as rebound points, enhancing the movement of blocks towards downstream with higher kinetic energies.

On the other hand, with reference to the scientific procedure followed herein:

4) the application of InfraRed Thermography for the study of the degree of fracturing of rock masses proved a useful tool for the estimation of the most fractured sectors and for the detection of the main discontinuity systems. The best quality of thermograms is achieved in nighttime, when no parasite radiation affects the acquisition of the thermal image.

5) The cooling behavior of rock masses can be studied by estimating their Cooling Rate Index (CRI), which proved an innovative index correlated to the degree of fracturing of the rock mass.

6) This study represents the example of a comprehensive procedure aimed at assessing the rockfall risk along roads through the specific approach of the Event Tree Analysis, which proved a suitable and versatile technique to deal with this kind of issues, although it is strongly conditioned by the subjectivity

of the operator computing the probabilities and by the results of rockfall trajectories simulations.

7) The starting point for such approach is the detailed knowledge of the study area and of its rockfall history, which has to be modeled according to the rock mass analysis and rockfall simulations.

8) Different probability scenarios can be considered, according to the specific purpose aimed.

9) The procedure can be applied at several mountainous transportation corridors worldwide, especially where the complexity of the geological conditions or of the road path may lead to important risks for the vehicle traffic.

10) Achieved results and their representation on thematic maps can be employed in the perspective of performing proper mitigation works along specific road segments, in order to prevent the occurrence of rockfalls and related consequences.

ACKNOWLEDGMENTS

I would like to express my special appreciation and thanks to my advisor Professor Domenico Calcaterra, who gave me the opportunity to be part of such a great experience, besides all the logistical difficulties. Thank you for the precious support you have offered me since the first time we “e-met”.

I would also like to thank Prof. Giovanna Pappalardo for encouraging my activity and for allowing me to grow as a research scientist, filling the working days with optimism, positivity, friendship and sincere advices. Thank you because you have never made me feeling only a PhD student, but also a colleague with whom sharing some scientific and professional issues.

Thank you to Prof. Sebastiano Perriello Zampelli for his suggestions and for the “pizza-times” we shared during my visits.

Thanks are also extended to Professors Paolo Budetta, Francesco Castelli and Carmelo Monaco for their useful revision of this thesis: your comments brought a great contribution of quality in this work.

A special thanks to my mother and father, who supported me both financially and emotionally during these years of doctoral course with no scholarship. You have been and always will be a landmark in my life.

Last but not least, I would like to acknowledge the girl who has been “walking” by my side for more than nine years and who deserves all my love: thank you M. Angelica, you are the most marvelous person I have ever met.

REFERENCES

Acquafredda P., Lorenzoni S., Zanettin-Lorenzoni E. The Devonian and Carboniferous volcanism of the Peloritan Mountains (Sicily) and the evolution of Palaeozoic basins in the Calabrian Peloritan Arc. Geological Journal, 26: 145–156, 1991.

Adamovski R., Masek L., Neuberger P. Analysis of rock mass borehole temperatures with vertical heat exchanger. Res. Agr. Eng.; 58 (2): 57-65, 2012.

Amanti M., Bertolini G., Ramasco M. The Italian landslides inventory–IFFI Project. In Proceedings of III Simposio Panamericano de deslizamientos, 1-2, 2001.

APAT- Agenzia per la Protezione dell'Ambiente e per I servizi Tecnici. Fenomeni di dissesto geologico – idraulico sui versanti, classificazione e simbologia. Manuali e Linee Guida 39/2006.

Arosio D., Longoni L., Papini M., Scaioni M., Zanzi L., Alba M. Towards rockfall forecasting through observing deformations and listening to microseismic emissions. Nat. Hazards Earth Syst. Sci., 9, 1119–1131, 2009.

Asef M.R., Reddish D.J., Lloyd P.W. Rock-support interaction analysis based on numerical modeling. Geotechnical and Geological Engineering, 18(1), 23-37, 2000.

Asteriou P., Saroglou H., Tsiambaos G. Geotechnical and kinematic parameters affecting the coefficients of restitution for rockfall analysis. International Journal of Rock Mechanics & Mining Sciences, 54, 103–113, 2012.

Athanasiou-Grivas, D. A reliability approach to the design of geotechnical systems. Rensselaer Polytechnic Institute Research Paper, Transportation Research Board Conference, Washington, DC, 1980.

Atzori P., Cirrincione R., Kern H., Mazzoleni P., Pezzino A., Puglisi G., Punturo R., Trombetta A. The abundance of 53 elements and petrovolumetric models of the crust in northeastern Peloritani Mountains (Site 8), in: The Abundance of 55 Elements and Petrovolumetric Models in Nine Type Areas from the Crystalline Basements of Italy, with some Geophysical and Petrophysical Data, edited by: Sassi, F. P., Acc. Naz. Sci. XL, 32, 309–358, 2003.

Atzori P., Ferla P., Paglionico A., Piccarreta G., Rottura A. Remnants of the Hercynian orogen along the Calabrian-Peloritan arc, southern Italy: a review. Journal of the Geological Society, 141: 137–145, 1984.

Atzori P., Cirrincione R., Mazzoleni P., Pezzino A., Trombetta A. A tentative pre-Variscan geodynamic model for the Palaeozoic basement of the Peloritani Mountains (Sicily): evidence from meta-igneous products. Periodico di Mineralogia, 70: 255–267, 2001.

AVI Project: Progetto AVI (Aree vulnerate da calamità idrogeologiche), Regione Sicilia Relazione Finale ed Allegati, CNRGNDCI, http://avi.gndci.cnr.it/, Italy, 1998.

Azzoni A., Barbera G.L., Zaninetti A. Analysis and prediction of rockfalls using a mathematical model. International J. Rock Mechanics and Mining Sci. 32, 709–724, 1995.

Bacilieri C. I borghi più belli d'Italia, Il fascino dell'Italia nascosta, Società Editrice Romana, Italy, 2012.

Ball D., Watt J. Risk Management and Cultural Presentation. Proceedings of the ARIADNE Workshop 4, Vulnerability of cultural heritage to hazards and prevention measures, Prague, 18–24 August, 2001.

Baratta, M. La catastrofe sismica calabro-messinese (28 Dicembre 1908). Relazione alla Soc. Geogr. Ital., 1910.

Barbano M.S., Pappalardo G., Pirrotta C. and **Mineo S.** Landslide triggers along volcanic rock slopes in eastern Sicily (Italy). Natural Hazards, 73, 3, 1587-1607, 2014. DOI: 10.1007/s11069-014-1160-1.

Barbano M.S., Azzaro R., Grasso D.E. Earthquake Damage Scenarios And Seismic Hazard Of Messina, North-Eastern Sicily (Italy) As Inferred From Historical Data. Journal of Earthquake Engineering,9 (6), 805–830, 2005.

Baroň I, Bečkovský D., Míča L. Application of infrared thermography for mapping open fractures in deep-seated rockslides and unstable cliffs. Landslides, 11: 15–27, 2012. DOI 10.1007/s10346-012-0367-z.

Barton N.R., Choubey V. The shear strength of rock joints in theory and practice. Rock Mech. 10(1-2), 1-54, 1977.

Beylich A.A., Kneisel C. Sediment budget and relief development in Hrafndalur, subarctic oceanic Eastern Iceland: Arctic, Antarctic, and Alpine research. Arct. Antarct. Alp. Res. 41, 3–17, 2009.

Bianca M., Monaco C., Tortorici L., Cernobori L. Quaternary normal faulting in southeastern Sicily (Italy): a seismic source for the 1693 large earthquake. Geophys. J. Int 139, 370–394. 1999.

Bieniawski Z.T. Engineering Rock Mass Classification. John Wiley & Son, New York, 1989, 251 pp.

Boccaletti M., Nicolich R., Tortorici L. New data and hypothesis on the development of the Tyrrhenian basin. Palaeo. Palaeo. Palaeo. 77, 15–40, 1990.

Boschi E., Ferrari G., Gasperini P., Guidoboni E., Smriglio G., Valensise G. Catalogo dei forti terremoti in Italia dal 461 a.c. al 1980. Istituto Nazionale di Geofisica, S.G.A, Roma, 1995a.

Boschi E., Guidoboni E., Mariotti D. Seismic effects of the strongest historical earthquakes in the Syracuse area. Ann. Geof. 38, 223–253, 1995b.

Bozzolo D., Pamini R., Hutter K.. Rockfall analysis — a mathematical model and its test with field data. Proceedings of the 5th International Symposium on Landslides in Lausanne. Balkema, Rotterdam, The Netherlands, pp. 555–560, 1986.

Budetta, P. Assessment of rockfall risk along roads, Nat. Hazards Earth Syst. Sci., 4, 71–81, doi:10.5194/nhess-4-71-2004, 2004.

Budetta P. Rockfall-induced impact force causing a debris flow on a volcanoclastic soil slope: a case study in southern Italy, Nat. Hazards Earth Syst. Sci., 10, 1995–2006, doi:10.5194/nhess-10- 1995-2010, 2010.

Budetta P. Application of the Swiss Federal Guidelines on rock fall hazard: a case study in the Cilento region (Southern Italy). Landslides, 8:381–389, 2011. DOI 10.1007/s10346-010-0247-3

Budetta P., De Luca C., Nappi M. Quantitative rockfall risk assessment foran important road by means of the rockfallrisk management (RO.MA.) method. Bull Eng Geol Environ 75:1377-1397, 2016. DOI 10.1007/s10064-015-0798-6

Bunce C. M., Cruden D. M., Morgenstern N. R. Assessment of the hazard from rockfall on a highway, Can. Geotech˙J., 34, 344–356, 1997.

Calcaterra D., Parise M. Weathering as a predisposing factor to slope movements: An introduction. Geological Society Engineering Geology Special Publication Volume 23, 1-4, 2010.

Catalano S., Di Stefano P., Sulli A., Vitale F.P. evoluzione paleogeografia e strutturale della Sicilia e dei mari adiacenti, Naturalista sicil., S. IV, Vol. XIX, 3–4, 143–187, 1995.

Catalano S., Di Stefano A. Sollevamenti e tettogenesi pleistocenica lungo il margine tirrenico dei Monti Peloritani: integrazione dei dati geomorfologici, strutturali e biostratigrafici. Ital. J. Quat. Sci. 10 (2) (6 pp.), 1997.

Cehlin M., Moshfegh B., Sandberg M. Visualization and measuring of air temperatures based on infrared thermography. In Proceedings of 7th International Conference on Air Distribution in Rooms ROOMVENT, Reading, UK, 9-12 July, 2000.

Chau K.T., Wong R.H.C., Lee C.F. Rockfall problems in Hong Kong and some new experimental results for coefficient of restitution. Int. J. Rock Mech. Min. Sci., 35, 662–663, 1998.

Cirrincione R., Fazio E., Ortolano G., Pezzino A., Punturo R. Fault-related rocks: deciphering the structural–metamorphic evolution of an accretionary wedge in a collisional belt, NE Sicily, Int. Geol. Rev., 54, 940–956, 2012.

Cirrincione R., Atzori P., Pezzino A. Sub-greenschist facies assemblages of metabasites from south-eastern Peloritani range (NE-Sicily). Mineralogy and Petrology, 67: 193–212, 1999.

Cluni F., Costarelli D., Minotti A.M., Vinti G. Enhancement of thermographic images as tool for structural analysis in earthquake engineering. NDT & E International; 70: 60-72, 2015.

CNR. Norme tecniche per le costruzioni stradali. Pon. 1V: 11-15, 1980.

Crosta G. B., Agliardi, F. A methodology for physically based rockfall hazard assessment, Nat. Hazards Earth Syst. Sci., 3, 407–422, doi:10.5194/nhess-3-407-2003, 2003.

Cruden D.M., Varnes D.J. Landslide types and processes. In: Turner AK, Schuster RL (eds) Landslides investigation and mitigation. Transportation research board, US National Research Council. Special Report 247, Washington, DC, Chapter 3, pp. 36–75, 1996.

Davies M.C.R., Hamza O., Harris C. The effect of rise in mean annual temperature on the stability of rock slopes containing ice-filled discontinuities. Permafrost and Periglacial Processes 12 (1), 137–144, 2001.

De Almeida, J. A. and Kullberg, J. C.: Rockfall hazard and risk analysis for Monte da Lua, Sintra, Portugal, Nat. Hazards, 58, 289–310, 2011.

De Capoa P., Guerrera F., Perrone V. & Serrano F. New biostratigraphic data on the Frazzanò Formation (Longi-Taormina Unit): consequences on defining the deformation age of the Calabria-Peloritani Arc Southern Sector. Riv. It. Paleontologia e Stratigrafia, 103, 343-356, 1997.

De Guidi G., Catalano S., Monaco C., Tortorici L. Morphological evidence of Holocene coseismic deformation in the Taormina region (NE Sicily). Journal of Geodynamics 36, 193–211, 2003.

De La Beche H.T., Broderip W.J. Researches in theoretical geology. London, C. Knight.; 408 pp, 1972.

De Vita P., Cevasco A., Cavallo C. Detailed rock failure susceptibility mapping in steep rocky coasts by means of non-contact geostructural surveys: the case study of the Tigullio Gulf (Eastern Liguria, Northern Italy). Nat. Hazards Earth Syst. Sci., 12, 867–880, 2012.

Deere D.U. Technical Description of Rock Cores for Engineering Purposes, Felsmechanik und InQenieurgeologie (Rock Mechanics and Engineering Geology), 1:1, pp. 16-22, 1963.

Deere D.U. Rock Quality Designation (RQD) After Twenty Years. U.S. Department Of Commerce National Technical Information Service Springfield, Va. 22161, 1989.

Deere D.U., Miller R.P. Engineering Classification and Index Properties of Intact Rock. Technical Report No. AFWL-TR-65-116, Air Force Weapons Laboratory, Kirkland Air Force Base, New Mexico, 1966.

DeWitt N. Theory and practice of radiation thermometry. New York 1988, Wiley.

Dewey J.F., Helman L.M., Turco E., Hutton D.W.H., Knott, S.D. Kinematics of the western Mediterranean. In: Coward, M.P., Dietrich, D., Park, R.G. (Eds.), Alpine Tectonics. Geol. Soc. Lond. Spec. Publ. 45, 265-283, 1989.

Di Martire D., Novellino A., Ramondini M., Calcaterra D. A-Differential Synthetic Aperture Radar Interferometry analysis of a Deep Seated Gravitational Slope

Deformation occurring at Bisaccia (Italy). S cience of The Total Environment 550:556-573, 2016.

Dochez S., Laouafa F., Franck C., Guedon S., Martineau F., D'amato J. & Saintenoy A. Multi-Scale Analysis of Water Alteration on the Rockslope Stability Framework. Acta Geophysica, 62 (5), 1025-1048, 2014. doi: 10.2478/s11600-014-0232-7.

Dorren L.K.A., Seijmonsbergen A.C. Comparison of three GIS-based models for predicting rockfall runout zones at a regional scale. Geomorphology, 56, 49–64, 2003.

Dorren L.K.A., Berger F., Putters, U.S. Real-size experiments and 3-D simulation of rockfall on forested and nonforested slopes, Nat. Hazards Earth Syst. Sci., 6, 145–153, doi:10.5194/nhess-6-145-2006, 2006.

Dueé G. Etude géologique des Monts Nebrodi (Sicile), Thèse Fac. Sci., 2 voll, 221–169, Paris, 1969.

Dumas B., Gueremy P., Lhenaff R., Raffi J. Relief et ne´otectonique de la facade orientale du detroit de Messine (Calabre, Italie). Trav. R.C.P. CNRS 461, 105–125, 1978.

Erismann T.H. Flowing, rolling, bouncing, sliding, synopsis of basic mechanisms. Acta Mechanica 64, 101–110, 1986.

Evans S.G., Hungr O. The assessment of rockfall hazard at the base of talus slopes. Canadian Geotechnical J. 30, 620–636, 1993.

Fanti R., Gigli G., Lombardi L., Tapete D., Canuti P. Terrestrial laser scanning for rockfall stability analysis in the cultural heritage site of Pitigliano (Italy). Landslides, 10:409–420, 2013. DOI 10.1007/s10346-012-0329-5

Ferrara V., Pappalardo G. Kinematic analysis of rock falls in an urban area: The case of Castelmola hill near Taormina (Sicily, Italy), Geomorphology, 66, 373–383, 2005.

Ferrari P., Giannini F. Geometria e progetto di strade- Ingegneria stradale. Vol. 1° ISEDI: pp. 344, 1975.

Ferrero A. M., Forlani G., Rondella R., Voyat H. I.: Advanced Geostructural Survey Methods Applied to Rock Mass Characterization, Rock Mech. Rock Eng., 42, 631–665, 2009.

Finetti I.R., Lentini F., Carbone S., Catalano S., Del Ben, A. Il sistema Appenninico Meridionale-Arco Calabro-Sicilia nel Mediterraneo Centrale: studio geologico geofisico. Boll. Soc. Geol. Ital. 115, 529–559, 1996.

Fisher R.A. Dispersion on a sphere. Proceedings of the Royal Society of London, Series A, 217, 295-305, 1953.

FLIR. User's manual FLIR Tools/Tools+. Publ n. T559600, 152pp, 2015.

Frattini P., Crosta G.B., Allievi J. Damage to buildings in large slope rock instabilities monitored with the PSInSAR™ technique. Remote Sens., 5 (10), pp. 4753–4773, 2013. http://dx.doi.org/10.3390/rs5104753

Frattini P., Crosta G.B., Lari S., Agliardi F. Probabilistic rockfall hazard analysis (PRHA). In: Eberhardt E, Froese C, Turner AK, Leroueil S (eds) Landslides and engineered slopes: protecting society through improved understanding. Taylor & Francis, London, pp 1145–1151, 2012.

Furukawa Y. Infrared thermography of the fumarole area in the active crater of the Aso volcano, Japan, using a consumer digital camera. Journal of Asian Earth Sciences; 38: 283–288, 2010. doi:10.1016/j.jseaes.2010.02.001

Galli P., Bosi V. Paleoseismology along the Cittanova fault: implications for seimotectonics and earthquake recurrence in Calabria (southern Italy). J. Geophys. Res. 107, 2002.

Gardner J.S. Rockfall frequency and distribution in the Highwood Pass area, Canadian Rocky Mountains. Zeitschrift für Geomorphologie N.F. 27, 311–324, 1983.

Ghisetti F. Evoluzione neotettonica dei principali sistemi di faglie della Calabria centrale. Boll. Soc. Geol. It. 98, 387–430, 1979.

Giani, G. P. Rock Slope Stability Analysis, A. A. Balkema, Rotterdam, the Netherlands, 1992.

Gigli G., Casagli N. Semi-automatic extraction of rock mass structural data from high resolution LIDAR point clouds. Int J of Rock Mech Min Sci 48:187–198, 2011.

Goldsmith W. Impact: The Theory and Physical Behavior of Colliding Solids, Edward Arnold, London, 1960.

Goodman R.E. Introduction to rock mechanics –second edition-. John Wiley & Sons, 1989.

Goodman R.E., Bray J. Toppling of rock slopes. ASCE, Proc. Specialty Conf. on Rock Eng. for Foundations and Slopes, Boulder, CO, 2, 201–34, 1976.

Gordon S., Lichti D., Stewart M. Application of a high-resolution, ground based laser scanner for deformation measurements. In: Proceedings of 10th International FIG Symposium on Deformation Measurements, Orange, California, USA, 19–22 March, 23-32 2001.

Grinzato E., Vavilov V., Kauppinen T. Quantitative infrared thermography in buildings. Energy Buildings; 29:1–9, 1998.

Gupta V., Tandon R.S. Kinematic rockfall hazard assessment along a transportation corridor in the Upper Alaknanda valley, Garhwal Himalaya, India. Bull Eng Geol Environ 74:315-326, 2015. doi:10.1007/s10064-014-0623-7

Guzzetti F., Reichenbach P. Rockfalls and Their Hazard. In Tree Rings and Natural Hazards, Ed. Stoffel et al., Springer, 129-137, 2010.

Guzzetti F., Crosta G., Detti R., Agliardi F. STONE: a computer program for the three-dimensional simulatation of rock-falls. Comput Geosci 28(9):1079–1083, 2002.

Hales T.C., Roering J.J. Climatic controls on frost cracking and implications for the evolution of bedrock landscapes. J. Geophys. Res. Earth Surf. 2003–2012, 112, 2007.

Haneberg W.C. Using close range terrestrial digital photogrammetry for 3-D rock slope modeling and discontinuity mapping in the United States, Bull. Eng. Geol. Environ., 67, 457–469, 2008.

Hantz D., Dussauge Peisser C., Jeannin M., Veneon J.M. Rock Fall Hazard Assessment: From Qualitative to Quantitative Failure Probability. Int. conf. on Fast Slope Movements, Naples, pp. 263–267, 2003.

Harp E.L., Wilson R.C. Shaking intensity thresholds for rock falls and slides: Evidence from 1987 Whittier Narrows and Superstition Hills earthquake strongmotion records. Bulletin of the Seismological Soci. of America 85 (6), 1739–1757, 1995.

Harr M. E. Mechanics of Particulate Matter—A Probabilistic Approach. McGraw-Hill, New York, 543 pp, 1977.

Hartford D.N.D., Baecher G.B. Risk and uncertainty in dam safety. Thomas Telford, London, 2004.

Heckmann T., Hilger L., Vehling L., Becht M. Integrating field measurements, a geomorphological map and stochastic modelling to estimate the spatially distributed rockfall sediment budget of the Upper Kaunertal, Austrian Central Alps. Geomorphology 260, 16–31, 2016.

Hillel D. Environmental Soil Physics. Academic Press, New York; 771 pp, 1998.

Ho K., Ko F. Application of quantified risk analysis in landslide risk management practice: Hong Kong experience, Georisk, 3, 134–146, doi:10.1080/17499510902873074, 2009.

Hocking G. A method for distinguishing between single and double plane sliding of tetrahedral wedges. Int. J. Rock Mech. Mining Sci., 13, 225–6, 1976.

Hoek E. Practical Rock Engineering, 115–136, available at:www. rocscience.com(last access: 16 September 2008), 2000.

Hoek E. Rockfall – A Program in Basic for the Analysis of Rockfalls from Slopes, Department of Civil engineering, University of Toronto, Canada, 1987.

Hoek E., Bray J.W. Rock Slope Engineering, Third Edition, The Institution of Mining and Metallurgy, London, p. 368, 1981.

Hoek E., Bray J. Rock Slope Engineering, 1st edn, IMM, London, 1977.

His J.P., Fell R. Landslide risk assessment of coal refuse emplacement. In: Landslide Risk Management (Hungr O., Fell R., Couture R., Eberhardt E. (eds)). Balkema, Rotterdam, pp. 224-238, 2005.

Hudson R.D. Infrared System Engineering. Wiley-Interscience, John Wiley & Sons, New York/London/Sydney/Toronto; 642 pp, 1969.

Hungr O., Evans S.G. Engineering evaluation of fragmental rockfall hazards. Proceedings of the 5th International Symposium on Landslides in Lausanne. The Netherlands, Balkema, Rotterdam, pp. 685–690, 1988.

Hungr O., Picarelli L. The Varnes classification of landslide types, an update. Landslides, 2014. DOI 10.1007/s10346-013-0436-y

Hungr O., Evans S.G., Bovis M., Hutchinson J.N. Review of the classification of landslides of the flow type. Environ Eng Geosci VII:221–238, 2001.

ISRM. The complete ISRM suggested methods for rock characterization, testing and monitoring: 1974–2006. In: Ulusay, R., Hudson, J.A. (Eds.), Suggested Methods Prepared by the Commission on Testing Methods, International Society for Rock Mechanics, Compilation Arranged by the ISRM Turkish National Group, Kozan Ofset, Ankara, Turkey 2007 (628 pp.).

Jaboyedoff M., Baillifard F., Bardou E., Girod F. The effect of weathering on alpine rock instability. Q. J. Eng. Geol. Hydrogeol. 37, 95–103, 2004.

Jacques E., Monaco C., Tapponnier P., Tortorici L., Winter T. Faulting and earthquake triggering during the 1783 Calabria seismic sequence. Geophys. J. Int. 147, 499–516, 2001.

Jaedicke C., Lied K., Kronholm K. Integrated database for rapid mass movements in Norway. Nat. Hazards Earth Syst. Sci. 9, 2009.

Kastberger G., Stachl R. Infrared imaging technology and biological applications. Behavior Research Methods, Instruments, & Computer; 35 (3): 429-439, 2003.

Kim B.H., Kaiser P.K., Grasselli G. Influence of persistence on behavior of fractured rock masses, Geol. Soc. Lond. Special Publications, 284: 161 – 173, 20070 Doi:10.1144/SP284.11.

Kirkby M.J., Statham I.. Surface stone movement and scree formation. J. Geol. 83, 349–362, 1975.

La Sicilia, Catania, 27 February, yr LXVIII, n. 57, 2012.

Lacasse S., Nadim F. Landslide risk assessment and mitigation strategy. Invited Lecture, state-of-the-art. First World Landslide Forum, Global Landslide Risk Reduction, International Consortium of Landslides, Tokyo, 31-61, 2008.

Lambert S., Nicot F. Rockfall engineering. ISTE Ltd and John Wiley & Sons, Inc. 2011.

Lee E.M., Jones D.K.C. Landslide risk assessment second edition.ICE Publishing, London, pp. 509, 2014.

Lee E. M., Moore R. Ventnor Undercliff: Development of landslide scenarios and quantitative risk assessment'. Proc. Int. Conf. 'Landslides and climate change - Challenges and solutions'. Ventnor, May 2007. Taylor & Francis, 2007.

Lentini F. Carta Geologica della Provincia di Messina, scala 1:50,000. Firenze: S.EL.CA., 2000.

Lentini F., Vezzani L. Le unità meso-cenozoiche della copertura sedimentaria del basamento cristallino peloritano (Sicilia nord-orientale): Bollettino Societa Geologica Italiana, 94, 537–554, 1975.

Lentini F., Carbone S., Guarnieri P. Collisional and postcollisional tectonics of the Apenninic-Maghrebian orogen (southern Italy), Geological Society of America Special Paper 409, Geological Society of America, Boulder, Colorado, 57–81, 2006.

Liu S., Xu Z., Wu L., Ma B., Liu X. Infrared imaging detection of hidden dander in mine engineering. Proc. of Symp. on Progress in electromagnetics research, Suzhou, China; 12-16, 125-129, 2011.

Macciotta R., Martin C.D., Edwards T., Cruden D.M., Keegan T. Quantifying weather conditions for rock fall hazard management. Georisk 9:171-186, 2015. doi:10.1080/17499518.2015.1061673

Markland J.T. A useful technique for estimating the stability of rock slopes when the rigid wedge sliding type of failure is expected, Imp. Coll. Rock Mech. Res. Rep. 19, Imperial College of Science and Technology, London, 10 pp., 1972.

Martino S., Mazzanti P. Integrating geomechanical surveys and remote sensing for sea cliff slope stability analysis: the Mt. Pucci case study (Italy). Nat. Hazards Earth Syst. Sci., 14, 831–848, 2014.

Marzorati S., Luzi L., De Amicis M. Rock falls induced by earthquakes: a statistical approach. Soil Dynamics and Earthquake Engineering 22 (7), 565–577, 2002.

Massey C. I., Hodgson I. F., Petley D. N. A rockfall simulation study for housing development in Gibraltar, 10th IAEG International Congress, Paper number 377, Nottingham, United Kingdom, 2006.

Matheson G.D. Rock stability assessment in preliminary investigations, graphical methods. Department of the Environment, Department of Transport and Road Research Laboratory Report LR1039, 1983.

Mateos R.M., Garcia-Moreno I., Herrera G., Reichenbach P., Sarro R., Rius J., Aguilo R., Fiorucci F. Calibration and validation of rockfall modelling at regional scale: application along a roadway in Mallorca (Spain) and organization of its management. Landslides, 13 (4), 751–763, 2016.

Matsuoka N., Sakai H. Rockfall activity from an alpine cliff during thawing periods. Geomorphology 28, 309–328, 1999.

Matsuoka N. Frost wedging and rockfalls on high mountain rock slopes: 11 years of observations in the Swiss Alps. Geophysical Res. Abstracts 8, 05344, 2006.

Meola C., Carlomagno G.M. Recent advances in the use of infrared thermography. Measurement Science and Technology; 15: 27-58, 2004.

Michoud M., Baumann V., Derron M., Jaboyedoff M., Lauknes T.R.. Slope instabilitydetection along the national 7 and the Potrerillos dam reservoir, Argentina, using the Small-Baseline InSAR technique. Engineering Geology for Society and Territory. 2, pp. 295–299, 2015. http://dx.doi.org/10.1007/978-3-319-09057-3_44.

Mineo S., Pappalardo G. The Use of Infrared Thermography for Porosity Assessment of Intact Rock. Rock Mechanics and Rock Engineering, 49 (8), 3027-3039, 2016a. DOI: 10.1007/s00603-016-0992-2

Mineo S., Pappalardo G. Preliminary results on the estimation of porosity in intact rock through InfraRed Thermography. Rend. Online Soc. Geol. It., Vol. 41, 317-320, 2016b. DOI: 10.3301/ROL.2016.157

Mineo S., Calcaterra D., Perriello Zampelli S and Pappalardo G. Application of Infrared Thermography for the survey of intensely jointed rock slopes. Rend. Online Soc. Geol. It., Vol. 35, 212-215, 2015a. DOI: 10.3301/ROL.2015.103

Mineo S., Pappalardo G., Rapisarda F., Cubito A. and Di Maria G. Integrated geostructural, seismic and infrared thermography surveys for the study of an unstable rock slope in the Peloritani Chain (NE Sicily). Engineering Geology, 195, 225–235, 2015b. DOI: 10.1016/j.enggeo.2015.06.010

Monaco C., Bianca M., Catalano S., De Guidi G., Tortorici L. Sudden change in the Late Quaternary tectonic regime in eastern Sicily: evidences from geological and geomorphological features. Boll. Soc. Geol. It., Vol. Spec. n 1, 901–913, 2002.

Monaco C., Tortorici L. Active faulting in the Calabrian Arc and eastern Sicily. J. Geodynamics 29, 407–424, 2000.

Monaco C., Tapponier P., Tortorici L., Gillot P.Y. Late Quaternary slip rates on the Acireale-Piedimonte normal faults and tectonic origin of Mt Etna (Sicily). Earth Planet. Sci. Lett. 147, 125–139, 1997.

Murton J.B., Peterson R., Ozouf J.C. Bedrock fracture by ice segregation in cold regions. Science 314:1127-1129, 2006. doi:10.1126/science.1132127

National Highway Institute: Rockfall Hazard Rating System participant's manual, NHI Course No. 130220, U.S. Dept. of Transportation, Federal Highway Administration, Publication No. FHWA SA-93–057, 1993.

Nicholson G.A., Bieniawski Z.T. A nonlinear deformation modulus based on rock mass classification. International Journal of Mining and Geological Engineering, 8: 181, 1990.

Niethammer U., James M.R., Rothmund S., Travelletti J., Joswig M. UAV-based remote sensing of the Super-Sauze landslide: Evaluation and results. Engineering Geology 128, 2-11, 2012.

Norrish N.I., Wyllie D.C. Rock slopes stability analysis. Transportation Research Voard. Special Report, Serial. Published in Washington D.C. 247, pp. 509–513, 1996.

Okura Y., Kitahara H., Sammori T., Kawanami, A. The effects of rockfall volume on runout distance, Eng. Geol., 58, 109– 124, 2000.

Oppikofer T., Jaboyedoff M., Blikra L., Derron M.-H., Metzger R. Characterization and monitoring of the Aknes rockslide using terrestrial laser scanning. Nat Hazards Earth Syst Sci 9:1003–1019, 2009.

P.A.I. Piano Stralcio di Bacino per l'Assetto Idrogeologico, Regione Siciliana, http://www.sitr.regione.sicilia.it/pai/ (last access: 3 February 2014), 2006.

Palmström A. Measurements of and Correlations between Block Size and Rock Quality Designation (RQD). Tunnels and Underground Space Technology; 20: 362-377, 2005.

Palmström A. The Volumetric Joint Count: A Useful and Simple Measure of the Degree of Rock Mass Jointing, Proceedings of the 4th Congress of the International Association of Engineering Geoloav, 5:221-228, 1982.

Palmström A. Measurement and characterization of rock mass jointing; in situ characterization of rocks. In: Sharma VM, Saxena KR, editors. New Delhi: Oxford & IBH Publishing Co. Pvt. Ltd., and Rotterdam: A.A. Balkema, p. 358, 1974.

Pantelidis L., Kokkalis A. Designing passive rockfall measures based on computer simulation and field experience to enhance highway safety, Int. J. Rock Mech. Min. Sci., 48, 1369– 1375, 2011.

Pappalardo G., **Mineo S.** Investigation on the mechanical attitude of basaltic rocks from Mount Etna through InfraRed Thermography and laboratory tests. Construction and Building Materials 134, 228–235, 2017. DOI: 10.1016/j.conbuildmat.2016.12.146

Pappalardo G., **Mineo S.** Rockfall Hazard and Risk Assessment: The Promontory of the Pre-Hellenic Village Castelmola Case, North-Eastern Sicily (Italy). In G. Lollino et al. (eds.), Engineering Geology for Society and Territory – Volume 2, 1989-1993, 2015. DOI: 10.1007/978-3-319-09057-3_353

Pappalardo G., **Mineo S**., Perriello Zampelli S., Cubito A., Calcaterra D. InfraRed Thermography proposed for the estimation of the Cooling Rate Index in the remote survey of rock masses. International Journal Of Rock Mechanics And Mining Sciences, 83, 182-196, 2016a. DOI: 10.1016/j.ijrmms.2016.01.010

Pappalardo G., Imposa S., **Mineo S**., Grassi S. Evaluation of the stability of a rock cliff by means of geophysical and geomechanical surveys in a cultural heritage site (south-eastern Sicily). Italian Journal of Geosciences, 135 (2), 308-323, 2016b. DOI: 10.3301/IJG.2015.31

Pappalardo G., **Mineo S.** and Rapisarda F. Rockfall hazard assessment along a road on the Peloritani Mountains (northeastern Sicily, Italy). Nat. Hazards Earth Syst. Sci., 14, 2735–2748, 2014. doi:10.5194/nhess-14-2735-2014.

Patton F.D. Multiple modes of shear failure in rock, Proc. of the 1st International Cong. on Rock Mech., Lisbon, 1: 509 – 515, 1996.

Parise M. Landslide hazard zonation of slopes susceptible to rock falls and topples, Nat. Hazards Earth Syst. Sci., 2, 37–49, doi:10.5194/nhess-2-37-2002, 2002.

Park J., Park H.D. The effect of frost weathering at the dinosaur tracksite in Seoyu-ri, Hwasun, Korea. Bull Eng Geol, 2016 Environ. doi:10.1007/s10064-016-0970-7

Paronuzzi P. Rockfall-induced block propagation on a soil slope, northern Italy, Envirio. Geol., 58, 1451–1466, 2009.

Peila D., Guardini C. Use of the event tree to assess the risk reduction obtained from rockfall protection devices. Nat. Hazards Earth Syst. Sci., 8, 1441–1450, 2008.

Perriello Zampelli S., De Vita P., Imbriaco D., Calcaterra D. Failure Mechanisms of the Mount Catiello Rock Avalanche in the Sorrento-Amalfi Peninsula (Southern Italy). In G. Lollino et al. (eds.), Engineering Geology for Society and Territory – Volume 2, 813-816, 2015.

Pfeiffer T. J., Bowen, T. D. Computer simulation of rockfalls, Bull. Assoc. Eng. Geol., 26, 135–146, 1989.

Pierson L.A., Davis S.A., Van Vickle R. Rockfall Hazard Rating System—Implementation Manual, Federal Highway Administration (FHWA), Report FHWAOR- EG-90–01, FHWA, US Department of Transportation. 1990.

Piteau D.R. Characterizing and Extrapolating Rock Joint Properties in Engineering Practice. Geomechanik — Fortschritte in der Theorie und deren Auswirkungen auf die Praxis / Geomechanics — Progress in Theory and Its Effects on Practice Volume 2 of the series Rock Mechanics / Felsmechanik / Mécanique des Roches pp 5-31, 1973.

Poetsch M., Schubert W., Gaich A. The application of metric 3D images for the mechanical analysis of keyblocks. In: Eberhardt E, Stead D, Morrison T (eds.) Rock mechanics: meeting society's challenges and demands: proceedings, 1st Canada-US rock mechanics symposium, Vancouver, Canada, 77–84, 2007.

Postpischl D. Catalogo dei terremoti italiani dall'anno 1000 al 1980. CNR, P.F. Geodinamica, Graficco, Bologna, 1985.

Prendes-Gero M.B., Suárez-Domínguez F.J., González-Nicieza C., Álvarez-Fernández M.I. Infrared thermography methodology applied to detect localized rockfalls in self-supporting underground mines. In: Kwa´sniewski & Łyd˙zba, editors, Rock Mechanics for Resources, Energy and Environment, Taylor & Francis Group, London; 825-829, 2013.

Rinker J.N. Airborne infrared thermal detection of caves and crevasses. Photogramm. Eng. Remote Sens.; 41: 1391–1400, 1975.

Ritchie A.M. Evaluation of rockfall and its control. Washington, DC: Highway Research Board, National Research Council, Highway Research Record, 17, pp. 13–28, 1963.

Roberds W. Estimating temporal and spatial variability and vulnerability. In: Hungr O, Fell R, Couture R, Eberhardt E (eds) Proc. landslide risk management. Taylor and Francis Group, London, pp 3–26 (ISBN: 04 1538 043X), 2005.

Robotham M. E., Wang H. Walton, G. Assessment of risk from rockfall from active and abandoned quarry slopes, T. Inst. Min. Metal., 104, A25–A33, 1995.

Rouyeta L., Kristensen L., Derron M-H, Michouda C., Harald Blikra L., Jaboyedoff M., Lauknes T.R. Evidence of rock slope breathing using ground-based InSAR. Geomorphology. http://dx.doi.org/10.1016/j.geomorph.2016.07.005

Saroglou H., Marinos V., Marinos P., Tsiambaos G. Rockfall hazard and risk assessment: an example from a high promontory at the historical site of Monemvasia, Greece, Nat. Hazards Earth Syst. Sci., 12, 1823–1836, doi:10.5194/nhess-12-1823- 2012, 2012.

Sarro R., Mateos R.M., García-Moreno I., Herrera G., Reichenbach P., Laín L., Paredes C. The Son Poc rockfall (Mallorca, Spain) on the 6th of March 2013: 3D simulation. Landslides 11, 493–503, 2014.

Sass O. Temporal variability of rockfall in the Bavarian Alps, Germany. Arctic, Antarctic, and Alpine Res. 37 (4), 564–573, 2005.

Scandone P., Giunta G., Liguori V. The connection between the Apulia and Sahara continental margins in the Southern Apennines and in Sicily. Rapp. P-V. Reun., Cons. Int. Explor. Mer., 26e Congr., 23 (4A): 99-103, 1974.

Scesi L., Seno S., Gioia U., Mazzucchelli A. Pareti rocciose instabili e strade: un sistema di valutazione delle priorit`a di intervento, Associazione Georisorse ed Ambiente (GEAM), Torino, 92–102, 2001.

Schober A., Bannwart C., Keushnig M. Rockfall modeling in high alpine terrain-validation and limitations. Geomech. Tunn. 5 (4), 368-378, 2012.

Schneuwly D.M., Stoffel M., Tree-ring based reconstruction of the seasonal timing, major events and origin of rockfall on a case-study slope in the Swiss Alps. Nat. Hazards Earth Syst. Sci., 8, 203-211, 2008.

Schweigl J., Ferretti C., NÖssing L. Geotechnical characterization and rockfall simulation of a slope: a practical case study from South Tyrol (Italy), Eng. Geol., 67, 281–296, 2003.

Serafim J., Pereira J. considerations of the geomechanics classification of Bieniawski. Proceeding International Symposium on Engineering Geology and Underground excavation, LNEC, Lisbona, 1983.

Shannon H.R., Sigda J.M., Van Dam R.L., Handrickx J.M.H., McLemore V.T. Thermal camera imaging of rock piles at the Questa Molybdenum Mine, Questa, New Mexico. Proc. 2005 National Meeting of the American Society of Mining and Reclamation, June 19–23, ASMR, 1015–1028, 2005.

Shick, R. Eine seismotektonische Bearbeitung des Erdbebens von Messina im Jahre 1908. Geol. Jahrb 11, 3–74, 1977.

Somma R., Messina A., Perrone V. The Cambrian to Aquitanian geological record of the Longi–Taormina Unit (Calabria-Peloritani Arc, southern Italy): geodynamic implications. Geodinamica Acta, 18: 417–430, 2005.

Squarzoni C., Galgaro A., Teza G., Acosta C.A.T, Pernito M.A., Bucceri N. Terrestrial laser scanner and infrared thermography in rock fall prone slope analysis. Geophysical Research Abstracts, Vol. 10, EGU2008-A-09254, 2008.

Statham I., Francis S.C.. Influence of scree accumulation and weathering on the development of steep mountain slopes. In: Abrahams, A.D. (Ed.), Hillslope Processes. Winchester, Allen and Unwin Inc., Sydney, NSW, Australia, pp. 245–267, 1986.

Stock G.M., Collins B.D., Santaniello D.J., Zimmer V.L., Wieczorek G.F., Snyder J.B. Historical Rock Falls in Yosemite National Park, California (1857–2011). U.S. Geological Survey Data Series 746. https://pubs.usgs.gov/ds/746/., 2013.

Stoffel M., Perret S.. Reconstructing past rockfall activity with tree rings: some methodological considerations. Dendrochronologia 24 (1), 1–15, 2006.

Tavukcuoglu A., Duzgunes A., Caner-Saltıkc E.N., Demirci S. Use of IR thermography for the assessment of surface-water drainage problems in a historical building, Agzıkarahan (Aksaray), Turkey. NDT & E International; 38: 402–410, 2005.

Teza G., Marcato G., Castelli E., Galgaro A. IRTROCK: A MATLAB toolbox for contactless recognition of surface and shallow weakness of a rock cliff by infrared thermography. Computers & Geosciences; 45: 109–118, 2012.

Titman D.J. Applications of thermography in non-destructive testing of structures. NDT & E Int.; 34(2):149–54, 2001.

Tortorici G., Bianca M., De Guidi G., Monaco C., Tortorici L. Fault activity and marine terracing in the Capo Vaticano area (southern Calabria) durino the Middle-Late Quaternary. Quatern. Int. 101- 102, 269–278, 2003.

Trombetta A., Cirrincione R., Corfu F., Mazzoleni P., Pezzino A. Mid-Ordovician U–Pb ages of Porphyroids in the Peloritan Mountains (NE Sicily): palaeogeographical implications for the evolution of the Alboran microplate. Journal of the Geological Society, 161: 165–276, 2004.

UNESCO, Risk Management Training Handbook, 2010.

UNESCO. Convention Concerning the Protection of the World Cultural and Natural Heritage. Paris, 1972.

USGS. Landslide Types and Processes. Fact Sheet 2004-3072, 2004.

Varnes D.J. Slope movement types and processes. In: Schuster RL, Krizek RJ (eds) Landslides, analysis and control, special report 176: Transportation research board, National Academy of Sciences, Washington, DC., 11–33, 1978.

Watanabe T., Sassa K. Seismic Attenuation Tomography and its Application to Rock Mass Evaluation. Int. J. Rock Mech. Min. Sci. & Geomech. Abstr., 33, 5, 467--477, 1996.

Wines D.R., Lilly P.A. Measurement and analysis of rock mass discontinuity spacing and frequency in part of the Fimiston Open Pit operation in Kalgoorlie, Western Australia: a case study. International Journal of Rock Mechanics & Mining Sciences 39, 589–602, 2002.

Wisniewski M., Lindow S., Ashworth E. Observations of ice nucleation and propagation in plants using infrared video thermography. Plant Physiology; 113: 327-34, 1997.

Wolfe W.L., Zissis G.J., Editors, The infrared handbook. Washington, DC: Office of Naval Research 1993.

WP/WLI — The International Geotechnical Societies' UNESCO Working Party on World Landslide Inventory, 1993. Multilingual Landslide Glossary. BiTech Publishers, Richmond B.C., Canada.

Wu J.H., Lin H.M., Lee D.H., Fang S.C. Integrity assessment of rock mass behind the shotcreted slope using thermography. Engineering Geology, 80: 164– 173, 2005.

Wyllie D.C., Mah C.W. Rock Slope Engineering civil and mining 4th edition. Spon Press Taylor & Francis Group, 431 pp, 2004.

Yin Y., Sun P., Zhang M., Li B. Mechanism on apparent dip sliding of oblique inclined bedding rockslide at Jiweishan, Chongqing, China. Landslides 8(1):49-65, 2011.